PHOTOCROSSLINKABLE POLY(PROPYLENE GLYCOL-CO-LACTIDE) DIMETHACRYLATE-BASED MICRONEEDLE PATCH FOR SCARLESS WOUND HEALING OF SOFT TISSUES

LYU SHANG

PhD

The Hong Kong Polytechnic University

This programme is jointly offered by The Hong Kong Polytechnic University and Zhejiang University

2024

The Hong Kong Polytechnic University
Department of Biomedical Engineering
Zhejiang University
School of Mechanical Engineering

Photocrosslinkable Poly(Propylene Glycol-Co-Lactide) Dimethacrylate-Based Microneedle Patch for Scarless Wound Healing of Soft Tissues

LYU Shang

A thesis submitted in partial fulfilment of the
requirements for the degree of Doctor of Philosophy

October 2023

Certificate of Originality

I hereby declare that this thesis is my own work and that, to the best of my knowledge and belief, it reproduces no material previously published or written, nor material that has been accepted for the award of any other degree or diploma, except where due acknowledgement has been made in the text.

_____(Signed)

_____LYU Shang_____(Name of student)

Abstract

Soft tissues, including skin, muscle, tendons, fat, cover almost all of the human body. Soft tissue injuries caused by trauma, disease, or overexertion are common in daily life but still lack targeted and effective repairing devices. This project aims to develop novel microneedle systems, involving special structure designs and multiple functions (e.g., programmable drug release, mechanical regulation, electrical stimulation) to better assist wound healing and tissue regeneration. Central to the systems was poly (lactide-co-propylene glycol-co-lactide) dimethacrylate (P_mL_nDMA; m and n represent the unit length of propylene glycol and lactide), a photocrosslinkable bioink developed by our group previously.

We first designed a bioinspired microneedle system loaded with exosomes and mangiferin for fast and scarless wound healing. The microneedle had a core-shell structure with a gelatin methacryloyl (GelMA) hydrogel shell and a P_7L_2DMA core. The swelling of GelMA tip provided a reliable contact between the wound tissue and the microneedle. At the early stage, the GelMA shell rapidly released small molecule mangiferin to suppress macrophage-initiated inflammation. Then, the P_7L_2DMA core sustainably released macromolecule exosomes for angiogenesis of human umbilical vein endothelial cells (HUVECs). *In vivo* results further confirmed the promising effects of combining mangiferin with exosomes on anti-inflammation, angiogenesis, and even scar reduction.

Secondly, we designed a contractile microneedle patch microneedle patch to regulate the stress environment in the wound and thereby reduce scar formation. Specifically, a skin wound bed has two kinds of forces: (1) the intrinsic tension force generated by the surrounding tissue and (2) the traction force generated during wound healing by fibroblasts and myofibroblasts. To counter those two forces, our microneedle system consisted of three parts: the backing layer, the middle part, and the tilted part. The backing layer was made of $P_{68}L_8$DMA, which was flexible and elastic enough to resist tension force of the surrounding tissue. The middle part was made of P_7L_2DMA, which was stiffer for relieving the local stress generated by myofibroblasts. The tilted part was also made of P_7L_2DMA and was inserted into the surrounding tissue for tissue adhesion and force transduction. The contractile microneedle patch showed better tissue adhesion than pure backing layer and common microneedle patches. Using a fibroblast-loaded collagen system as an *in vitro* scar model, the proposed microneedle system significantly reduced some scar-related protein (α-SMA, CXCL14) expressions. RNA sequencing revealed that our patch could decrease the scar formation by downregulating some mechanical signaling pathways, including ECM-receptor interaction, PI3K signaling pathway, and focal adhesion.

Finally, we designed a self-powered patch integrated with microneedle and aligned piezoelectric polyvinylidene fluoride (PVDF) microfibers for cardiac tissue regeneration. The microneedle tip was made of stiff P_7L_2DMA for tissue anchoring while the backing layer was made of elastic $P_{68}L_8$DMA which could withstand long-

term cyclic stretching (no breaking under 20% strain). The aligned PVDF fibers were fabricated by electrohydrodynamic (EHD) printing and attached on the $P_{68}L_8$DMA backing layer. Once the microneedle was inserted into the cardiac tissue and deformed with cyclic stretching by heartbeats, the aligned PVDF fibers could generate electrical stimulation to cells and provide topological induction for cell growth. Under dynamic cell culture, the electrical stimulation caused by the PVDF fiber significantly enhanced the cardiac functional protein (connexin 43) expression in H9c2 cardiomyocytes and induced oriented growth with elongated cell morphology.

In summary, based on different microneedle systems, we investigated the effects of different treatments, including drug therapy, mechanical regulation, and electrical stimulation, on wound healing and scar formation. We found that long-term drug treatment augmenting the wound healing process was important for healing acceleration and scar reduction. Mechanical regulation is also crucial to scar reduction as stress relaxation in wound area during wound healing could effectively reduce fibroblast proliferation and scar-related protein expressions. In addition, electrical stimulation could promote cardiomyocyte functions, slowing down or even reversing myocardial infarction.

List of Publications

Journal Papers

1. **Lyu S**, Dong Z, Xu X, Bei H-P, Yuen H-Y, James Cheung C-W, Wong M-S, He Y, Zhao X. Going below and beyond the surface: Microneedle structure, materials, drugs, fabrication, and applications for wound healing and tissue regeneration. *Bioactive Materials*, 2023, 27, 303-326.

2. **Lyu S,** Nie J, Gao Q, Xie C, Zhou L, Qiu J, Fu J, Zhao X, He Y. Micro/nanofabrication of brittle hydrogels using 3D printed soft ultrafine fiber molds for damage-free demolding. *Biofabrication*, 2020, 12(2), 025015.

3. Li Y, **Lyu S (co-first author)**, Yuan H, Ye G, Mu W, Fu Y, Zhang X, Feng Z, He Y, Chen W. Peripheral Nerve Regeneration with 3D Printed Bionic Scaffolds Loading Neural Crest Stem Cell Derived Schwann Cell Progenitors. *Advanced Functional Materials*, 2021, 31(16), 2010215.

4. Li Y, Xie M, **Lyu S**, Sun Y, Li Z, Gu Z, He Y. A Bionic Controllable Strain Membrane for Cell Stretching at Air-Liquid Interface Inspired by Papercutting. *International Journal of Extreme Manufacturing*, 2023.

5. Wu P, Zhou L, **Lyu S**, Fu J, He Y. Self-sintering liquid metal ink with LAPONITE® for flexible electronics. *Journal of Materials Chemistry C*, 2021, 9(9), 3070-3080.

6. Gu Z, Xie M, **Lyu S**, Liu N, He J, Li Y, Zhu Y, Fu J, Lin H, Xie C, He Y. Perfusable Vessel-on-a-Chip for Antiangiogenic Drug Screening with Coaxial Bioprinting.

International Journal of Bioprinting, 2023, 8(4).

7. Nie J, Gao Q, Xie C, **Lyu S**, Qiu J, Liu Y, Guo M, Guo R, Fu J, He Y. Construction of multi-scale vascular chips and modelling of the interaction between tumours and blood vessels. *Materials Horizons*, 2020, 7(1), 82-92.

8. Liu N, Zhu Y, Yu K, Gu Z, **Lyu S**, Chen Y, He C, Fu J, He Y. Functional Blood–Brain Barrier Model with Tight Connected Minitissue by Liquid Substrates Culture. *Advanced Healthcare Materials*, 2023, 12(4), 2201984.

9. Zhang Q, Luo Y, Liang B, Suo D, **Lyu S**, Wang Y, Zhao X. An anti-bacterial and anti-cancer fibrous membrane with multiple therapeutic effects for prevention of pancreatic cancer recurrence. *Biomaterials Advances*, 2022, 137, 212831.

10. Zhou L, Ramezani H, Sun M, Xie M, Nie J, **Lyu S**, Cai J, Fu J, He Y. 3D printing of high-strength chitosan hydrogel scaffolds without any organic solvents. Biomaterials Science, 2020, 8(18), 5020-5028.

11. **Lyu S**, Liu Q, Yuen H-Y, Xie H, Yang Y, Yeung W-K, Tang C-Y, Wang S, Liu Y, Li B, He Y, Zhao X. Differential-targeting core-shell microneedle patch with coordinated and prolonged releases of mangiferin and MSC-derived exosomes for scarless skin regeneration. Materials Horizons. Submitted.

Patents

1. He Y, **Lyu S**, Chen W, Fu J, a multiscale biological scaffold and its fabrication and application, China. (Granted, CN112915255B)

2. He Y, **Lyu S**, Nie J, Fu J, a method for sample production based on microfiber

template and its application, China. (Filed, CN110479390A)

3. Zhao X, **Lyu S**, Yang YH, a core-shell microneedle patch and its preparation method, China. (Applied, 202410104261.1)

4. Zhao X, **Lyu S**, Yang YH, a piezoelectric cardiac patch and its preparation method and application, China. (Applied, 202410104077.7)

Acknowledgements

First of all, I would like to express my heartfelt gratitude to my supervisor, Dr. Zhao Xin, for her guidance, support, and invaluable knowledge throughout the journey of completing this doctoral thesis and my PhD study. I would also like to thank her for providing me with the opportunity to study at PolyU. With her guidance, I have been able to expand my knowledge beyond my original mechanical engineering background and gain a deeper understanding of biological concepts. This has allowed me to broaden my future research path.

I would like to thank my co-supervisor, Prof. He Yong in Zhejiang University for his great support, encouragement during my research life, and the opportunity to further my studies at PolyU. His imagination and inspiration in scientific research have constantly motivated me to undertake bold and exploratory work.

Then, I would like to thank all my colleagues and friends in PolyU: Dr. Yang Yuhe, Dr. Zhang Qiang, Miss. Mei Quanjing, Miss. Rao Jingdong, Miss. Xie Huizhi, Mr. Bei Ho Pan, Mr. Yuen Andy, Mr. Xu Tianpeng, Miss. Suo Di, Mr. Liu Huaqian, Mr. Liu Qi, Mr. Chun Hei Lam, Mr. Zhao Shuai, Miss. Zhou Xintong, Miss. Mo Yongyi, Miss. Zhang Shanshan, Mr. Chen Zhenhua, Miss. Chen Tianyu, Miss. Wong Ching Yui Ryta, and Mr. Gordon Hung, in Dr. Zhao’s group. In particular, I would give my thanks to Miss Xie Huizhi for helping with exosome extraction and TEM characterization, to Mr. Liu Qi for helping with material purification and material degradation test, to Mr.

Yuen Andy and Mr. Bei Ho Pan for helping with paper writing, to Mr. Zhao Shuai and Mr. Chen Zhenhua for helping with cell culture, to Mr. Gordon Hung for helping with sample preparation. In addition, many thanks to Prof. Zheng Zijian and his student Miss. Zhuang Qiuna for helping with the piezoelectric test of the PVDF fibers, Mr. He Yi for helping with some preliminary test of the piezoelectric experiment. I also want to thank all my colleagues and friends in Zhejiang University: Dr. Gao Qing, Dr. Shao Huifeng, Dr. Nie Jing, Dr. Xie Chaoqi, Dr. Shao Lei, Dr. Xie Mingjun, Mr. Sun Yuan, Dr. Hamed Ramezani, Dr. Yu Kang, Mr. Liu Yu, Mr. Wang Peng, Mr. Zhou Ruijian, Mr. Zeng Jiahui, Mr. Niu Xuefeng, Mr. Fu Zhenliang, Mr. Chen Lulu, Mr. Tian Jialong, Mr. Gu Zeming, Miss. Zhang Yani, Mr. Zhou Luyu, Mr. Lu Chunfei, Mr. Li Xiang, Mr. Li Yuanrong, Mr. Wu Pengcheng, Mr. Jingzhong Boyu, Mr. Zhu Yuanbo, Mr. Zhang Jingbo, Miss. He Jing, Mr. Chen Yuewei, Mr. He Chaofan, Mr. Li Yangning, Mr. Li Zhuang, Mr. Ji Haina, Mr. Qi Xianyang, Mr. Liu Nian, Mr. Liu Guofeng, Mr. Muhammad Hassan Sarfraz, Mr. Yao Ke, Mr. He Honghui, Mr. Gao Yan, Miss. Zhu Meng, Mr. Zhang Zhaojie, Mr. Liu Kai, Mr. Qiao Tianhong, and Mr. Weng Jiahao. Thank you for your companionship and encouragement throughout my research journey.

Lastly, I would like to acknowledge the unwavering support of my parents and friends. Their constant belief in my abilities and encouragement have been a source of motivation during the challenging times of this research endeavor. Their

understanding and patience have been invaluable, and I am forever grateful for their presence in my life.

Table of content

Chapter 1 Introduction

1.1 Wound healing of soft tissues

Soft tissues cover almost all of the human body, including skin, muscle, tendons, fat, and so on. Soft tissue injuries caused by trauma, disease, aging, or overexertion are common in daily life but still difficult to repair due to the lack of targeted and effective repairing devices.[1] This situation is anticipated to deteriorate in the future due to a growing elderly demographic and a rising global prevalence of individuals suffering from chronic wounds, placing significant financial burdens on society. To meet the growing demand for soft tissue regeneration, wound dressings incorporating state-of-the-art drug delivery systems have been innovated in recent decades, including tissue engineering scaffolds, micro/nano particles, and hydrogels.[2] Each of these methods has its own benefits and has improved drug delivery efficiency by controlling release kinetics and enhancing drug retention rate. But they may face challenges in permeating scar tissues and wound clots to deliver cargos due to the barrier effect. Therefore, there is a need for more effective delivery systems to enhance soft tissue regeneration.

1.1.1 Pathological process of wound healing

Normal wound healing process has 4 major phases: homeostasis, inflammation, proliferation, and remodeling.[3] During homeostasis and inflammation, immune cells such as platelets are recruited to eliminate pathogens and to control bleeding. Chemokines and growth factors secreted by these immune cells attract other cells and lead to the proliferation phase. The proliferation phase involves several important events, including formation of new blood vessels (i.e., angiogenesis), reformation of

the epidermal skin layer (i.e., re-epithelialization), and granulation tissue development (which requires a temporary extracellular matrix). After proliferation, the wound tissue contracts and undergoes remodeling, where the previously generated matrix gradually transforms into either functional skin or scar tissue.

1.1.2 Scar formation

As a natural part of the healing process in many tissues, scar formation happens when a fibrous tissue replaces the original tissue in an area of injury or damage. After the inflammation phase, fibroblasts migrate to the injury site, proliferate, and secrete collagen, a key protein that forms the structural framework of the scar tissue. Over time, the collagen fibers become organized and cross-linked, leading to a dense scar. Although scar formation is important for wound healing and tissue repair, excessive or abnormal scarring can lead to functional impairments and aesthetic concerns, like hypertrophic scar and keloid scar. Understanding the mechanisms underlying scar formation is crucial for developing strategies to modulate or minimize scar formation and promote optimal tissue regeneration.

Unlike adult wounds, wounds in the fetal body can heal without any scars.[4] Such difference can be attributed to a variety of cell types. Fetal fibroblasts exhibit faster proliferation than adult fibroblasts, and primarily generate collagen III during wound healing.[5] Furthermore, fetal wound healing does not involve myofibroblast differentiation, which is characterized by the expression of α-smooth muscle actin and

contributes to scar formation in adults. In addition, fetal wound healing has reduced inflammation due to a lower number of recruited neutrophils, which are the primary inflammation cells in wound area.[6] Macrophages, which influence the growth and differentiation of cells, formation of ECM, and remodeling, are recruited during wound healing, but in diminished numbers during early-stage fetal development. In particular, fetal skin has a higher ratio of M2 (anti-inflammatory) to M1 (pro-inflammatory) macrophages than adult skin, despite fewer macrophages in fetal skin.[7] Finally, tissues and fluids surrounding the fetus contain more mesenchymal stem cells (MSCs) than adult wounds, which lead to immunoregulatory effects on wound repair.[8] Co-culturing MSCs and macrophages could induce an M2 transition in macrophages, leading to the upregulation of IL-10 and the downregulation of IL-12.[9] Mimicking the above-mentioned cellular phenomena associated with fetal wound healing can help with scarless healing in adults.

Besides these biological cues, physical factors, like stress environment, can also be crucial to scar formation. For example, excessive stress can activate the integrin-FAK mechanical pathway and promote fibroblast differentiation into the scar-promoting EN-1 phenotypes, leading to excessive matrix deposition and scar formation.[10] There are many clinical treatments based on stress regulation, like W-plasty, wound tension reduction patches, silicone gel patches, to reduce scar formation.

1.2 Current therapies for wound healing

Traditional wound healing methods in clinics include wound cleansing, debridement, and dressings. However, these methods focus on preventing infection and providing initial protection, which cannot address the complex biological processes necessary for optimal and fast wound healing. Current therapies for wound healing, like tissue engineering scaffolds and microneedles, aim at promoting tissue repair with the support of biomaterials, scaffolds, cells, growth factors, and efficient drug delivery. In this section, several tissue engineering scaffolds, like injectable scaffolds, electrospun scaffolds, and 3D printing scaffolds, and microneedle patch are discussed with regards to their pros and cons.

1.2.1 Injectable scaffolds

Injectable scaffolds, especially injectable hydrogels, have largely been explored in regenerative medicine recently. They can be injected as a liquid and subsequently form a gel-like structure *in situ* in different ways, such as photocrosslinking, thermosensitivity, and pH responsiveness. The advantage of injectable hydrogels is the ease of application as the hydrogel conforms precisely to the shape of the wound, eliminating the need for additional adhesives or sutures. In addition, injectable hydrogels can be delivered through minimally invasive methods, such as syringe injection, reducing patient discomfort. As a result, they are ideal carriers for cell delivery and bioactive molecules.

However, these injectable hydrogels usually have poor mechanical properties and may

not provide sufficient structural support for tissue regeneration. It is also difficult to precisely control their degradation rates, release profiles, and shape formation. As a result, considerations should be given to their mechanical properties, stability, and precise control during formulation and application.

1.2.2 Electrospun scaffolds

Electrospun scaffolds have gained considerable interest for wound dressings due to their distinctive micro- and nano-scale fibrous structure that closely resembles the native ECM. Their highly porous structure also enhances fluid absorption and facilitates the exchange of oxygen, water, and nutrients. In addition, the high surface area not only enhances cell behaviors, but also offers large payload of therapeutic agents. Bioactive molecules like growth factors or antimicrobial agents have been loaded in for a controlled release to enhance wound healing. However, if the pores within the fibrous network are nanosized, cell infiltration into the scaffold is often restricted. Furthermore, electrospinning some high-molecular-weight polymers would sometimes require toxic solvents, which may compromise the biocompatibility of the final products and affect the bioactivity of the loaded proteins.

1.2.3 3D-printed scaffolds

3D printing is widely applied for fabricating tissue engineering scaffolds in recent decades, as it allows for tailored geometries, sizes, and internal structures, enabling personalized treatment. Unlike injectable and electrospun scaffolds, 3D-printed

scaffolds can provide many more physical cues, such as topological morphology, porosity, and gradient mechanical properties, for stimulating cell functions and tissue regeneration. In addition, most biological tissues (e.g., the skin) are heterogeneously layered structures, and 3D printing can achieve such spatial heterogeneity by loading different printing materials.

However, current 3D printing scaffolds still have some limitations. For example, 3D printing requires bio-inks with a certain strength and viscosity, which can compromise cell compatibility. Some 3D printing processes often introduce factors that damage cell viability, such as shear forces during extrusion-based printing and blue light exposure during photopolymerization. Additionally, current 3D printing cannot achieve full-scale mimicry of biological tissues and their functionalities due to a limited precision of tens of micrometers.

1.2.4 Microneedle patch

Microneedle, a novel system comprising an array of microscale needle tips, has garnered significant interests because of its non-invasive nature, ease of use, and ability to deliver various drugs topically in a controlled manner.[11] While originally designed for transdermal drug delivery by penetrating the stratum corneum, microneedle has expanded its applications in recent years[12] to the repair of tissues like skin, heart, and bone.[13-22]

Microneedles offer distinct advantages with regard to tissue regeneration. Firstly,

these micro-sized needle tips can traverse physical barriers at wound area, such as exudates, clots, and scars, facilitating sustained drug release. Secondly, the administration process is non-invasive and painless, resulting in better patient compliance compared with conventional hypodermic injections. Thirdly, the needle array structure exerts mechanical influence on wounds in two distinct ways: (1) tissue penetration induces collagen production and reorganization [23, 24] and (2) the microneedle patches could support the wound area and alter the local tissue stress, further contributing to scar reduction.[25] Fourthly, microneedles offer potential advantages in overcoming drug resistance associated with biofilms in the wound site, by physically breaking down the biofilm into planktonic bacteria.[26] Furthermore, microneedles can load and deliver diverse drugs including small molecules, macromolecules, extracellular vesicles (EVs), nanoparticles, nucleic acids, and cells. [20, 27-32] Last microneedles can contain stimulus-responsive materials, like poly(N-isopropylacrylamide), to monitor wound conditions through various physical and chemical signals, including temperature, reactive oxygen species, pH, and proteins.[28, 33-36] Such responsiveness empowers microneedles to deliver drugs in a targeted manner based on the specific phase of wound healing.

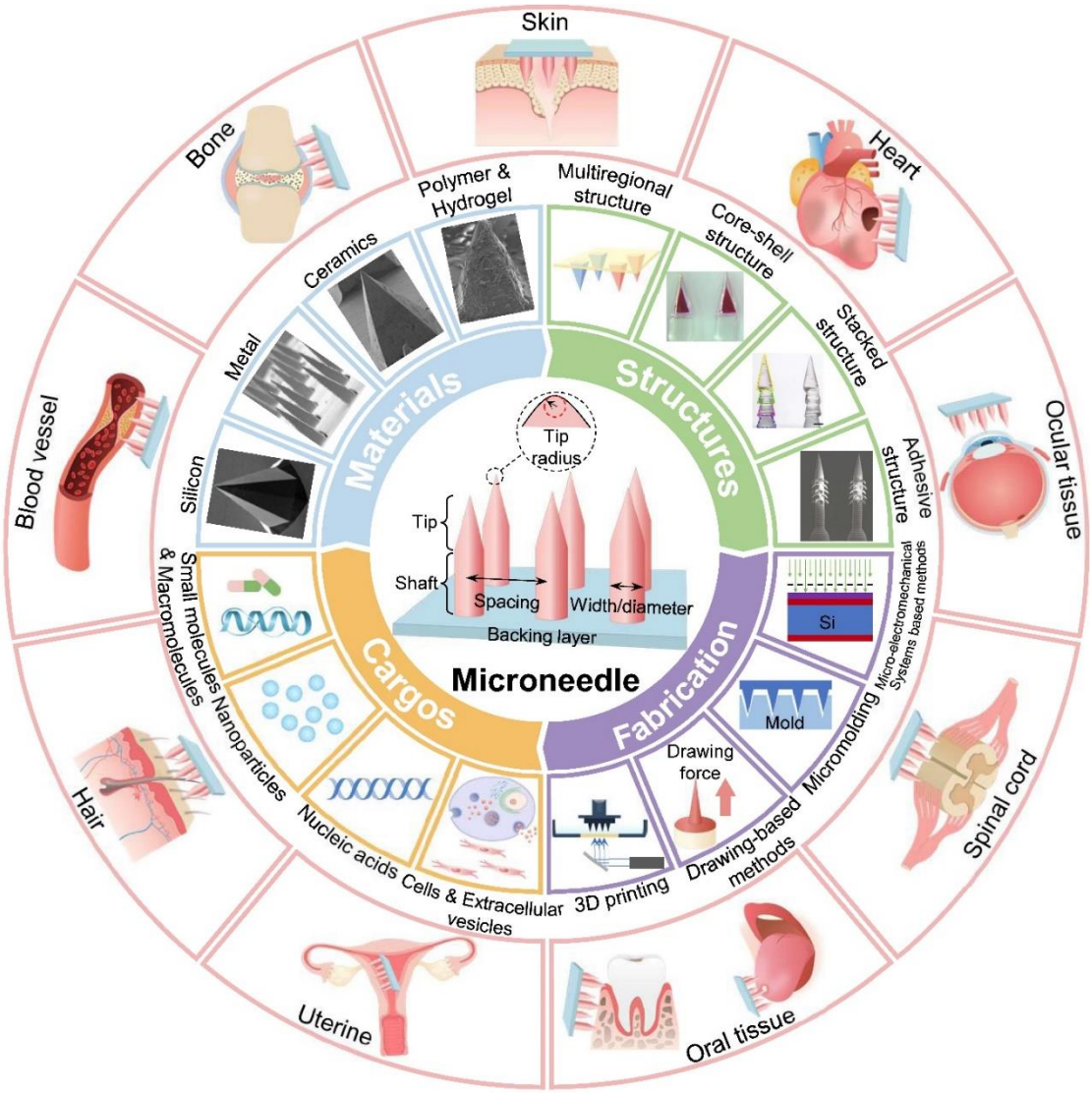

Figure 1-1. Illustration showing the utilization of microneedle in wound healing and tissue regeneration. Reproduced with permission from [37]. Copyright 2023, Elsevier.

1.3 Current microneedles for wound healing

Figure 1-1 illustrates the classical structure of microneedle patch. Microneedle length varies from 25 μm to 2,000 μm. This corresponds to a depth of around 2,000 μm, which is the combined thickness of the epidermal layer and stratum corneum (10-15 μm),[38] as the function of microneedles is to pass through the corneum, reach the epidermis, and avoid insertion into the dermis and the blood vessels and nerves within

the dermis. To ensure effective penetration, the tip radius is typically varied between 1 μm and 25 μm. To achieve successful insertion, the needles must possess sufficient strength and stiffness to avoid buckling and breakage during penetration. Microneedle properties are based on the shape, material properties, and particularly the shaft diameter, typically ranging from 10 μm to 300 μm.[39] In this section, we will discuss structural designs, material selection, and drug loadings in microneedles.

1.3.1 Materials to fabricate microneedles

Currently, depending on the specific applications and requirements (e.g., degradation, stiffness), materials used for microneedle manufacturing include metals (e.g., stainless steel, titanium), silicon, ceramics, and polymers (e.g., hydrogel, carbohydrate). [40-46]

Metals, ceramics, and silicon exhibit high stiffness (over 10 GPa) and are non-degradable. Therefore, they are commonly used for creating pores in the skin to enhance drug permeation. They can be manufactured as either hollow microneedles, enabling direct administration of drug solutions, or solid microneedles having drugs dipped on their surfaces.

In contrast, polymers offer the advantage of adjustable drug release kinetics by tuning molecular weight, charge properties, concentration, and crosslinking density. Polymers such as poly (lactic-co-glycolic acid) (PLGA) and polycaprolactone (PCL) have intermediate mechanical properties (10 MPa to 10 GPa) and can persist *in vivo* for weeks to years for drug release, making them well-suited for the regeneration of bone-related tissues (e.g., tendons, cartilages), which require long-term recovery and

adequate mechanical support. On the other hand, hydrogels, such as gelatin methacryloyl (GelMA), polyethylene (glycol) diacrylate (PEGDA), and hyaluronic acid (HA), exhibit lower mechanical properties (< 1 MPa) and faster degradation (a few hours to a few weeks). This makes them suitable for applications that require quick drug release (e.g., anti-infection purposes during early-stage wound healing) and organs composed of soft ECM (e.g., skin, liver, kidney).[47, 48] Furthermore, hydrogels, being ECM-like materials containing large amount of water, are appropriate for transporting drugs that are soluble in water, nanoparticles, proteins, EVs, nucleic acids, and cells. By varying crosslinking and chemical modification methods, one can adjust the polymer network density, thereby tuning the controlled drug release based on the size of the drug.[49]

Besides the basic materials mentioned above, conductive materials, such as carbon nanotube,[50] MXene,[51] have also been integrated into microneedles recently for electrical stimulation. Such new feature results in improved cell functions for cells sensitive to electrical signals, such as cardiac and neural cells. Additionally, after conductive modification, microneedles can serve as patch electrodes for monitoring physiological signals. Compared to traditional patch electrodes, microneedle electrodes allow for more extensive contact with deep tissues.

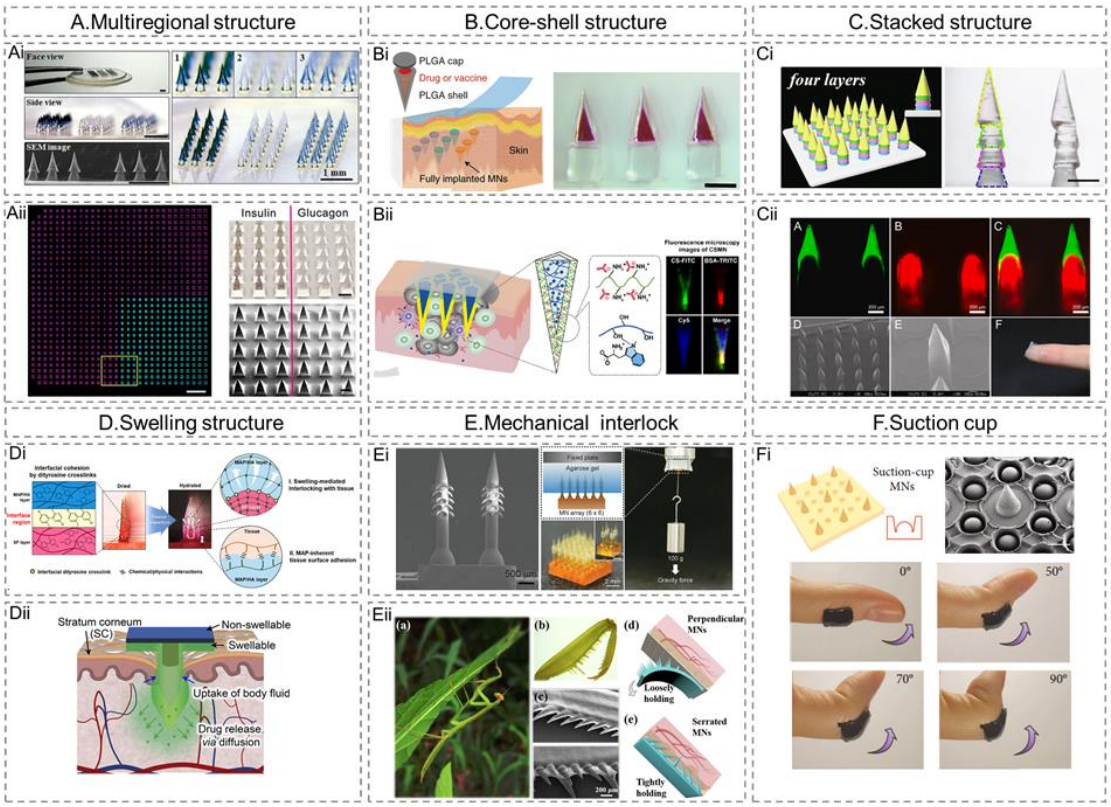

Figure 1-2. Structural designs of microneedles applied in wound healing. (A) Multiregional microneedles. (B) Core-shell microneedles. (C) Stacked microneedles. (D) Typical swelling microneedles. (E) Biomimetic structures for tissue interlocking. (F) Microneedles with suction cup structure. Scale bar, 300μm. Reproduced with permission from [37]. Copyright 2023, Elsevier.

1.3.2 Microneedle structure

Although microneedle has predominantly served as a drug delivery carrier, the common microneedle structure has been proven effective in modulating the local stress of biological tissues.[25] This characteristic gives microneedles a natural advantage in regulating scar formation.

Thanks to the advancements in fabrication techniques, particularly micromolding, more sophisticated microneedle structures can be achieved, and various loadings can

be incorporated to a single patch and released in a regulated manner over time and space. [11, 52] Various microneedle structures and fabrication methods have been proposed to achieve precise control over the distribution of multiple drugs in patches, containing multiregional structures (**Figure 1-2**A),[53-55] core-shell structures (**Figure 1-2**B), and stacked structures (**Figure 1-2**C).[56-58] To achieve programmable release of specific drugs, researchers often make use of the release properties of materials or incorporate unique structures.

In **Figure 1-2**A, different drugs were loaded into distinct underlying materials and integrated into different areas of the patch. Due to the varying degradation characteristics of these materials, the cargos were released asynchronously within one patch. The programmable drug release method is good for combined therapies involving diverse drugs or for treatments which need patients to take medicine multiple times a day (e.g., diabetes). However, in certain topical wound treatments, where coordinated drug release is more effective, this kind of design may not be suitable.

In **Figure 1-2**B, the core and shell portions can be incorporated with various drugs, leading to a sequential drug release (first from the shell then from the core). Increasing the layer number of the shell can load more drug types but leads to larger needle size, potentially compromising the non-invasiveness of the microneedles. As a result, the common practice is to have fewer than three layers.

In **Figure 1-2**C, multiple layers of matrices were stacked onto a single needle tip. Different from core-shell structures that release drug in a sequential manner, layers in

stacked structures degrade simultaneously, leading to a coordinated release of several cargos. Stacked structure in **Figure 1-2**Ci can enhance the adhesive property of microneedle patches, which could be categorized into two types: swelling and biomimicking structure.

Swelling microneedles (**Figure 1-2**D) exploits the water up taking capability of needle tips, often made from materials like GelMA, polystyrene-block-poly(acrylic acid), and hyaluronic acid.[59-61] Once inserted, the tips absorb water and rapidly expand, mechanically interlocking with the biological tissues.

Figure 1-2E shows the microneedles with biomimicking structures, such as backward barbs, and pagoda-like structures, which are more effective for tissue interlock.[57, 62-64] These structures do not impede microneedle insertion but generate certain withdrawal force upon removal due to their mechanical interlock with targeted tissues. Additionally, they are able to attach to tissues in both wet and dry conditions, irrespective of the surface smoothness of the tissue.

Microneedles with octopus-sucker-mimicking structures have also been developed (**Figure 1-2**F).[65] These structures create a partial vacuum between the tissue surface and the suction cups to generate negative pressure for tissue adhesion, which is particularly suitable for adhesion in wet environments.

1.3.3 Drugs loaded in microneedles

Drug-loaded microneedles utilized in wound management are usually applied for anti-bacterial, anti-inflammatory, angiogenic, or anti-scarring purpose. Small-molecule

drugs represent the first category and include antibiotics and antifungal medications, such as doxycycline, tetracyline, amphotericin B, and clindamycin.[35, 66-68] Nonsteroidal anti-inflammatory drugs (NSAIDs) like salicylic acid,[69, 70] corticosteroids like triamcinolone acetonide,[71] and antimetabolites like methotrexate are used as anti-inflammatory and anti-scarring drugs.[72]

The second category of drugs used in wound treatment is macromolecular drugs, like growth factors (e.g., PDGF, VEGF), cytokines (e.g., tumor necrosis factor-α, interleukin-6), and antibodies (e.g., tumor necrosis factor inhibitor).[73] Cytokines and growth factors are crucial natural signaling molecules that facilitate communication among cells to stimulate cell behaviors, including migration, angiogenesis, and immunoregulation. Tumor necrosis factor inhibitors are antibodies used to treat skin disorders and arthritis by acting on the immune system for anti-inflammatory effects.[74, 75]

Nucleic acids, including DNA, siRNAs, and miRNAs, have demonstrated effectiveness in wound healing due to their relationships with various signaling pathways in different stages (e.g., inflammation suppression, angiogenesis, migration).[3, 29, 76, 77] DNA-based strategy involves transporting exogenous DNA to cells to express specific proteins. On the other hand, siRNA- and miRNA-based therapies concentrate on impeding the specific messenger RNA (mRNA) translation associated with the target gene. Currently, limitations of nucleic acids are short-term effects and low delivery efficiency, as cells hardly take up exogenous nucleic acids and the unfavorable cellular environment usually degrades nucleic acids. To overcome these challenges, carriers such as nanoparticles, cationic polymers, and viral vectors

have been incorporated into microneedles.[29, 77, 78] Microneedles enable direct delivery of cargos to the wound area while the carriers can efficiently deliver the nucleic acids into the cell nuclei.

Nanoparticles can be mixed into microneedles to serve as antibacterial agents or drug carriers. Anti-bacterial nanoparticles commonly use metallic materials (e.g., Ag, Au, CuO, and ZnO [79]), carbon-based materials (e.g., carbon nanotube and graphene), polymers (e.g., chitosan, quaternary ammonium, and certain synthetic polymers involving hydrophobic or cationic moieties).[80, 81] Meanwhile, drug carriers include polylactic-co-glycolic acid nanoparticles, poly-D,L-lactide-co-glycolide nanoparticles, gelatin nanoparticles, and calcium phosphate particles.[82-86] The nanoparticles are typically incorporated into dissolvable microneedles through methods like solvent evaporation, co-polymerization, and coating.

EVs, containing exosomes (diameter ranging from 30 to 100 nm) and microvesicles (diameter ranging from 50 to 1,000 nm), are another emerging therapeutic approach in wound healing. These vesicles are secreted by various stem/progenitor cells like BMSCs, iPSC-derived MSCs, myocardial progenitor cells, and endothelial progenitor cells.[87] The vesicles' content of nucleic acids, enzymes, and ECM proteins collectively contribute to different phases of healing.[88] Additionally, EVs have the advantage of easily passing through cell membranes, as they are regulators of intercellular communication, making them more effective as therapeutic agents than pure nucleic acids.

Cell therapy uses various cell types such as mesenchymal stem cells (MSCs), induced

pluripotent stem cell (iPSC)-derived MSCs, and endothelial progenitor cells to promote the healing process.[89] These cells could be integrated into microneedles in three different ways: 1) directly delivered through hollow microneedles, 2) cultured on the microneedles, or 3) embedded in microneedles. However, encapsulating cells in microneedles can be challenging due to the harsh fabrication conditions involving chemical solvent, high temperature, vacuum, and ultraviolet light. Long-term storage, contamination, and cell viability also hinder the development of cell-loaded microneedles.

Chapter 2 Core-shell microneedle patch with coordinated and prolonged releases of mangiferin and MSC-derived exosomes for scarless skin regeneration

2.1 Introduction

In the past decades, the advancement of biomaterials fabrication techniques has enabled various skin wound dressings, including electrospun mats,[90-94] 3D-printed scaffolds, and *in situ* crosslinkable hydrogels[95, 96]. While their biocompatibility is good, their functionalization for controllable drug delivery remains a weakness. Microneedle is a promising functionalization strategy for topical drug delivery due to its ability to penetrate and anchor into the wound site.[37, 97] This offers possibility to load and release bioactive macromolecules (e.g., growth factors,[98, 99] exosomes,[100-103] and cells[104, 105]) beyond the epidermis and to augment the functionalities of its base biomaterials (e.g., GelMA,[101, 106, 107] hyaluronic acid methacrylate (HAMA),[99, 105, 108, 109] and chitosan[98, 110]). Indeed, hydrogel swelling can enhance the anchoring of the microneedles, and hydrogel degradation can facilitate drug release at the microneedle tips. However, these functionalization strategies are often insufficient to address a major issue in skin wound care: the multi-step remodeling of wound healing. More specifically, skin wound healing can be broken down into different phases with various needs, which necessitates a multi-scale microneedle design to release corresponding drugs while keeping them viable during storage.

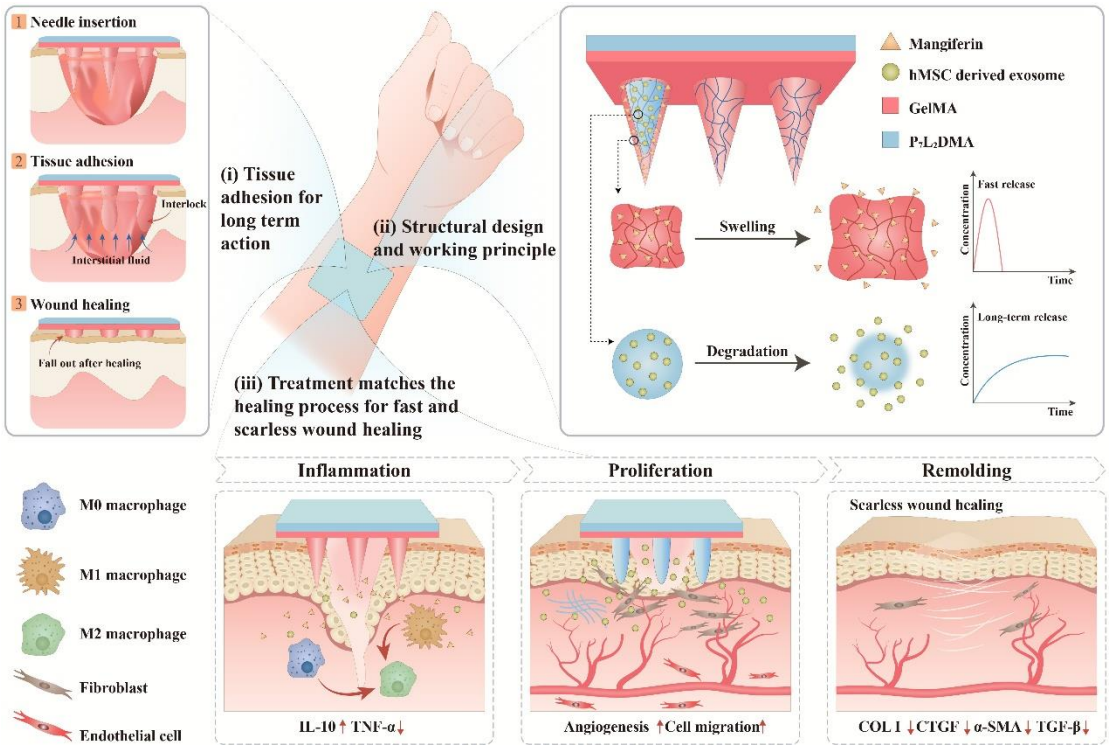

Figure 2-1. Schematic diagram showing the (i) tissue adhesion for long-term action. After microneedle insertion into the wound bed, GelMA in needle tips absorb the interstitial fluid, swell, and interlock with the wound tissue. Finally, the needle tips degrade, and the remaining backing layer falls out after wound healing. (ii) Structure design and working principle. The microneedle system consists of mangiferin-loaded GelMA shell and hMSC-derived exosome-loaded P_7L_2DMA core. Mangiferin is released quickly by diffusion during GelMA swelling, while exosome is released sustainably by the degradation of P_7L_2DMA. (iii) Treatment matches the healing process for fast and scarless wound healing. After insertion, the core-shell microneedle firstly releases mangiferin and bits of exosomes for anti-inflammation, downregulating the tumor necrosis factor-α (TNF-α) level and upregulating the interleukin-10 (IL-10) level. Then, during the proliferation phase, exosomes are sustainably released, promoting angiogenesis and cell migration. Finally, the wound is

remodeled with less scar-related markers, like collagen I (COL I), connective tissue growth factor (CTGF), α-smooth muscle actin (α-SMA) and transforming growth factor-β (TGF-β).

In this chapter, we developed a wet-adhesive, core-shell microneedle patch with a dual drug release profile (**Figure 2-1**). The shell portion is made of GelMA, due to its excellent biocompatibility, high swelling ratio, and fast drug release capability. The core portion is made of P_7L_2DMA, chosen for its dense crosslinked network that enables slow protein release and excellent biocompatibility.[111] The gelatin methacryloyl (GelMA) shell achieved tissue-interlocking adhesion via *in situ* swelling and burst release of mangiferin to suppress early-stage inflammation. On the other hand, the poly (lactide-co-propylene glycol-co-lactide) dimethacrylate (P_7L_2DMA) core slowly degraded over time to sustainably release human mesenchymal stromal cell (hMSC)-derived exosomes for immunoregulation and angiogenesis. Although hMSC-derived exosomes possess multiple beneficial properties for wound healing (e.g., anti-inflammatory effect via M2 polarization[112], improved tissue regeneration[113], enhanced angiogenesis and tube formation[114-116]), its efficacy is impeded by rapid drug release, weak mechanical strength, and fast hydrogel degradation.[100-102, 117, 118] Thanks to the denser polymer network of P_7L_2DMA, it can effectively block the rapid diffusion-driven release of biomacromolecules such as exosomes. Instead, the exosomes are slowly released along with the degradation of P_7L_2DMA.

To the best of our knowledge, such differential strategy of anti-inflammation and long-term exosome release for scarless skin wound healing has not been demonstrated in the literature previously. In addition, we believe our core-shell microneedle system not only offers a promising skin wound dressing for clinical treatment, but also provides a universal strategy for diverse tissue regeneration.

2.2 Methodology

2.2.1 Materials

GelMA (EFL-GM-60) was bought from EFL (Suzhou, China). Mangiferin (M3547), lithium phenyl-2,4,6-trimethylbenzoylphosphinate (LAP), and propylene glycol (PPG) were bought from Sigma-Aldrich (Hong Kong). Lactide (LA), methacryloyl chloride (MAC), trimethylamine (TEA), stannous octoate, trimethylamine (TEA), Irgacure 819, and 2-hydroxyethyl methacrylate (HEMA) were purchased from Macklin reagent (Shanghai, China). Dichloromethane (DCM) and diethyl ether were purchased from Duksan (Hong Kong). Phosphatic buffer solution (PBS), Dulbecco's modified eagle medium (DMEM), minimum essential medium α (MEM α), fetal bovine serum (FBS), and penicillin/streptomycin (PS) were bought from Gibco (Hong Kong). Exosome-depleted fetal bovine serum (FBS) was purchased from Vivacell (Shanghai, China). Lipopolysaccharide (LPS), 4′,6-diamidino-2-phenylindole (DAPI), and Nile red dye were purchased from Thermo Fisher (Hong Kong).

2.2.2 Synthesis of P_7L_2DMA

The synthetic process has been presented in our previous work.[111] In brief, under nitrogen protection, the ring-opening polymerization of 34.4 g of PPG and 23 g of LA was carried out at 150℃ for 6 hours using stannous octoate as a catalyst. Then 4.22 g MAC and 4.05 g TEA (both were diluted in DCM) were added in drops at 0℃ to conjugate methacrylate groups to the polymer chain end. To remove TEA·HCL generated during this process, the product (mixture of P_7L_2DMA and TEA·HCL) was dissolved in diethyl ether, followed by filtration. Finally, to eliminate the residual solvent in the oil solvent phase, 2 h of rotary evaporation was used, and pure P_7L_2DMA was obtained. To form a photocrosslinkable P_7L_2DMA precursor, P_7L_2DMA was mixed with a HEMA solution containing Irgacure 819 (10 wt% of Irgacure 819 mixed in HEMA) at a ratio of 9:1 (w/w).

2.2.3 Isolation of exosomes

Human mesenchymal stem cells (hMSCs) were chosen as the cell source of exosome extraction. hMSCs were incubated in MEM α with 10% (v/v) FBS and 1% PS. All cells were cultured under humidified conditions at a temperature of 37°C and 5% concentration of CO_2, and the medium was refreshed every 48 h. After the cells got to 80% confluence in the culture flask, the medium was altered to a conditioned medium consisting of MEM α, 10% (v/v) exosome-depleted FBS, and 1% (v/v) PS. The cells were incubated in the conditioned medium for another 48 h. The conditioned medium was then collected and subjected to centrifugation at a temperature of 4°C and a speed

of 800 g for 5 min, followed by a speed of 2,000 g for 20 min. The resulting supernatant was purified using a 0.22-μm filter to obtain the clarified conditioned medium. Finally, the clarified conditioned medium underwent two rounds of centrifugation at 4°C and 100,000 g for 70 minutes each to obtain the pure exosomes.

2.2.4 Nanoparticle tracking analyzer (NTA)

Size profile of exosome and its concentration were assessed using a NanoSight NS300HSBF (Malvern Panalytical GmbH, Germany) instrument featuring a CMOS camera and a 405-nm laser source. Samples were diluted using PBS to 10^7-10^8 vesicles mL^{-1}, with 50–200 vesicles observed per frame. A 60-second video was recorded using the NanoSight device. Data were analyzed using the NanoSight NTA 3.1 software with a detection threshold of 5.

2.2.5 Transmission electron microscope (TEM)

TEM was employed to examine the morphology of exosomes. A 2-μL exosome solution was placed on carbon-coated grids. Subsequently, a 1% (v/v) glutaraldehyde solution was used to fix the exosomes on the grid for 5 min. Double-distilled water was then used to wash the fixed exosomes several times. Excess water was dried under ambient conditions. To stain the samples, uranyl oxalate at pH 7 was applied for 5 min, followed by incubation in a mixture of 4% v/v uranyl acetate (UA) and 2% v/v methylcellulose on ice for 10 min. Excess liquid was air-dried. The fixed samples were observed using TEM (JEOL, JEM-2010).

2.2.6 Fabrication process of microneedles

The whole microneedle system was fabricated by a multistep micro-molding technique. Firstly, to prepare mangiferin-loaded GelMA solution for shell construction, a 10% (w/v) GelMA solution was prepared by dissolving GelMA in PBS containing 0.5% (w/v) LAP. Then mangiferin was added into the 10% (w/v) GelMA solution to achieve a final concentration of 2 mg/mL. Secondly, to prepare exosome-loaded P_7L_2DMA solution for core construction, P_7L_2DMA precursor and 10% (w/v) Irgacure 819 in hydroxyethyl methacrylate (HEMA, Sigma Aldrich, Hong Kong) solution were mixed at a ratio of 9:1 (w/w), forming the photocrosslinkable P_7L_2DMA solution. Then, the exosome solution was poured into the photocrosslinkable P_7L_2DMA solution (500 μg exosome in 1 mL P_7L_2DMA solution) and put into a freeze dryer to remove the water overnight. Thirdly, 200 μL mangiferin-loaded GelMA solution was added into a PDMS mold (Y61, Weixinyiyao technology, China) and vacuumed to get rid of the bubbles between the mold and the solution for 3 min. Then, a 405-nm blue light was used to crosslink the mangiferin-loaded GelMA solution. The crosslinked GelMA solution and the mold were put into thermostat to dehydrate the GelMA at 40℃ for about 1 h, forming a layer of drug-loaded GelMA shell on the bottom of the mold. Fourthly, 200 μL exosome-loaded P_7L_2DMA solution was poured into the mold and vacuumed to get rid of the bubbles for over 30 min. A 405-nm blue light was also used to crosslink P_7L_2DMA. Finally, the core-shell microneedle patch was gently removed from the mold.

2.2.7 Microneedle morphology characterization

The general morphology of the microneedles was detected utilizing an optical microscope (Nikon, Japan) and scanning electron microscope (SEM, Tescan VEGA3, Czech Republic) after gold sputtering using a sputter coater. A fluorescence microscope (Nikon, Japan) and a confocal microscope (TCS SPE, Leica) were used to observe the microneedle's core-shell structure. For shell staining, DAPI was added to the GelMA solution during the fabrication process. For core staining, a Nile red dye was mixed in the P_7L_2DMA solution during fabrication.

2.2.8 *In vitro* drug release test

For testing the mangiferin release from GelMA, a standard curve that determined the concentration of mangiferin in PBS was obtained at first. A series of mangiferin solutions (500, 250, 125, 62.5, 31.25, 15.625, 7.8, 3.9, 1.95, and 0.976 μg/mL) were prepared by serial dilution in a 96-well plate. The optical density value of these solutions was detected using a microplate reader (Thermo Fisher, Hong Kong). The standard curve was drawn by Origin software, reflecting the relationship between the concentrations and optical density values. Subsequently, a 2 mg/mL mangiferin/GelMA solution was prepared as mentioned above. Each sample was prepared by dehydrating 200 μL crosslinked mangiferin/GelMA solution. Finally, samples were immersed in 5 mL PBS for a drug release test. The PBS was fully refreshed at each time point (30 min, 1 h, 2 h, 4 h, 6 h, 8 h, 10 h, 12 h, 24 h, 48 h, 72 h,

96 h). The extracted solution was used for optical density value measurement at 370 nm and for calculating the quantity of the released mangiferin. The cumulative release rate at each time point = cumulative release quantity / total quantity (0.4 mg). For testing the exosome release from P_7L_2DMA, a 500 μg/mL exosome/ P_7L_2DMA mixture was prepared. Each sample was prepared by crosslinking 200 μL exosome/P_7L_2DMA mixture and subsequent immersion in 5 mL PBS. PBS was fully refreshed at each time point (from day 1 to day 21), and the extracted solution was used for concentration measurement using an exosome ELISA kit (mlbio, China) according to the user manual. The cumulative release rate at each time point = cumulative release quantity / total quantity (100 μg).

2.2.9 *In vitro* degradation test

For the P_7L_2DMA degradation test, each sample was made into a disc shape (8 mm in radius and 5 mm in thickness) using a mold. The samples were firstly weighed using an analytical balance for initial weight and then immersed in a 50-mL centrifuge tube containing 10 mL of PBS. After incubation for different periods (7, 14, 21, 28, 35, 42, and 56 days) at 37℃, the samples were taken from the solution, dried in a vacuum at room temperature, and weighed by a balance. The mass loss (M_L) at different time points was calculated following the equation: M_L (%) = $(M_0-M_t)/M_0 \times 100$, where M_0 was the initial weight of the samples, and M_t was the dry weight of samples at different time points. As low-polymerized lactic acid is the primary degradable chain segment in P_7L_2DMA, samples of the degradation solution were collected at various

time points over 56 days for lactate detection using the lactate Assay Kit (ab65330, Abcam). The cumulative concentration of lactate at each time point was determined following the instructions provided in the user manual.

2.2.10 Mechanical test

A mechanical testing system (ElectroForce 3200, Bose, America) was used for the compression test and tissue adhesion test of the microneedles. For the compression test, a piece of microneedle sample was attached to the stainless-steel platform (needles facing up) using glue, and the sensor probe approached the microneedle at a velocity of 5 mm/min. The initial distance between the probe and the needle tips was 1 cm. All data were treated and analyzed by Origin software. For the tissue adhesion test, a piece of microneedle sample was attached to the sensor probe (needles facing down), and a piece of pig skin was attached to the stainless-steel platform using glue. The sensor probe was programmed to move down for 1 cm initially at a velocity of 5 mm/min. Then, the sensor probe was set to hold the position for 2 min for stabilization and finally pulled up at a 5 mm/min velocity. The initial separation between the needle tips and the pork skin was 0.4 centimeters. All data were analyzed by Origin software. An insertion test was conducted using pork skin tissue. The needle tip was stained with red dyes and then inserted directly into the pork skin.

2.2.11 *In vitro* anti-inflammatory assay

RAW 264.7 macrophages were incubated using a complete DMEM medium. The

cells were incubated in a humidified environment at a temperature of 37°C and a CO_2 concentration of 5%. The medium was refreshed every two days. Seven groups, including control (PBS), LPS, LPS + GelMA, LPS + P_7L_2DMA, LPS + MN/MF, LPS + MN/EXO, and LPS + MN/MF/EXO, were involved in the test. The concentrations of loaded mangiferin and exosomes were determined according to the release kinetics of P_7L_2DMA and GelMA. Except for the control and LPS groups, all groups used extraction solutions by immersing the samples in full DMEM for two weeks for investigation. Then, except for the control group, LPS was supplemented to all groups at 100 ng/mL as a working medium. Finally, RAW 264.7 macrophages were pre-cultured for 24 h in full DMEM, followed by the medium changing to the working medium of the seven groups. The cells were incubated for another 48 h and prepared for immunostaining. 4% paraformaldehyde was used to fix cells for 30 min, then permeabilized with 0.5% Triton X-100 for 10 min and blocked for 1 h under room temperature. Subsequently, samples were incubated with primary antibodies, including CD86 (1:500, ab239075, Abcam), CD206 (1:900, ab64693, Abcam), TNF-α (1:500, ab183218, Abcam) and IL-10 (1:500, ab189392, Abcam), at a temperature of 4℃ for the whole night. Then the samples were incubated with secondary antibodies, Alexa Fluor® 488 (1:500, ab150157, Abcam), for 1 h at room temperature. The samples were washed three times by PBS and then examined by a fluorescence microscope (Nikon, Japan).

2.2.12 Tube formation assay

Human umbilical vein endothelial cells (HUVECs) were cultured in full DMEM containing 10% (v/v) FBS and 1% PS. The cells were incubated under humidified conditions at 37°C and 5% CO_2, and the culture medium was refreshed every 48 h. Six groups, including control (PBS), P_7L_2DMA, GelMA, MN/MF, MN/EXO, and MN/MF/EXO, were involved in the test. Except for the control group, all groups used extraction solutions by immersing the samples in full DMEM for two weeks. HUVECs were plated at 50,000 cells per cm^2 on a 24-well plate precoated with 250 μL Matrigel and grown to confluence. Then, the culture medium in each group was replaced by the solution prepared as mentioned above. The tube formation was imaged by an inverted microscope (Nikon, Japan) at three time points (4, 6, and 18 h) and analyzed with ImageJ software applying the angiogenesis analyzer plugin.

2.2.13 Scratch wound healing assay

L929 fibroblasts and HUVECs were both cultured as in full DMEM containing 10% (v/v) FBS and 1% PS. The cells were incubated under humidified conditions at 37°C and 5% CO_2, and culture medium were replaced every two days. Six groups, including control (PBS), P_7L_2DMA, GelMA, MN/MF, MN/EXO, and MN/MF/EXO, were involved in the test. Except the control group, all groups used extraction solutions which was made by immersing the samples in full DMEM for two weeks for investigation. L929 fibroblasts were grown at a density of 1×10^5 cells per cm^2 in a 24-well plate and grown to confluency. Then wounds were scraped in each well using a 200 μL pipette tip. The wound area was imaged by a microscope (Nikon, Japan) at

five time points (0, 4, 12, 24, and 48 h) and analyzed with ImageJ software. HUVECs were grown at a density of 1×10^5 cells per cm^2 in a 6-well plate and grown to confluency. Then wounds were scraped in each well using a 200 μL pipette tip. The wound area was imaged by a microscope (Nikon, Japan) at four different time points (0, 4, 12, and 24 h) and analyzed with ImageJ software.

2.2.14 *In vivo* therapeutic test

The Animal Subjects Ethics Sub-committee of the Hong Kong Polytechnic University (Approval No. 21-22/83-BME-R-STUDENT) granted ethical approval for all animal experiments conducted in this study. The animal experiment was finished with the help of Wuhan Servicebio Technology Co., Ltd. Male C57BL/6J mice weighing around 20 g and aged 7 weeks were employed to establish the excisional full-thickness wound model. Before the procedure, the mice were anesthetized using 1.5% isoflurane in 100% O_2 gas anesthesia. A circular incision was then made along the midline of the mouse dorsal skin, encompassing the epidermis, dermis, subcutis, and muscularis layers. A total of 80 mice were used and allocated into five groups. In the blank group, the wound bed was treated with 100 μL PBS. Microneedles with GelMA shell and P7L2DMA core were applied for the pure MN group. For the MN/MF group, microneedles with mangiferin (100 μg/mL)-loaded GelMA shell and P_7L_2DMA core were applied. For the MN/EXO group, microneedles with GelMA shell and exosome (1 mg/mL)-loaded P_7L_2DMA core were applied. For the MN/MF/EXO group, microneedles with mangiferin-loaded GelMA shell and exosome-loaded P_7L_2DMA

core were applied. Mice were sacrificed for histology on days 7 and 14 post-operation.

2.2.15 Histology and wound healing evaluation

Wound images were taken on days 0, 7, and 14. The wound area was measured by ImageJ software by recognizing the border of the wound. Diagrams of wound areas at different time points were also generated using ImageJ software by setting the wound border as the region of interest (ROI). The tissue samples were subjected to hematoxylin-eosin (H&E) staining to visualize the newly generated skin tissue. Quantitative data, including the migrating epidermal tongue (MET) length, granulation tissue length, re-epithelialization ratio, and somatic cell quantity, were measured or counted using ImageJ. MET is the newly formed epithelium. Re-epithelialization ratio (%) = distance covered newly formed epithelium / wound width × 100%. TNF-α, IL-10, CD31, TGF-β, CTGF, Col I, and Col III immunostaining (Servicebio, China) was conducted to evaluate the angiogenesis, inflammation, and scar formation.

2.2.16 Western blot analysis

Isolated exosomes, mouse skin homogenates, and cell lysates were quantitated by bicinchoninic acid protein (BCA) assay. Subsequently, the specimens were subjected to electrophoresis on an 8-12% sodium dodecyl sulfate (SDS) polyacrylamide gel and subsequently moved to a PVDF membrane (Millipore). The protein-loaded PVDF membranes were blocked for 30 min at room temperature using 5% skim milk.

Following blocking, the membranes were incubated with primary antibodies, including CD9 (1:1000, ab223052, Abcam), ALIX (1:1000, ab275377, Abcam), GM130 (1:500, PA5-95727, Invitrogen), ACTIN (1:2000, GB15001, Servicebio), VEGFR1 (1:1000, GB114200, Servicebio), PDGF B (1:1000, GB11261, Servicebio), FGF2 (1:1000, GB113969, Servicebio), P65 (1:1000, GB11997, Servicebio), IL-10 (1:1000, GB11108, Servicebio), and TNF-α (1:1000, GB11188, Servicebio), overnight at 4°C. The PVDF membranes were washed three times for 5 min each with TBST and then incubated with the horseradish peroxidase-conjugated secondary antibodies at room temperature for 1 h. The labeled proteins were observed by a luminescent image analyzer.

2.2.17 RT-qPCR

RNA extraction and reverse transcription process were performed referring to the kit instructions. mRNA expression levels of angiogenesis- and inflammation-related proteins were calculated relative to GAPDH (internal control gene) using primers specific for VEGF, PDGF, NF-κB, IL-10, TNF-α, and FGF-2. (**Table 1**)

Table 1. Primers for RT-qPCR

Gene	Forward	Reverse
GAPDH	CCTCGTCCCGTAGACAAAATG	TGAGGTCAATGAAGGGGTCGT
FGF	CCAGGACCAGCTATCACCTACAGA	GCCATTCTCCAGCGTCCACT
IL-10	AATAAGCTCCAAGACCAAGGTGT	CATCATGTATGCTTCTATGCAGTTG
TNF-α	CCCTCACACTCACAAACCACC	CTTTGAGATCCATGCCGTTG
VEGF	GTAACGATGAAGCCCTGGAGTG	TCACAGTGAACGCTCCAGGAT
PDGF	GGCTTATCCGATGCCTTCTGT	TGACTCTCACTCAGCTCCAGCA
NF-κB	CCTGCTTCTGGAGGGTGATG	GGCTCATACGGTTTCCCATTTA

2.2.18 Statistical analysis

GraphPad software was used for statistical analysis. Unless otherwise stated, all tests were repeated at least three times. Results are shown in mean ± standard deviation (SD). A normality test was conducted for each set of data. One-way ANOVA was used in comparing two different groups. P-value ≤ 0.05 was considered statistically significant (*p ≤ 0.05, **p ≤ 0.01, ***p ≤ 0.001).

2.3 Results and Discussions

2.3.1 Synthesis of PGLADMA

We synthesized the PGLADMA as P_7L_2DMA where P_7 denotes seven repeating units of propylene glycol (PPG) and L_2 denotes two repeating units of lactide (LA) attached to either end of PPG. We previously demonstrated that this configuration possesses excellent *in vitro* and *in vivo* biocompatibility, capability to encapsulate and release bioactive macromolecules long-term, and appropriate mechanical properties (with compressive modulus of 50 MPa) [111, 119-122]. The synthesized P_7L_2DMA was characterized by ^{1}H NMR as $P_{7.19}L_{1.97}$DMA (data not shown).

2.3.2 Fabrication and characterization of the core-shell microneedle patch

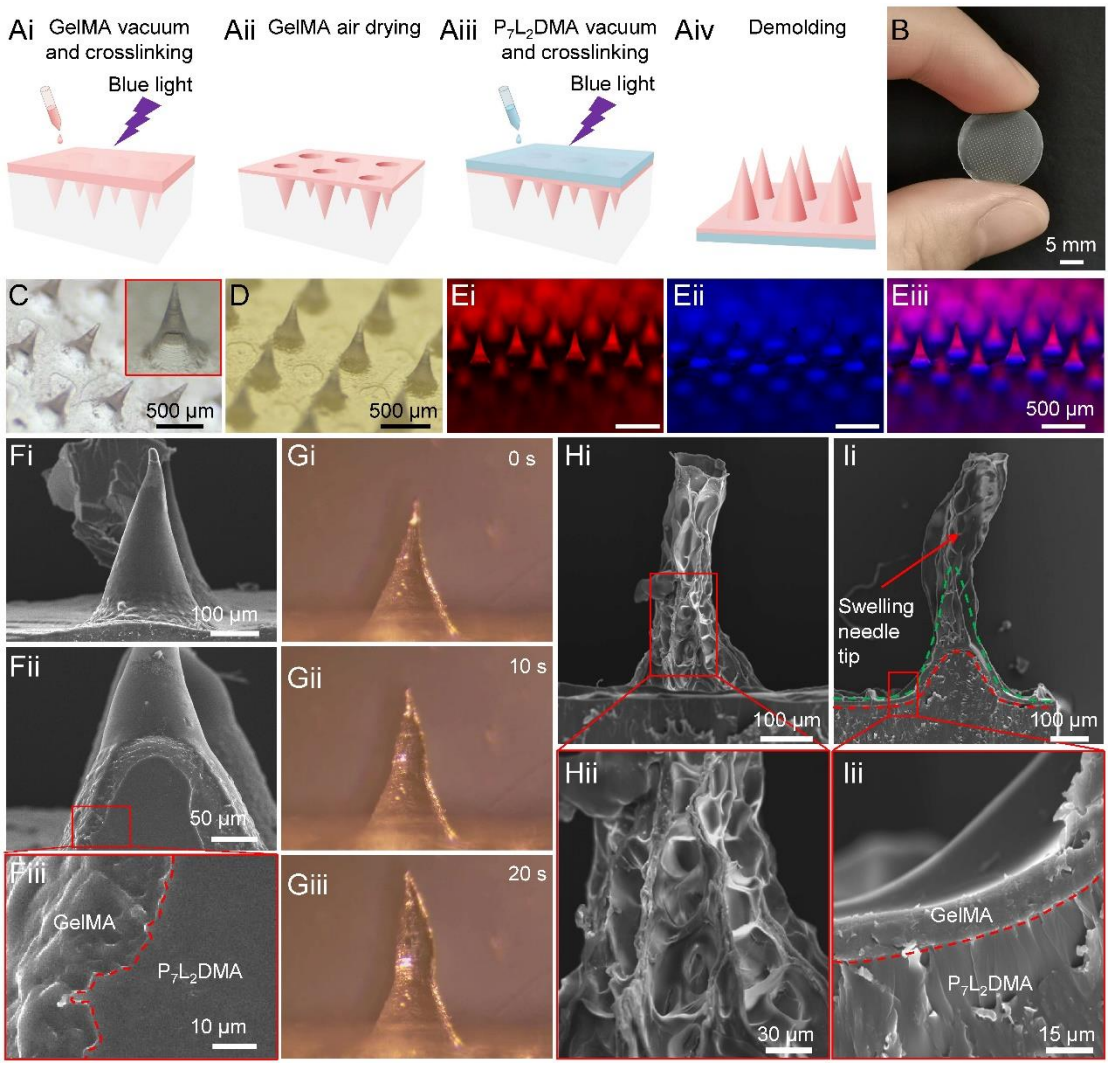

Figure 2-2. Fabrication, morphology, structure, and swelling of the core-shell microneedle patch. (A) Illustration of microneedle fabrication process. (i) GelMA vacuum and photo-crosslinking. (ii) GelMA air drying. (iii) P_7L_2DMA vacuum and photo-crosslinking. (iv) Demolding. (B) General appearance of the microneedle patch. Microscope images of (C) GelMA shell, and (D) the complete microneedles. (E) Fluorescence images showing the GelMA shell (red) and P_7L_2DMA core (blue) structure of the microneedle patch. (i) GelMA shell stained with red dye. (ii) P_7L_2DMA core stained with blue dye. (iii) Merged view. (F) Representative SEM images showing (i) the general structure of the microneedle, (ii) the core-shell structure of the microneedle, and (iii) the interface between the GelMA shell and the

P_7L_2DMA core showing the good combination of these two materials. Red dash line indicates the interface. (G) Representative microscope images of the microneedle after absorbing water for (i) 0 s, (ii) 10 s, and (iii) 20 s. The needle tip shows an obvious swelling. (H) Representative SEM images showing (i) the general structure of the microneedle after swelling, and (ii) the enlarged view of porous structure on the needle tip. (I) Representative SEM images showing (i) the core-shell structure of the microneedle after swelling. Red dash line indicates the GelMA-P_7L_2DMA interface. Green dash line indicates the original microneedle shape before swelling, and (ii) the enlarged view of the GelMA-P_7L_2DMA interface, presenting a good combination of these two materials even after swelling. Red dash line indicates the interface.

Our proposed core-shell microneedle system (**Figure 2-2A**) contained PGLADMA as the core (inner-layer) material of the microneedle, and GelMA as the shell (outer-layer) material. The core could slowly release exosome long-term while the shell could adhere onto the wound with burst release of mangiferin. [123-126] The fabrication involved four steps: solidifying the GelMA in the mold by vacuum and photocrosslinking (**Figure 2-2A**i), air-drying the GelMA to form the outer-layer structure (**Figure 2-2A**ii), solidifying the PGLADMA-in-GelMA by vacuuming and photocrosslinking (**Figure 2-2A**iii), and finally demolding the microneedle product (**Figure 2-2A**iv).

Figures 2-2B, 2-2C, and **2-2D** show the macroscopic image of the complete microneedle, the GelMA part of the microneedle under a microscope, and the full microneedle (with P_7L_2DMA) under the microscope, respectively. The microneedles had an average height of 403 ± 12 μm and a base diameter of 270 ± 0.40 μm. To

visualize the internal structure of the microneedle, we stained the GelMA and P_7L_2DMA layers in red and blue, respectively (**Figure 2-2E**i-iii). The GelMA and P_7L_2DMA layers were clearly distinguished with a core-shell structure.

Then, we examined the transitory interface between GelMA and P_7L_2DMA with scanning electron microscope (SEM). As shown in **Figure 2-2F**, the outer (GelMA) and inner (P_7L_2DMA) layers demonstrated a distinctive morphology, with the GelMA layer being rougher and more porous, and the P_7L_2DMA layer being more homogenous. We believed that the irregularity of the GelMA layer facilitated its integration and binding with P_7L_2DMA in two aspects. Firstly, the P_7L_2DMA precursor could infiltrate the GelMA shell during the vacuuming step **(Figure 2-2A),** so that the two layers were interlocked during the crosslinking step. Secondly, after the demolding, the GelMA shell would continue to shrink due to evaporation of residual water, which tightly wrapped the P_7L_2DMA material.

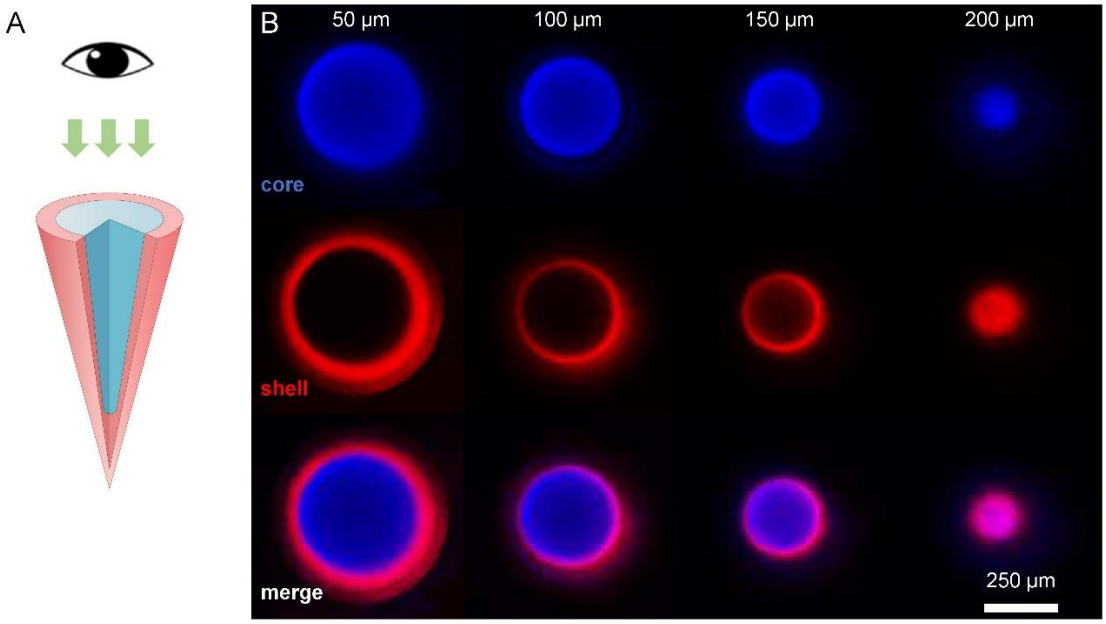

Figure 2-3. Confocal images of microneedle structure. (A) Illustration of microneedle observation using confocal microscopy. (B) Confocal images of microneedle cross sections at different height (i.e., 50, 100, 150, 200 μm).

We also characterized the material distribution at z-level by capturing a stained single needle tip at different height (from 50 to 200 μm, **Figure 2-3**) using a confocal microscope. The GelMA shell (red) showed a perfect circular distribution around the P_7L_2DMA core (blue). As the section height increased and approached the needle point, the diameters of core and shell decreased.

Since morphological changes of the GelMA (shell) layer during swelling is important for both tissue interlocking and core-shell layer interlocking, we dipped the microneedle into water and examined the structural and morphological changes of a single needle tip under a microscope. **Figures 2-2G**i-iii show the changes of the general appearance of a single needle after absorbing water for different periods (i.e., 0, 10, 20 s). The tip of the needle was greatly swollen within 20 s, while the base of the needle, which was mainly composed of P_7L_2DMA with a thin GelMA outer layer, was less swollen. Using SEM, we examined the swollen needle tip (**Figure 2-2H**) and further noted an emerging porous structure and volume expansion of the GelMA shell as opposed to the smooth structure in **Figure 2-2F**. The dissected needle tip in **Figure 2-2I** illustrates more details on the swelling behavior of the GelMA layer. Using the GelMA-P_7L_2DMA interface (red dashed line) and the extent of the original GelMA layer (green dashed line) as references, we observed significant swelling in the tip while the base showed no obvious deformation, with the inner surface of the GelMA shell still adhered to the P_7L_2DMA firmly. **Figure 2-2I**ii also illustrates the intact and

tight bonding between the GelMA shell and the P_7L_2DMA core. These results altogether indicated the microneedle could swell at the tip for tissue interlocking and keep a tight bonding between the GelMA shell and the P_7L_2DMA core at the base, demonstrating successful fabrication of a functional core-shell structure for the goal of an adhesive and multi-step drug-releasing patch.

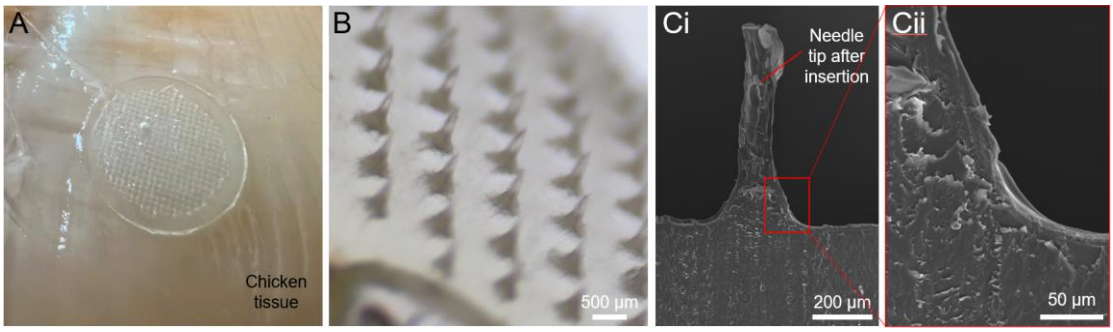

Figure 2-4. Core-shell integrity after tissue insertion. (A) Photo of the experimental setup for the tissue insertion test. Chicken tissue was selected as a model to simulate the wound tissue. (B) Microscope image showing the swelling of needle tip after tissue insertion. (Ci) SEM image showing the cross section of the needle tips after tissue insertion. (Cii) Enlarged view showing the interface of P_7L_2DMA-GelMA after tissue insertion.

To assess the core-shell integrity of the microneedle after wound insertion, we conducted tissue insertion tests using chicken tissue as a soft and moist mimic of wound tissue (**Figure 2-4**). In **Figure 2-4A**, the core-shell microneedle was inserted into the chicken tissue and left in place for 1 min before removal. **Figure 2-4B** shows slight swelling of the needle tips, with the water-absorbing component primarily concentrated at the tips that directly contact the tissue. **Figure 2-4C**ii demonstrates no delamination at the interface between P_7L_2DMA and GelMA. Given that the water-

absorbing segment is predominantly situated at the upper part of the needle tip, it does not impact the adhesion between the P_7L_2DMA core and the GelMA shell.

2.3.3 Mechanical and tissue adhesion property of the core-shell microneedle patch

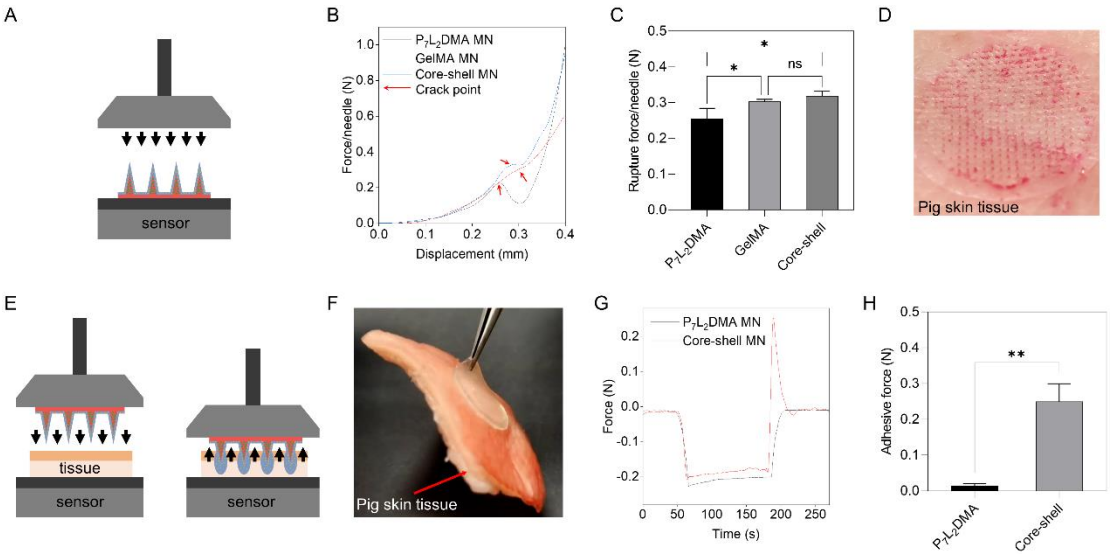

Figure 2-5. Mechanical property of the core-shell microneedle patch. (A) Illustration of the compression test. (B) Force-displacement curve of compression test. Red arrows indicate the microneedle crack point during the test. (C) Rupture force comparison between the P_7L_2DMA microneedle, GelMA microneedle, and core-shell microneedles. (D) Microneedle insertion test in pig skin tissue. Needle tips were coated with red dye. Red dots on the tissue indicate the insertion site. (E) Illustration of the tissue adhesion test. (F) Image of pig skin adhesion of the core-shell microneedle. (G) Force-time curve of the tissue adhesion test. (H) Adhesive force comparison between the P_7L_2DMA microneedle and the core-shell microneedle. The differences are statistically significant when p values are below 0.05 (*), and 0.01 (**).

MN = microneedle.

As skin wounds are softer and less elastic than the stratum corneum, a needle tip that is too stiff can easily cause secondary trauma.[105] GelMA in its swollen state is sufficiently soft for tissue penetration, and its dehydration can enforce a packing effect of its polymer network to increase its stiffness. After insertion, GelMA would first absorb the interstitial fluid, swell, and become softer when interlocking with the wound tissues, providing suitable tissue adhesive force and biocompatibility of the microneedles for the surrounding tissues. Therefore, we chose dehydrated GelMA shell to facilitate wound insertion[127, 128]. **Figure 2-5A** illustrates our microneedle compression setup of the above properties.

As shown in **Figure 2-5B**, microneedles in all groups cracked at a similar displacement (~280 μm), where the average rupture forces of P_7L_2DMA, GelMA, and core-shell microneedle were 0.26 N/needle, 0.30 N/needle and 0.32 N/needle, respectively (**Figure 2-5C**). In addition, the rupture forces of the GelMA and core-shell microneedles had no significant difference, indicating that GelMA was the primary component that provided the insertion force and thus tissue interlocking. The rupture force above was actually far beyond the required force to penetrate porcine skin (around 0.05 N/needle [129]), confirmed by **Figure 2-5D** with an array of red dots.

To further verify the dynamic tissue-interlocking mechanism of GelMA, we used a setup involving three steps: insertion, stabilization, and pulling of the microneedle against a pork skin (**Figure 2-5E**). The microneedle was first inserted into the pork skin for 2 min (**Figure 2-5F**). As shown in **Figure 2-5G**, before pulling the microneedle from the pork skin (0 – 180 s), the curves of the P_7L_2DMA and core-shell groups matched, hovering at around 0.20 N during insertion (0 – 60 s) and achieving a steady value during stabilization (60 – 180 s). However, during the pulling process (180 – 200 s), the core-shell microneedle showed a drastic rise of adhesive force while the pure P_7L_2DMA microneedle showed no significant adhesion. **Figure 2-5H** also shows that the average adhesive force of the core-shell microneedle was 0.25 N, which was ten times higher than that of the pure P_7L_2DMA microneedle (0.02 N). This strong interlocking force is attributed to the swelling GelMA shell that, without the P_7L_2DMA core, would simply be too soft and fell apart during the pulling process (data not shown). In summary, our core-shell microneedle patch had sufficient tissue adhesive force for long-term drug delivery.

2.3.4 *In vitro* drug release from the core-shell microneedle patch

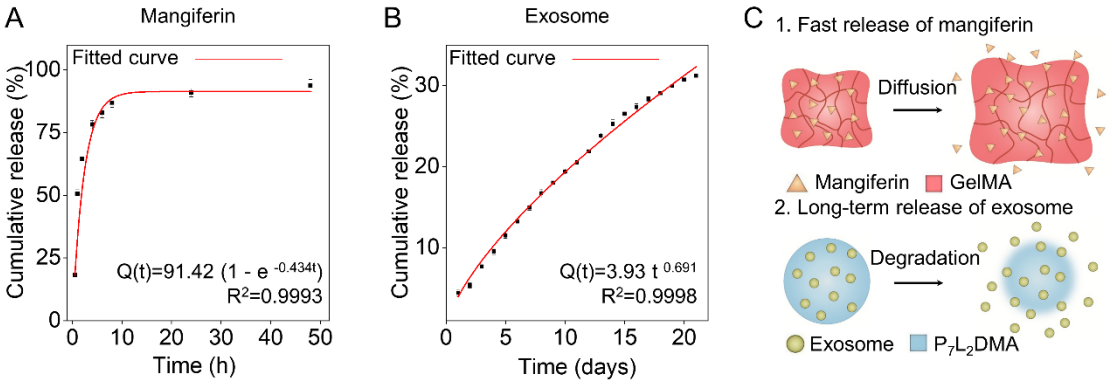

Figure 2-6. Drug release from the core-shell microneedle patch. (A) Cumulative release of mangiferin from GelMA in PBS within 48 h. (B) Cumulative release of exosome from P_7L_2DMA in PBS within 21 days. (C) Schematics showing the release mechanisms of mangiferin and exosome.

To fabricate the drug-loaded microneedles, we loaded exosome into P_7L_2DMA solution and mangiferin into GelMA solution before repeating the same process **Figure 2-2A**i-iv. The drug encapsulation did not significantly influence the mechanical and tissue adhesion property of the microneedle patch (data not shown). We found that 86.94 ± 2.25% of total mangiferin was released from GelMA rapidly within the first 8 h and the cumulative percentage reached 93.84 ± 2.94% within 48 h (**Figure 2-6A**). We chose Weibull function to fit the release data: $Q(t) = Q_\infty (1 – \exp(-at^b))$, where Q(t) is the percentage of drug released at time t, Q_∞ is the percentage of drug released at infinite time, a is the scale factor, and b is the shape factor. After curve fitting, the release profile could be described by the equation: $Q(t) = 91.42 (1 – \exp(-0.434t))$, where b equals to 1, suggesting the mangiferin release from GelMA obeys Fick's first law of diffusion.[130-133] This rapid mangiferin release is expected to counter early-stage inflammation, which usually lasts for 2-3 days.[134]

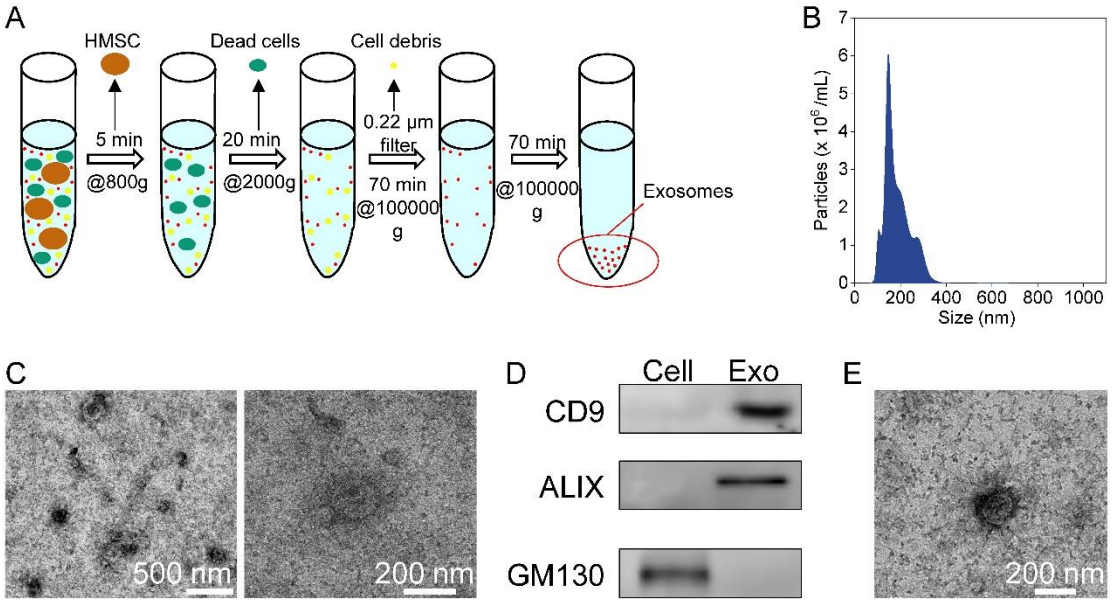

Figure 2-7. Extraction and identification of hMSC-derived exosomes. (A) Illustration showing the extraction of hMSC-derived exosomes using differential centrifugation. (B) Nanoparticle tracing analysis of hMSC-derived exosomes. (C) Transmission electron microscope (TEM) images of extracted exosomes prior to loading into P_7L_2DMA. (D) Western blot of representative exosome-related protein markers. Typical exosome markers CD9 and ALIX were expressed while GM130 (Golgi marker) was absent in the extracted exosome, indicating high purity of the exosomes. (E) TEM image of exosomes after 21 days of release from P_7L_2DMA. Similar morphology of exosomes before encapsulation and after release indicated that P_7L_2DMA preserved the structure of exosomes.

For exosome release, we started with characterizing our yield and used differential centrifugation to extract the hMSC-derived exosomes (**Figure 2-7A**). After isolation, nanoparticle tracking analyzer (NTA) was used to confirm the particle size distribution (**Figure 2-7B**). The exosomes had a modal diameter of 146.6 nm

with a normal size distribution. They presented a distorted cup-shaped morphology (**Figure 2-7C**). The exosome samples were also positive for exosome marker proteins CD9 and ALIX while negative for GM130 (a Golgi marker only in cells but not in exosome) (**Figure 2-7D**), indicating high purity of the exosomes. These results showed successful preparation of exosomes with exosomal molecular features and morphology.

Then, we loaded the exosomes into P_7L_2DMA in the core-shell microneedle patch to characterize the release profile. **Figure 2-6B** shows that the release rate of exosomes was slower than that of mangiferin, where the cumulative release of exosome from P_7L_2DMA was 25.24 ± 0.66% in 14 days and 31.19 ± 0.27% in 21 days. Such slower exosome release is advantageous as the proliferation phase of wound healing usually lasts for 4-21 days.[135] After curve fitting, the release profile could be described by the equation: $Q(t) = 3.93\ t^{0.691}$, where Q(t) is the amount of cumulative drug released at time t, following the Ritger–Peppas model with the release exponent n being equal to 0.691. This implied the exosomes were released from P_7L_2DMA by anomalous transport, based on a combination of diffusion and erosion.[136, 137] In addition, the exosomes appeared intact after 21-day release from the microneedle patch, indicating that the P_7L_2DMA preserved the structure of exosomes for long-term delivery (**Figure 2-7E**). In summary, the mangiferin in the shell was rapidly released from the GelMA hydrogel through diffusion, while the exosomes in the core was slowly released along with the P_7L_2DMA degradation (**Figure 2-6C**). To confirm the relationship between exosome release kinetics with P_7L_2DMA degradation, mass loss of P_7L_2DMA during degradation in PBS was measured.

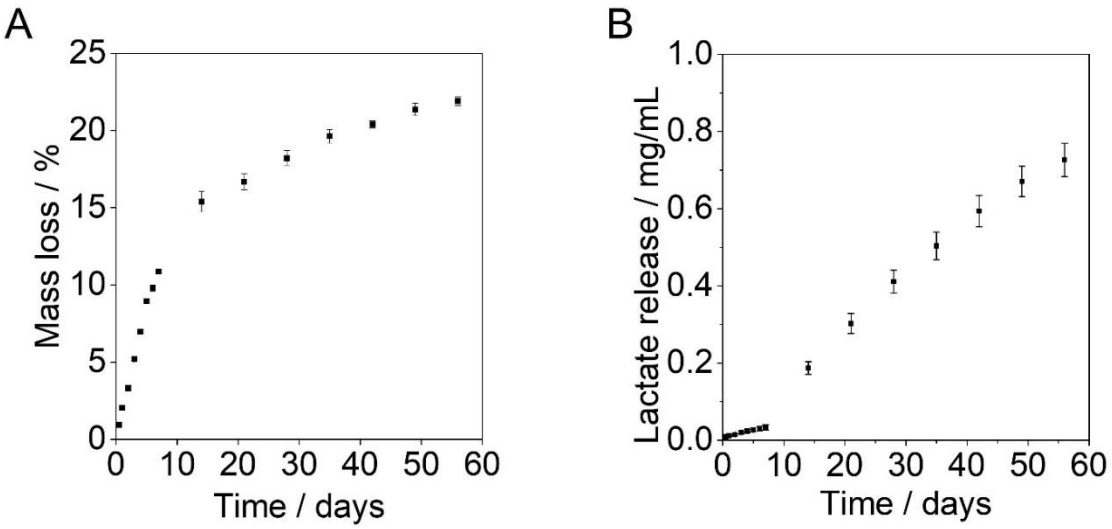

Figure 2-8. Degradation of P_7L_2DMA and the main degradation product. (A) Weight loss of P_7L_2DMA after immersion in PBS within 56 days (8 weeks). (B) Cumulative release of Lactate as main degradation product of P_7L_2DMA after immersion in PBS within 56 days (8 weeks).

To further verify the exosome release mechanisms and confirm the relationship between exosome release kinetics and P_7L_2DMA degradation, the mass loss of P_7L_2DMA during degradation in PBS was measured. As shown in **Figure 2-8A**, 16.68 ± 0.51% and 21.90 ± 0.29% of P_7L_2DMA was eroded within 21 and 56 days, respectively. Considering the exosome release was 31.19 ± 0.27% on day 21, which was higher than the mass loss of P_7L_2DMA at the same time point, the release kinetics of exosome from P_7L_2DMA was based on a combination of diffusion and erosion. To further validate the hypothesis, we measured the release of lactate, which is presumed to be the primary hydrolysis product of P_7L_2DMA based on the established hydrolysis mechanism (**Figure 2-8B**).[138] The results demonstrated a consistent release of lactate throughout the entire testing period, with the concentration of lactate in the degradation solution on day 56 recorded at 0.72 mg/mL. This finding confirmed material erosion during water immersion of P_7L_2DMA, with lactate identified as one

of the key degradation products.

The above results suggested that our microneedle system could achieve a programmable therapeutic delivery matching the wound healing process by suppressing initial inflammation while promoting long-term angiogenesis and cell migration. In particular, this long-term exosome release is a breakthrough in using microneedles for biomacromolecule (e.g., proteins, cytokines) delivery, which usually lasts for 3 days due to the low-density polymer network of the microneedle patch materials.

2.3.5 *In vitro* anti-inflammatory effect of the core-shell microneedle patch

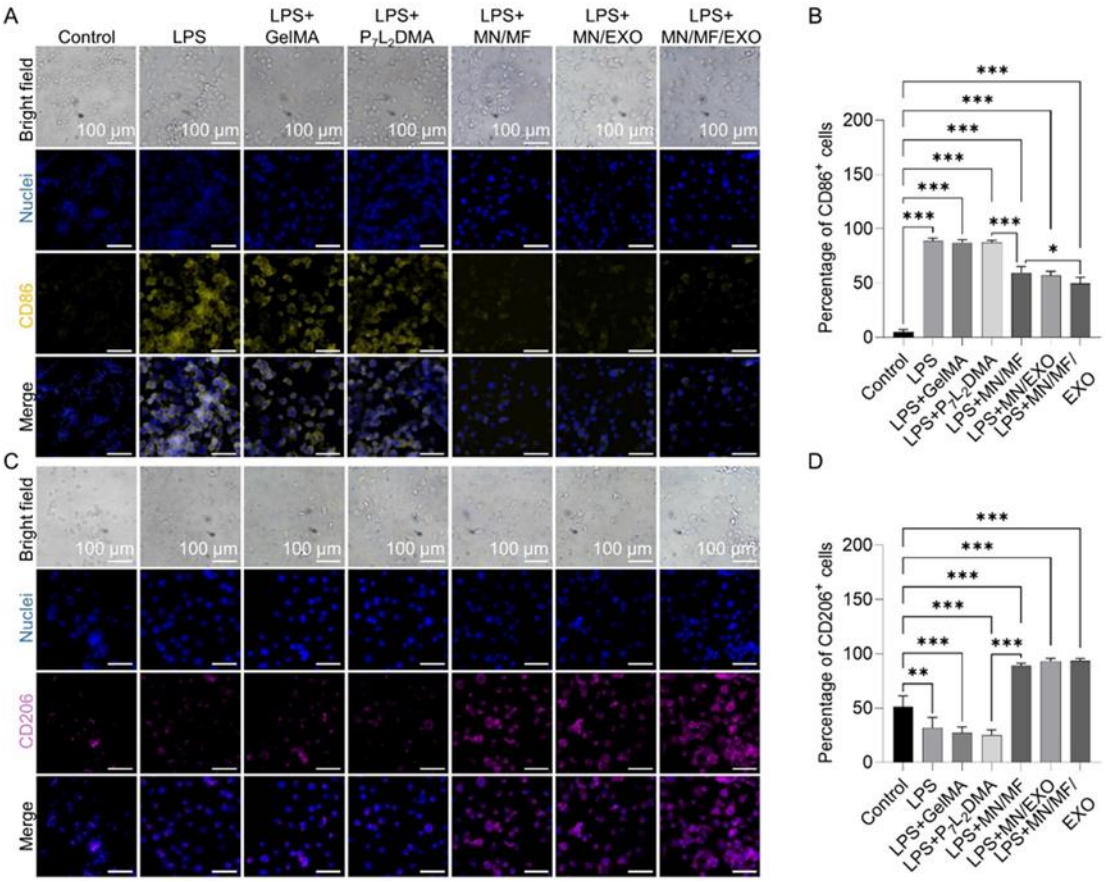

Figure 2-9. Immunoregulatory effect of different components in core-shell microneedles. (A) RAW 264.7 cells cultured in extraction solution of different groups

for 48 h marked with CD86 (yellow) and DAPI (blue). (B) Quantitative analysis of percentage of $CD86^+$ cells in different groups. (C) RAW 264.7 cells cultured in extraction solution of different groups for 48 h marked with CD206 (pink) and DAPI (blue). (D) Quantitative analysis of percentage of $CD206^+$ cells in different groups. The differences are statistically significant when p values are below 0.05 (*), 0.01 (**), and 0.001 (***).

We next characterized the anti-inflammatory effects of the microneedle *in vitro*. Our target was the prolonged inflammation in wounds, which usually impedes wound healing and leads to extracellular matrix (ECM) degradation or even chronic wounds. Anti-inflammation and immunoregulation is not only beneficial to angiogenesis that follows, but also to scar reduction.[139-141] As noted in the previous section, we loaded mangiferin into the GelMA shell for its anti-oxidant, anti-inflammatory, and anti-microbial properties[142], all of which are beneficial at the early stage of wound healing. We also loaded hMSC-derived exosomes into P_7L_2DMA to suppress inflammation in the long term.

Since macrophages are the primary mediators of inflammation after injury, we first studied the immunomodulatory and anti-inflammatory effect *in vitro* using RAW 264.7 cells, via immunofluorescence staining of the M1 phenotype marker protein CD86, M2 phenotype marker protein CD206, anti-inflammatory factor IL-10 and pro-inflammatory factor TNF-α. Regarding determining the concentrations of mangiferin and exosome, we mainly referred to previous studies. For mangiferin, concentration ranging from 20 to 200 μg/mL is usually used in *in vitro* tests.[143] Many articles

have used mangiferin at 100 μg/mL and achieve a good anti-inflammatory and cytoprotective effect.[144-147] Therefore, 100 μg/mL was chosen as the working concentration in this study. For exosome, most articles investigating exosomes have chosen 100-500 μg/mL as the working concentration.[115, 116, 148, 149] However, most of them were directly applied to the wound or encapsulated in hydrogels with fast release rate. Considering that the exosomes loaded in P_7L_2DMA would be slowly released, 1 mg/mL was chosen as the working concentration in this study. In summary, 100 μg/mL mangiferin and 1 mg/mL exosome were used in the following *in vitro* cell experiments.

Table 2. Abbreviations of sample groups for *in vitro* experiments on anti-inflammatory effect, tube formation, and scratch wound healing

Abbreviation	Full name and setting
Control	PBS
LPS	100 ng/mL lipopolysaccharides
GelMA	GelMA extraction
P_7L_2DMA	P_7L_2DMA extraction
MN/MF	100 μg/mL mangiferin loaded GelMA shell/ P_7L_2DMA core microneedle extraction
MN/EXO	GelMA shell/1 mg/mL exosome loaded P_7L_2DMA core microneedle extraction
MN/MF/EXO	100 μg/mL mangiferin loaded GelMA shell/1 mg/mL exosome loaded P_7L_2DMA core microneedle extraction

To investigate the anti-inflammatory and immunoregulatory effect of different components in microneedles, extraction solution of different groups including control, LPS, P_7L_2DMA, GelMA, MN/MF (100 μg/mL mangiferin-loaded microneedle), MN/EXO (1 mg/mL exosome-loaded microneedle), and the MN/MF/EXO (100 μg/mL mangiferin and 1 mg/mL exosome-loaded microneedle) were used in the

experiment (**Table 2**). All extraction solutions were supplemented with 100 ng/mL LPS and applied to the macrophages for 48 h. From the bright field images of **Figure 2-9A** and **Figure 2-9C**, macrophages in all treatment group showed a larger cell area than the control groups, preliminarily indicating a phenotypic transformation. **Figure 2-9B** shows the quantitative analysis of the percentage of $CD86^+$ cells in different groups, where LPS group (88.95 ± 2.15%) has a significantly higher percentage of $CD86^+$ cells compared with the control group (4.99 ± 2.01%), proving a successful induction of the M1 transition by LPS. GelMA (87.33 ± 2.40%) and P_7L_2DMA (87.56 ± 1.63%) groups showed similar CD86 level compared with the LPS group, indicating no obvious effect on immunoregulation. However, the MN/MF (59.77 ± 4.68%), MN/EXO (56.97 ± 3.48%), and especially the MN/MF/EXO (49.55 ± 5.06%) group significantly decreased the proportion of $CD86^+$ cells, suggesting that both mangiferin and exosome can promote the M1-M2 transition of the macrophages. Similarly for **Figure 2-9D**, GelMA (27.21 ± 4.74%) and P_7L_2DMA (25.22 ± 4.24%) groups showed similar CD206 level with the LPS (31.94 ± 8.36%) group, indicating no obvious effect on immunoregulation, while the MN/MF (89 ± 2.04%), MN/EXO (93.13 ± 2.41%), and the MN/MF/EXO (93.53 ± 1.93%) group significantly increased the proportion of $CD206^+$ cells compared with the control (51.44 ± 8.63%) and LPS group, indicating good immunoregulatory effects of the drugs.

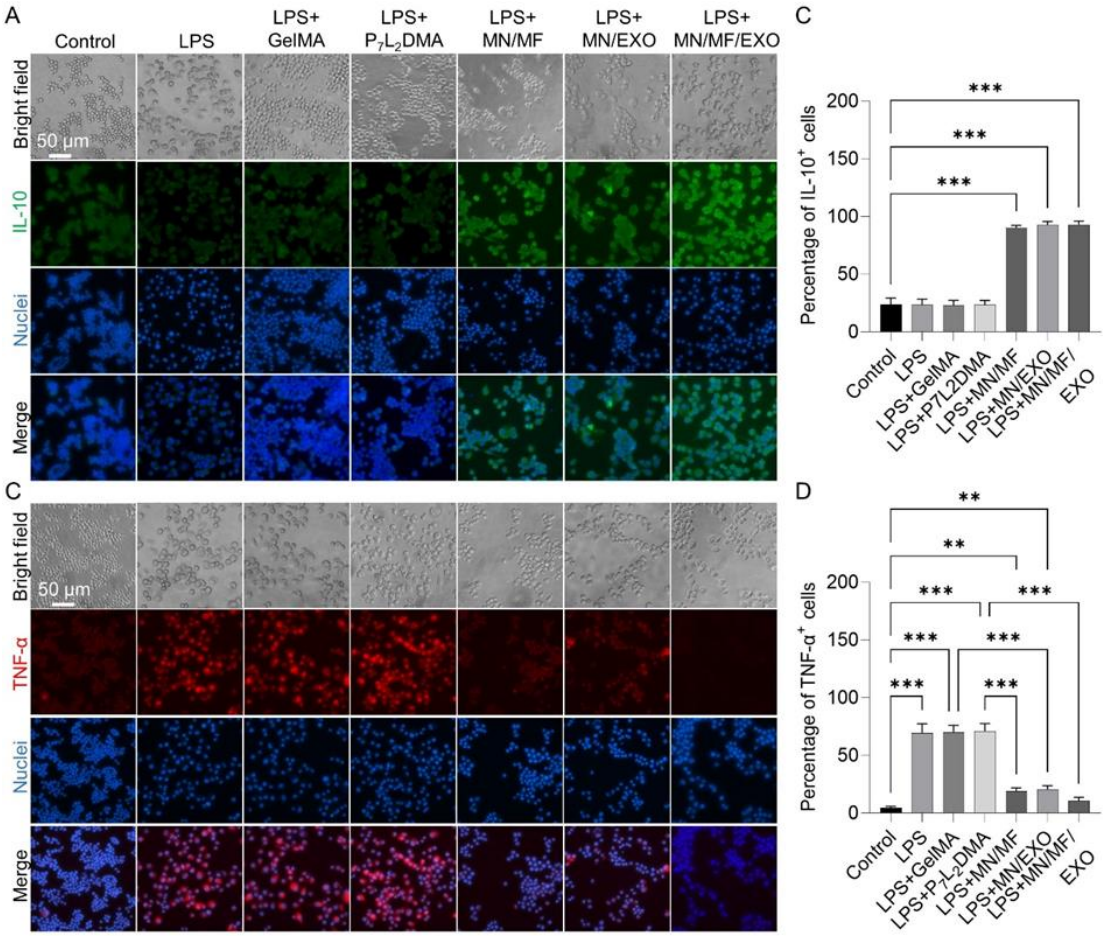

Figure 2-10. Anti-inflammatory effect of different components in core-shell microneedles. (A) RAW 264.7 cells cultured in extraction solution of different groups for 48 h marked with IL-10 (green) and DAPI (blue). (B) Quantitative analysis of percentage of IL-10$^+$ cells in different groups. (C) RAW 264.7 cells cultured in extraction solution of different groups for 48 h marked with TNF-α (red) and DAPI (blue). (D) Quantitative analysis of percentage of TNF-α$^+$ cells in different groups. The differences are statistically significant when p values are below 0.01 (**) and 0.001 (***).

Figure 2-10 also shows IL-10 and TNF-α immunostaining results to further confirm the anti-inflammatory effect of the core-shell microneedle. In brief, **Figure 2-10B**

shows the quantitative analysis of IL-10^+ cells in different groups, where GelMA (23.16 ± 3.72%) and P7L2DMA (23.62 ± 3.72%) groups showed similar IL-10 level compared with the LPS (23.48 ± 4.28%) group, indicating no obvious effect on anti-inflammation. However, the MN/MF (90.23 ± 1.84%), MN/EXO (92.83 ± 2.48%), and the MN/MF/EXO (93.09 ± 2.56%) group had higher level of IL-10 expression than the LPS group, proving good anti-inflammatory effect of these two drugs (mangiferin and exosome). Similarly for TNF-α expression (**Figure 2-10D**), GelMA (70.04 ± 5.22%) and P_7L_2DMA (71.16 ± 5.62%) groups showed similar TNF-α level with the LPS (69.48 ± 6.87%) group, indicating no obvious effect on anti-inflammation, while the MN/MF (19.20 ± 2.33%), MN/EXO (20.74 ± 2.63%), and especially the MN/MF/EXO (10.65 ± 2.70%) group significantly downregulated the TNF-α expression compared with the LPS group, indicating good anti-inflammatory effects of the drugs.

These results suggested that both the released mangiferin and exosomes showed good immunoregulatory effect and inhibited inflammation in vitro. More importantly, these results showed that P_7L_2DMA preserved the activity of exosomes, which is crucial for long-term treatment of wound healing. We thus believe the core-shell microneedle patch with programmed release of mangiferin and exosome would achieve an effective and long-term anti-inflammation efficacy in our in vivo experiment in later sections.

2.3.6 *In vitro* angiogenesis and wound healing of the core-shell microneedle patch

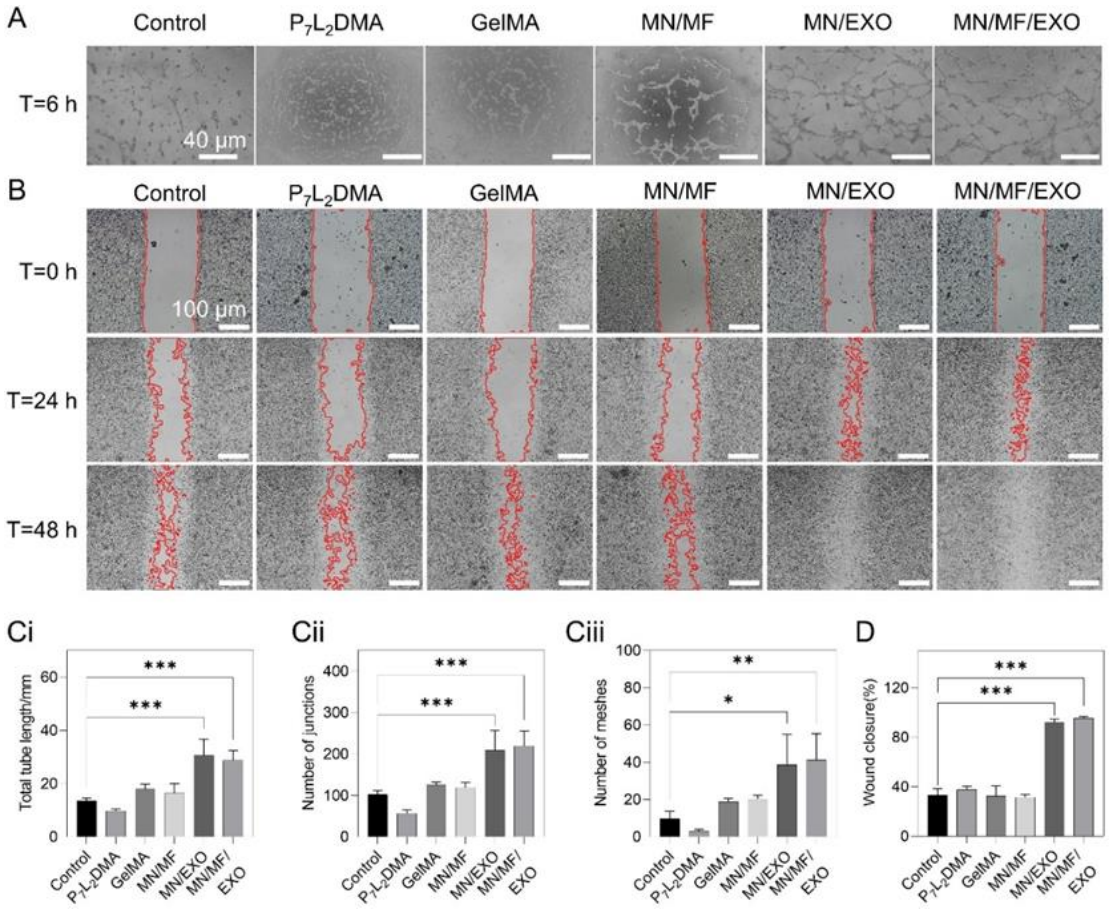

Figure 2-11. Angiogenesis and *in vitro* wound healing effect of different components in microneedles. (A) Representative bright-field images of HUVECs cultured in extracts from different groups at 6 h. (B) Representative bright-field images of L929 fibroblasts cultured in extracts from different groups at different time points (0, 24, 48 h) (red lines indicate wound borders). (C) Quantitative analysis of tube formation in different groups using ImageJ. (i) Total tube length, (ii) number of junctions, (iii) number of meshes. (D) Quantitative analysis of wound closure rate in different groups at 24 h using ImageJ. The differences are statistically significant when p values are below 0.05 (*), 0.01 (**), and 0.001 (***).

Angiogenesis and cell migration capacity are also critical in the wound healing process. For these two aspects, we investigated tube formation and migration of L929 fibroblasts and HUVECs. Extraction solutions of six groups, including control, P_7L_2DMA, GelMA, MN/MF, MN/EXO, and MF/MF/EXO were used in the tests (**Table 2**).

We first cultured HUVECs with the extraction solutions for 6 h and examined tube formation. As shown in **Figure 2-11**A, MN/EXO and MN/MF/EXO groups both showed apparent tube formation in most areas. As for the control, GelMA, and MN/MF groups, only few short cell connections were observed. For quantitative measurement, we evaluated the total tube length, number of junctions, and number of meshes (**Figure 2-11**Ci-iii). Consistent with our observations, all three measurements were significantly higher in the MN/EXO and MN/MF/EXO groups compared with the remaining groups, suggesting the pivotal role of exosome on tube formation and angiogenesis.

For cell migration, **Figure 2-11B** shows the wound closure rate of different groups at 0, 24, and 48 h. For fibroblast migration experiment, the MN/EXO and MN/MF/EXO groups showed accelerated wound closure with average closure rate of 91.88 ± 2.34% and 95.40 ± 1.18%, respectively. Meanwhile, the control, P_7L_2DMA, GelMA, and MN/MF groups showed no significant differences with wound closure rate of 33.32 ± 4.21%, 37.65 ± 2.27%, 32.46 ± 6.82%, 31.47 ± 1.89%, respectively.

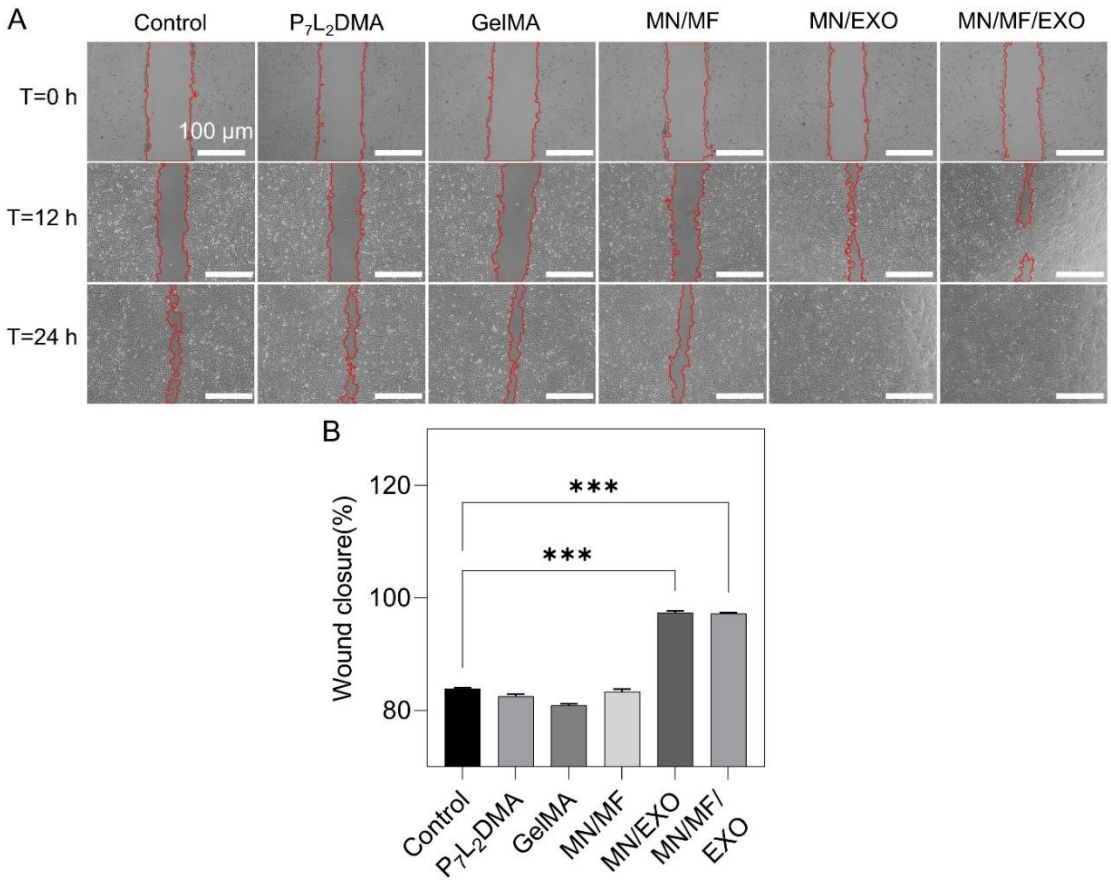

Figure 2-12. *In vitro* wound healing effect of different components in microneedles based on HUVECs. (A) Representative bright-field images of HUVECs cultured in extracts from different groups at different time points (0, 12, 24 h) (red lines indicate wound borders). (B) Quantitative analysis of wound closure rate in different groups at 12 h using ImageJ. The differences are statistically significant when p values are below 0.001 (***).

In **Figure 2-12**, the cell migration experiment of HUVECs shows similar results, with MN/EXO and MN/MF/EXO groups exhibiting the fastest wound closure rate among all groups. The MN/EXO and MN/MF/EXO groups showed accelerated wound closure with average closure rate of 97.40 ± 0.34% and 97.22 ± 0.22% respectively. Meanwhile, the control, P_7L_2DMA, GelMA, and MN/MF groups showed no

significant differences in wound closure rate (83.88 ± 0.19%, 82.51 ± 0.42%, 80.91 ± 0.28%, and 83.31 ± 0.52% respectively). This indicates that the released exosomes were critical for promoting cell migration. All the above results suggested that the core-shell microneedle patch improved angiogenesis and migration of fibroblast and HUVECs *in vitro*. The current drug loading concentration will also be used in the following *in vivo* tests.

Table 3. Abbreviations of sample groups for *in vivo* experiment.

Abbreviation	Full name and setting
Blank	PBS
Pure MN	GelMA shell/ P_7L_2DMA core microneedle
MN/MF	100 μg/mL mangiferin loaded GelMA shell/ P_7L_2DMA core microneedle
MN/EXO	GelMA shell/1 mg/mL exosome loaded P_7L_2DMA core microneedle
MN/MF/EXO	100 μg/mL mangiferin loaded GelMA shell/1 mg/mL exosome loaded P_7L_2DMA core microneedle

2.3.7 *In vivo* therapeutic effect of the core-shell microneedle patch

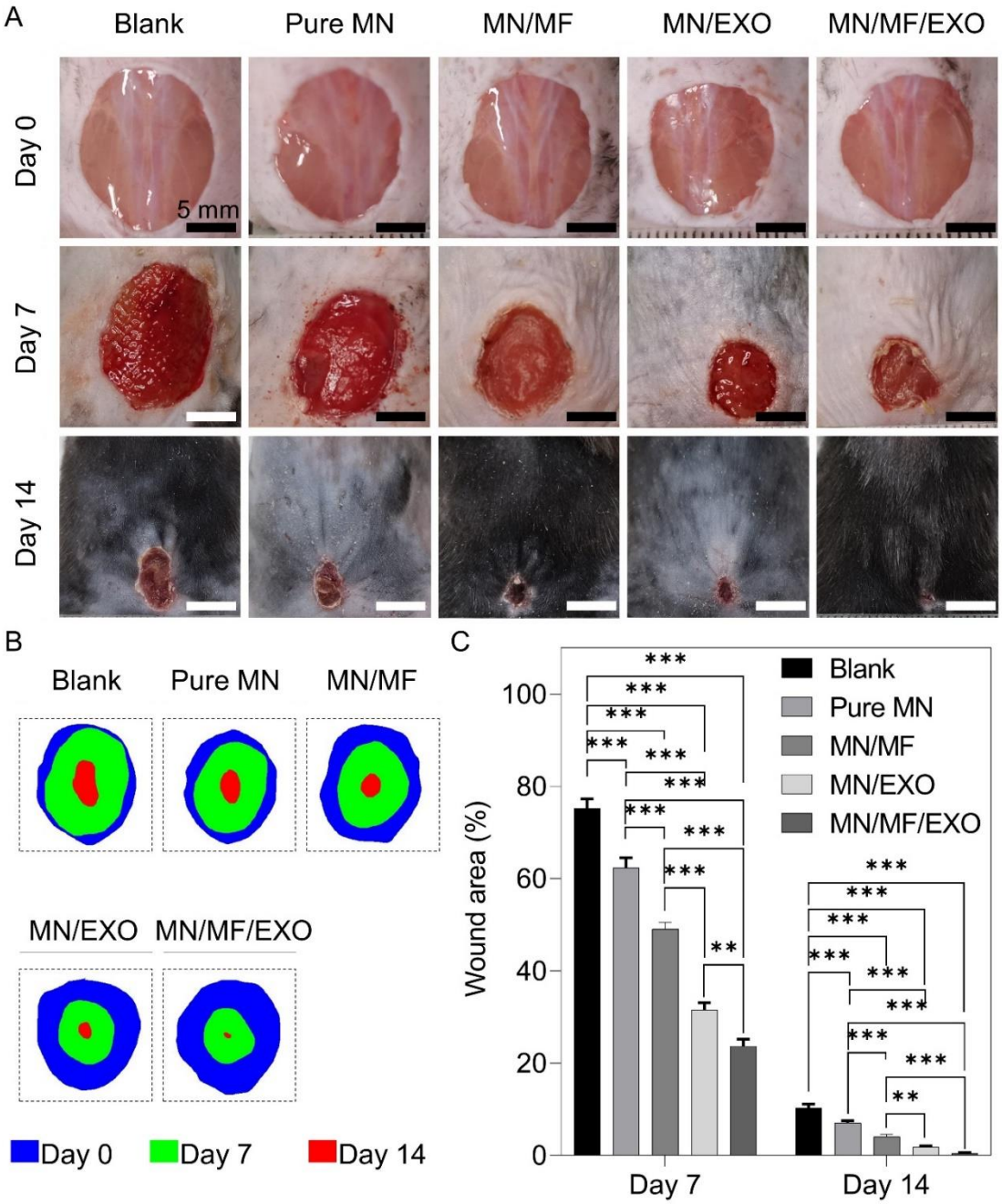

Figure 2-13. Assessment of *in vivo* wound closure rate. (A) Images of wound healing in different groups: blank, pure MN, MN/MF, MN/EXO, and MN/MF/EXO on days 0, 7, and 14. Scale bar, 5 mm. (B) Diagrams of wound area at different time points. Blue, green, and red indicate days 0, 7 and 14, respectively. (C) Quantitative analysis of wound area in different groups on days 7 and 14. The differences are statistically significant when p values are below 0.01 (**), and 0.001 (***).

The excisional wound model is one of the common mouse models to investigate skin regeneration and scarless wound healing.[150] For our experiment, we created an excisional, full-thickness wound on mouse dorsal skin. Then – except for the blank group (i.e., no treatment) – pure MN, MN/MF, MN/EXO, or MN/MF/EXO group was directly applied to the wound bed (**Table 3)**.

Images were taken on days 0, 7, and 14, to illustrate how the wounds changed (**Figure 2-13A-B)**. We evaluated wound closure rate using the wound areas on days 7 and 14 relative to the original wound area on day 0 (**Figure 2-13C**). The resulting wound closure rates were as follows (on days 7 and 14; lower indicates quicker healing): 75.26 ± 2.00% and 10.32 ± 0.83% in blank group; 62.43 ± 2.09% and 7.07 ± 0.48% in pure MN group; 49.10 ± 1.38% and 4.11 ± 0.49% in MN/MF group; 31.57 ± 1.54% and 1.83 ± 0.26% in MN/EXO group; 23.66 ± 1.50% and 0.49 ± 0.16% in MN/MF/EXO group. From the results, the MN/MF, MN/EXO, and MN/MF/EXO groups recovered over 50% on day 7 and over 95% on day 14, which was significantly faster than the blank and pure MN groups, indicating a critical effect of either exosomes or mangiferin, as well as when they were used together.

Interestingly, the pure MN group also showed a better recovery than the blank group on both day 7 (62.43% healed in the blank group compared to 75.26% healed in the MN group) and day 14 (7.07% healed in the blank group compared to 10.32% in the

MN group). This can be attributed to hydration effect of the GelMA and the water retention effect of the P_7L_2DMA patch on the wound area (data not shown). Hydration is a crucial external factor for optimal healing, known as moist wound healing, which has been demonstrated to enhance epithelialization rate and reduce scarring.[151, 152] GelMA, an extensively studied hydrogel biomaterial, is recognized for its excellent hydration properties attributed to its swelling characteristics and high porosity.[153] It efficiently absorbs interstitial fluid and exudate upon application to the wound, preventing rapid loss of wound moisture. Various forms of GelMA, such as hydrogel blocks,[154, 155] electrospun membranes,[91] and microneedles,[156, 157] have been proven to accelerate wound closure. In our system, GelMA needle tips rapidly absorb wound interstitial fluid, providing localized moisturization. Moreover, the P_7L_2DMA in the microneedle substrate, which covers the entire wound, exhibits significant hydrophobicity as demonstrated in our previous research.[111, 119] When crosslinked, it forms a dense polymer network with a low water vapor transmission rate, effectively preserving the wound moisture and complementing the hydrating properties of GelMA. In conclusion, the combination of the GelMA shell and the P_7L_2DMA substrate design synergistically maintains wound moisture, resulting in a beneficial hydration effect.

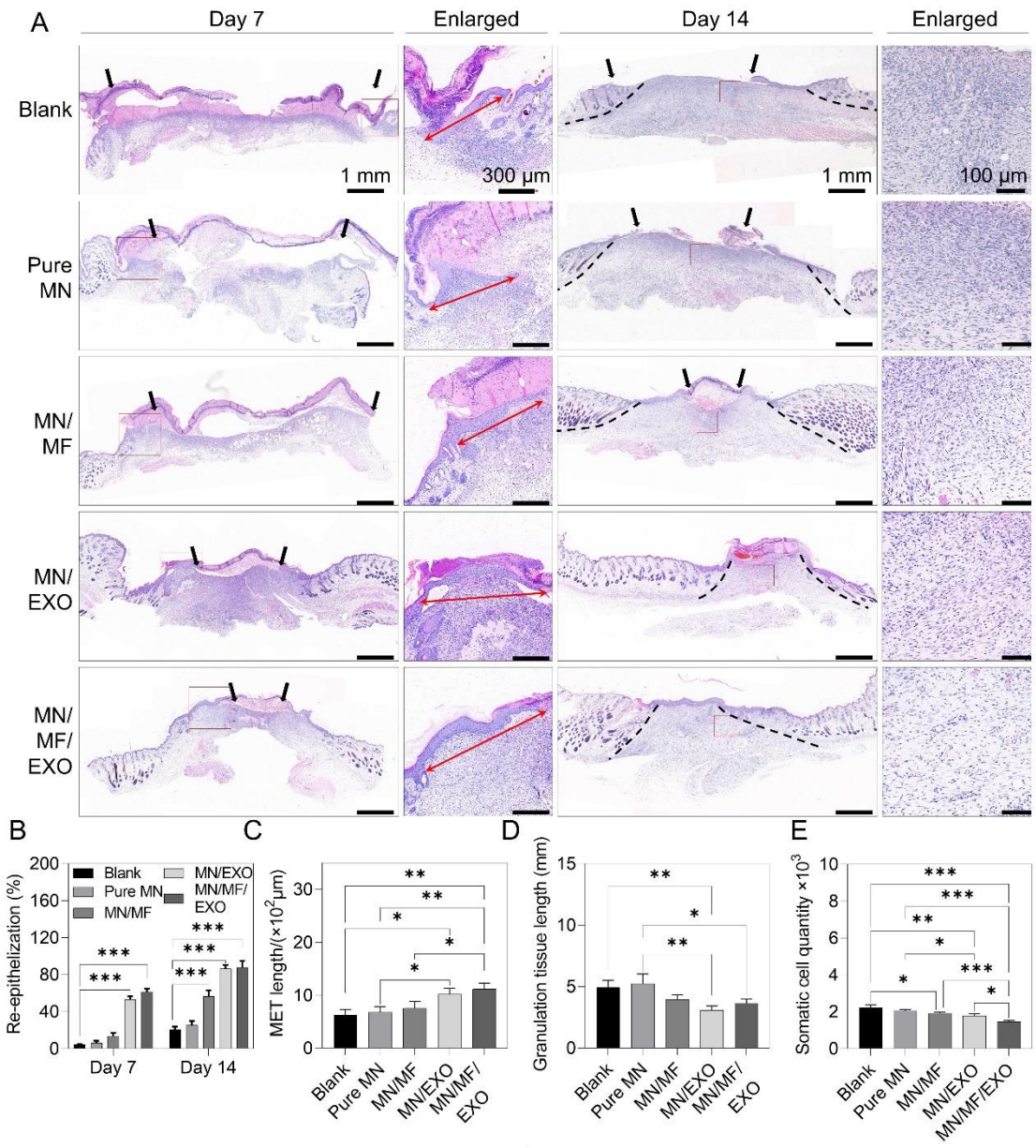

Figure 2-14. Histological evaluation of wounds using H&E staining. (A) Representative H&E staining images of the wound tissues treated with different groups after 7 and 14 days: blank, pure MN, MN/MF, MN/EXO, and MN/MF/EXO. Black arrow indicates the border of the migrating epidermal tongue (MET). Black dotted line indicates the granulation tissue border. Enlarged views of day 7 images show the METs in wounds. Red double-sided arrow indicates the MET length. Enlarged views of day 14 images show the distribution of somatic cells in the center

of the granulation tissues. (B) Quantitative analysis of re-epithelialization ratio of different groups on days 7 and 14. (C) Quantitative analysis of MET lengths of different groups on day 7. (D) Quantitative analysis of granulation tissue lengths of different groups on day 14. (E) Quantitative analysis of somatic cell numbers of different groups on day 14. The differences are statistically significant when p values are below 0.05 (*), 0.01 (**), and 0.001 (***).

The wound healing effect of different groups was further analyzed through histology. **Figure 2-14A** shows representative H&E staining images on days 7 and 14 of the wound tissues of different groups. Low-magnification images were used to observe the general re-epithelialization, inflammation, and granulation tissue morphology. Quantitative re-epithelialization ratio was also measured (**Figure 2-14B**). On day 7, the MN/MF/EXO (61.30 ± 3.51%) and MN/EXO groups (53.00 ± 3.61%) demonstrated significantly more re-epithelialization than other groups (blank 4.33 ± 0.58%; pure MN 6.00 ± 2.65%; MN/MF 13.33 ± 3.51%). On day 14, three groups (MN/MF/EXO 87.67 ± 7.10%; MN/EXO 86.33 ± 4.04%; MN/MF 56.33 ± 6.51%) showed significantly more re-epithelialization than other groups (blank 20.67 ± 3.06%; pure MN 25.33 ± 4.51%). In addition, the MET length, which also represents the re-epithelialization capacity, was marked in the enlarged view of images on day 7 and quantitatively analyzed (**Figure 2-14C**). On day 7, MN/MF/EXO and MN/EXO groups showed the longest MET length while the other three groups showed no significant difference. These results proved that mangiferin and especially exosomes

greatly promoted cell migration in the wound bed, leading to faster re-epithelialization. On day 14, granulation tissue maturation was observed in MN/MF, MN/EXO, and especially MN/MF/EXO groups, with the presence of paler scars and absence of inflammatory cells from the enlarged view. Moreover, hair follicles were generated in the MN/MF/EXO group, suggesting a successful recovery of functional and healthy skin tissues, which was consistent with the systemic regenerative effect of exosomes reported in the literature.[158] As the scar formation is mainly due to the excessive matrix deposition of somatic cells like fibroblasts and myofibroblasts, somatic cell quantity was adopted as a preliminary indicator for assessing scar formation.[25, 159] Quantitative results also indicated that significant decrease in granulation tissue length and somatic cell quantity occurred in the MN/MF, MN/EXO, and MN/MF/EXO groups (**Figure 2-14D-E**), indicating a trend in reducing scar formation by these treatments. Overall, our results demonstrated that mangiferin and exosomes greatly facilitated wound closure and re-epithelization of skin wounds.

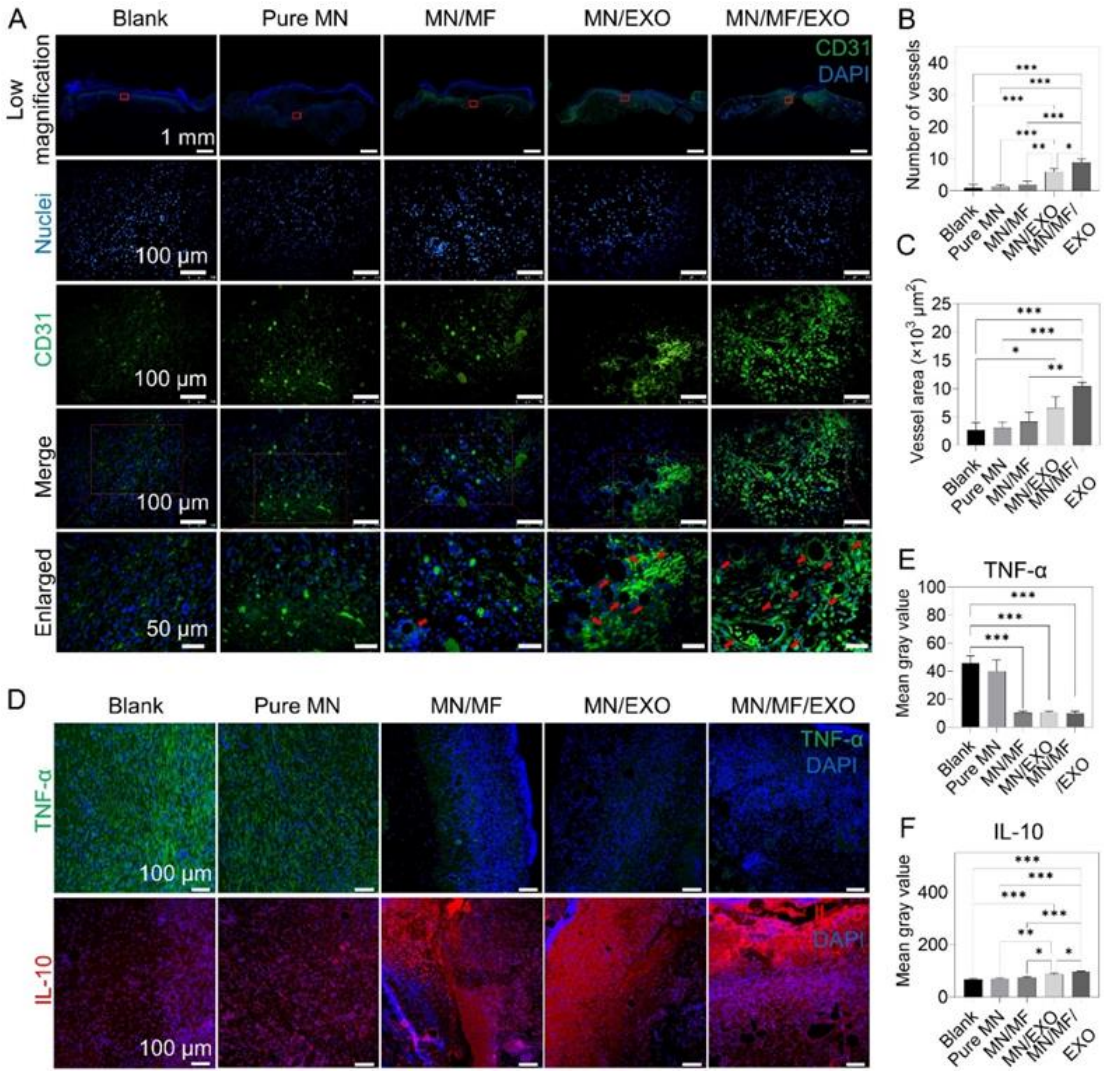

Figure 2-15. *In vivo* angiogenesis and anti-inflammation effect of different groups on day 7. (A) Representative immunofluorescence images of different groups stained with CD31 (green) and DAPI (blue). Red boxes in the low magnification indicate the target areas. Red arrow indicates blood vessels in wound tissues. (B) Quantitative analysis of the number of blood vessels in wound tissues. (C) Quantitative analysis of the blood vessel area in wound tissues. (D) Representative immunofluorescence images of different groups stained with IL-10, TNF-α, and DAPI. (E-F) Quantitative analysis of immunofluorescence intensity of IL-10 and TNF-α in different groups. The differences are statistically significant when p values are below 0.05 (*), 0.01

(**), and 0.001 (***).

To elucidate the underlying mechanism of accelerated wound healing, we examined the signs of early inflammation and angiogenesis in tissue sections on day 7 using CD31 (angiogenesis marker), IL-10 (anti-inflammatory marker), and TNF-α (pro-inflammatory marker) immunostaining. **Figure 2-15A** shows the representative images of CD31 in different groups, and the blood vessel number and vessel area were analyzed in **Figure 2-15B-C**. Similar to our other *in vitro* results, the exosomes provided excellent systemic regeneration effect, making the MN/MF/EXO group having the most blood vessel number and vessel area compared to the other groups, followed by the MN/EXO group. The remaining groups showed no significant difference in the CD31 expression. For anti-inflammation, **Figure 2-15D** shows the representative images of IL-10 and TNF-α in different groups and average fluorescence intensity was quantified in **Figure 2-15E-F**. We found that mangiferin and exosomes significantly decreased the TNF-α expression and elevated the IL-10 expression, indicating the presence of anti-inflammatory response. The combination of mangiferin and exosomes had stronger anti-inflammatory effect compared to either of the individual treatment, indicating a synergetic long-term anti-inflammatory effect when the two treatments were combined. Altogether, our core-shell microneedles successfully demonstrated the ability to inhibit inflammation and promote angiogenesis *in vivo*.

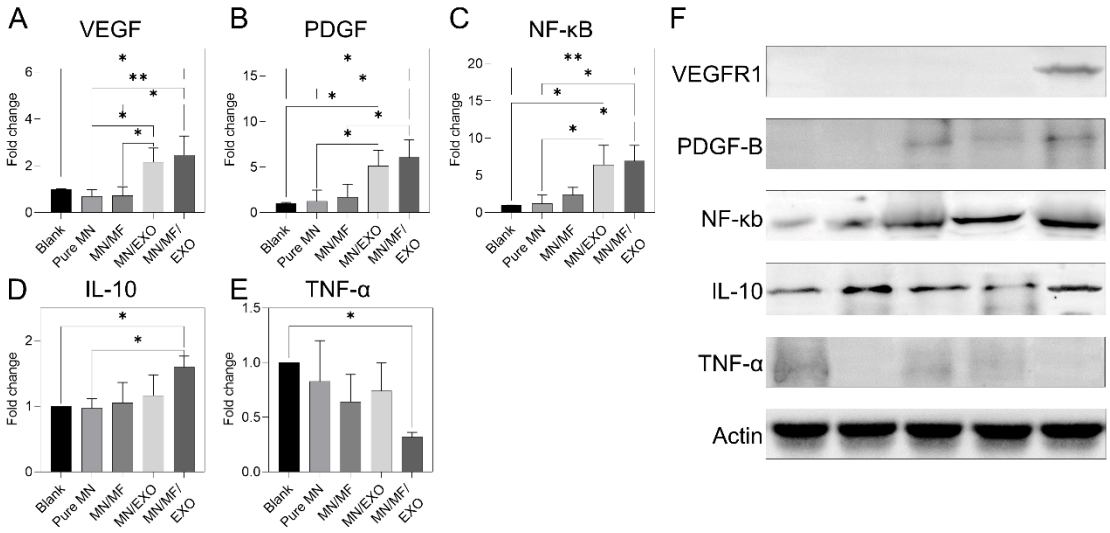

Figure 2-16. Inflammation- and angiogenesis-related gene expressions in wound bed of different groups. (A)-(E) Real-time quantitative polymerase chain reaction (RT-qPCR) results of vascular endothelial growth factor (VEGF), platelet-derived growth factor (PDGF), nuclear factor kappaB (NF-κB), IL-10, and TNF-α expressions in wound bed of different groups on day 7. (F) Western blot analysis of VEGFR1, PDGF-B, P65, IL-10, and TNF-α expression in the wound bed of different groups on day 7. The differences are statistically significant when p values are below 0.05 (*) and 0.01 (**).

We further verified the anti-inflammatory and angiogenic effect via real-time quantitative polymerase chain reaction (RT-qPCR) and western blot (**Figure 2-16**). The markers we chose included vascular endothelial growth factor (VEGF; a classic marker for neovascularization), platelet derived growth factor (PDGF; a classic marker for stability of neovascularization), and nuclear factor-kappaB (NF-κB; a key mediator associated with exosome-induced angiogenesis in endothelial cells). According to **Figure 2-16**, expression of VEGF, PDGF, and NF-κB were

significantly higher in the MN/MF/EXO and MN/EXO groups than the other three groups, indicating that our MSC-derived exosomes released from the core-shell microneedles could elevate the VEGF and PDGF expression and activate the NF-κB signaling pathway for promoting angiogenesis. This was consistent with the immunostaining results which demonstrated the angiogenesis activity of the released exosome. We also evaluated the two inflammatory markers, IL-10 and TNF-α, to further support our previous data (**Figure 2-15**). As shown in **Figure 2-16**, IL-10 showed higher expression and TNF-α showed lower expression only in the MN/MF/EXO group, indicating that our mangiferin and MSC-derived exosomes released from the core-shell microneedle patch can inhibit inflammation *in vivo*.

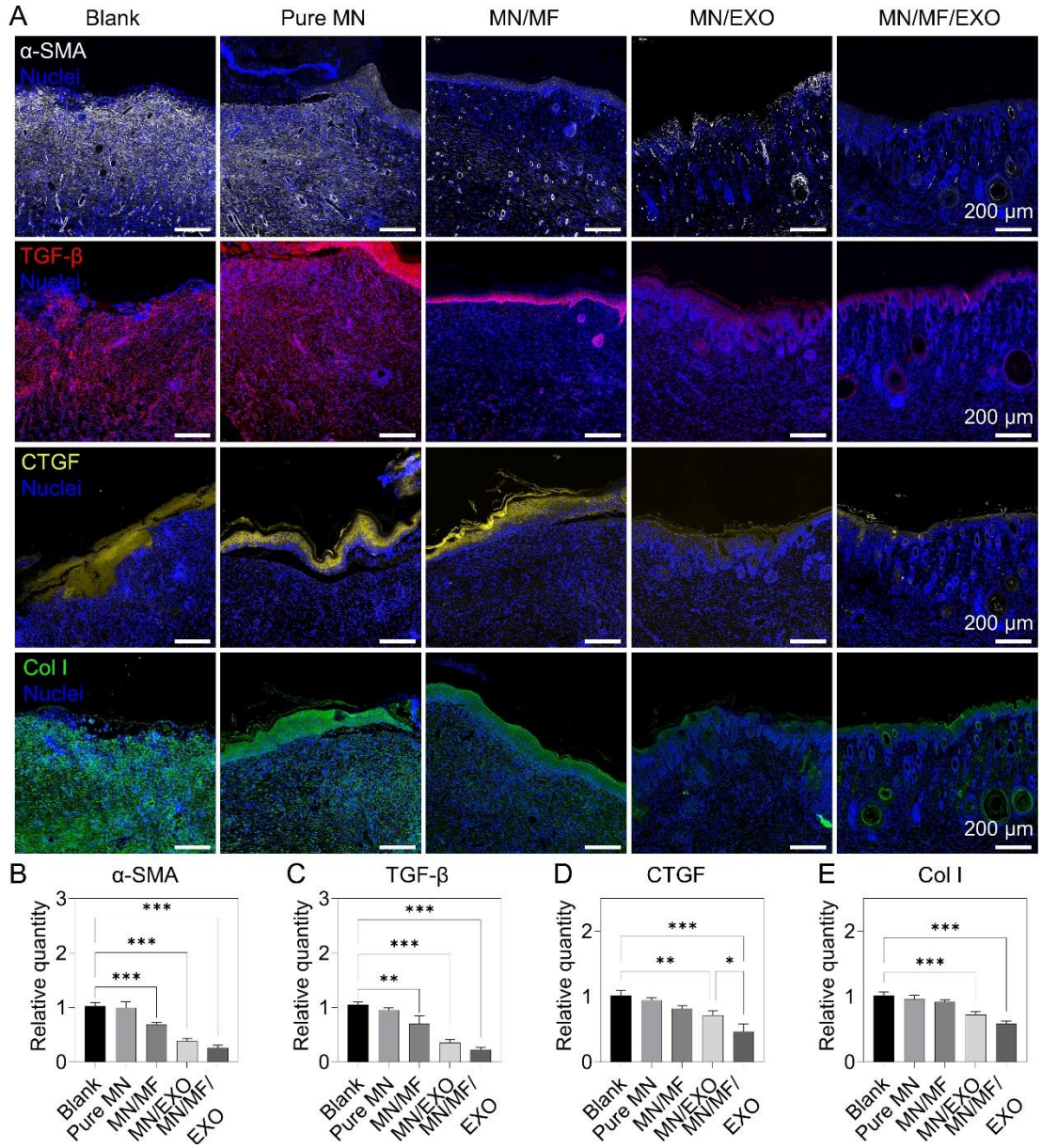

Figure 2-17. *In vivo* scar formation of wounds treated with different groups on day 14. (A) Representative immunofluorescence images of different groups stained with four scar-related proteins: α-smooth muscle actin (α-SMA, white), transforming growth factor-β (TGF-β, red), connective tissue growth factor (CTGF, yellow), and collagen type I (Col I, green). (B-E) Quantitative analysis of relative quantity of fluorescence intensity in different groups for evaluating the expressions of α-SMA, TGF-β, CTGF,

and Col I in wound tissues. The differences are statistically significant when p values are below 0.05 (*), 0.01 (**), and 0.001 (***).

Apart from restoration of regulatory processes like inflammation suppression and angiogenesis, scarless skin wound healing is also another important indication of functional skin recovery. We hypothesized that exosomes and mangiferin combined could inhibit myofibroblast activations, regulate ECM deposition and the skin microenvironment for less scar formation.[90, 92, 160] Therefore, we evaluated scar formation in the regenerated wounds of different groups after 14 days. The following scar-related proteins were selected for immunostaining: α-smooth muscle actin (α-SMA; representing myofibroblasts that secrets ECM and is responsible for wound contraction and scar formation[161]), transforming growth factor-β (TGF-β; representing ECM deposition and the associated stress environment in the wound area), connective tissue growth factor (CTGF; a key mediator for pathways involving myofibroblast activation, ECM deposition, and fibrosis, as well as a key marker for hypertrophic scars and keloids[162-164]), and collagen type I (Col I; a major component of scar in general). **Figure 2-15** illustrates the resulting wound sites of different microneedle groups. The MN/MF/EXO group – followed by MN/EXO and then MN/MF – showed the lowest expressions of all markers. Several structural differences could also be observed among different microneedle groups. For instance, TGF-β was not observed in the MN/MF/EXO group, persisted slightly in the newly formed epidermis of MN/EXO and MN/MF groups, and distributed abundantly and

evenly in the granulation tissue of the blank and pure MN groups. Similarly, CTGF was only present as a thin layer in epidermis of the MN/MF/EXO group, which was otherwise thicker in the other groups in the following order: MN/EXO, MN/MF, pure MN, and blank. In addition, the MN/EXO and MN/MF/EXO groups had a sparse distribution of Col I with also signs of hair follicles (round or oval-shaped structures) appearing in the wound area, an indication of functional recovery. On the contrary, there was an abundance of Col I in the granulation tissue (and hence scarring) of the blank, pure MN, and MN/MF groups. All these results suggested that our core-shell microneedle patch could greatly reduce scar formation by regulating several key cytokines, including α-SMA, TGF-β, and CTGF. In particular, the hMSC-derived exosomes played a vital role with systemic improvement and regulation of scar-related cytokines, while mangiferin primarily affected the α-SMA and TGF-β expressions to suppress inflammation.

Altogether, the combination of exosomes, mangiferin, and the core-shell microneedle patch greatly enhanced wound healing by promoting anti-inflammation, angiogenesis, cell migration, and scar reduction. Attributed to the system design and material selection of our core-shell microneedle patch, these two drugs could be delivered programmatically to match the two different phases of wound healing: the inflammatory phase and the regenerative phase. Importantly, our choice of the core material, P_7L_2DMA, can encapsulate and release biomacromolecules in a sustained way without losing their activity, enabling the long-term effect of exosomes for

promoting anti-inflammation, angiogenesis, cell migration, and ECM reorganization at later stage of wound healing (i.e., proliferation, remodeling). This is a breakthrough to the current hydrogel-based microneedle systems which can only release encapsulated therapeutics in a short term and cannot address the full process of wound healing.

2.4 Summary

In summary, we have fabricated a PGLADMA/GelMA core-shell microneedle patch incorporating mangiferin and hMSC-derived exosomes to address scarless skin wound healing. The benefit of this core-shell structure is the rapid release of mangiferin from the GelMA shell for early inflammation suppression, and prolonged release of exosomes from the PGLADMA core for angiogenesis and cell proliferation. Specifically, such a differential release enhanced cell migration and tube formation of HUVECs *in vitro*, suppressed pro-inflammatory cytokine TNF-α and anti-inflammatory cytokine IL-10, and promoted neovascularization with markers of the NF-κB signaling pathway (α-SMA, TGF-β, CTGF, Col I) *in vivo*. Altogether, our patch not only realized scarless skin regeneration manipulating the release dynamics of the material properties and microneedle designs, but also demonstrated for the first time a stiff hydrogel strategy for prolonged encapsulation/release of exosomes for therapeutic purposes. This provides an important guideline for future biomaterial studies taking advantage of the long-term benefits of exosome treatments, especially using hydrogel microneedles, for multi-phase tissue regeneration. However, there are

still limitations to the current research. While the 14-day *in vivo* results have demonstrated the anti-scarring efficacy of our core-shell microneedle, future animal experiments with a longer duration, such as 28 days, will be conducted to better showcase the scar reduction effect.

Chapter 3 Contractile microneedle patch for anti-scar treatment

3.1 Introduction

As a common complication in wound healing, scarring not only negatively affects the appearance and psychological well-being of patients but also impairs normal tissue and functions, resulting in significant social and economic burdens.[140, 165] Currently, scar treatments mainly include surgery, laser therapy, and drug injections. However, these methods have certain side effects and high risks, and their effectiveness is not always satisfactory. In recent years, with the continuous advancement of medical technology, anti-scar patches have emerged as a novel approach. These patches can help reduce the color, hardness, and height of scars, and they offer advantages such as convenience, safety, and non-invasiveness. Nevertheless, there are still several limitations associated with anti-scar patches, including long treatment duration and limited efficacy.[166] Therefore, further research on scar formation is needed to help design more effective and safer anti-scar products.

Current mainstream anti-scar strategies involve drug-based regulation of anti-inflammatory and antioxidant responses, drug-based regulation of wound cell proliferation and differentiation to modulate matrix deposition, as well as mechanical regulation of wound cell differentiation into scar-forming cell lineage to modulate matrix deposition.[167-169] Additionally, wound stress profoundly influences scar formation, as excessive stress can activate the integrin-FAK mechanical pathway and

promote fibroblast differentiation into scar-promoting myofibroblasts, leading to excessive matrix deposition.[10, 25] Currently, many clinical treatment methods, such as W-plasty, wound tension-reducing tapes, and silicone gel sheets, are based on the principle of stress modulation to minimize scar formation.[170]

As a novel therapeutic tool in recent decades, microneedles have been widely used in wound repair and scar inhibition. In addition to delivering drugs for scar treatment, microneedles themselves have been proven to inhibit and reduce scars. Currently, a method called medical needling has been widely applied in clinical and cosmetic industries. This method uses a roller with an array of metal microneedles to repeatedly puncture burn scars. During this process, the microneedle patches pierce the scar, puncture the vessels in dermal layer, and facilitate collagen re-deposition and skin remodeling. Consequently, the scar tissue is disrupted and replaced by normal collagen with mesh-like structure. Then, fibronectin and related proteins increase, resulting in skin with better smoothness and elasticity.[24]

Besides microneedle rollers, polymer microneedles themselves have also been proven to possess anti-scar properties. Zhang et al. developed a silk fibroin microneedle that can penetrate the dermal layer and interact with target tissues in a mechanical way, thereby modulating the stress environment and ultrastructure of the local tissue. RNA sequencing showed that this microneedle system disrupted the mechanical communication between cells and the extracellular matrix through the integrin-FAK

pathway, thereby reducing scar formation. To sum up, the use of microneedles for physical intervention could decrease mechanical transduction within scar tissue, leading to a low-stress environment and ultimately reducing the formation of scars.[25]

However, there are still limitations in the current theoretical understanding and design of anti-scar microneedles. For instance, *in vitro* models utilized to investigate the anti-scar results of microneedles cannot accurately reflect the stress conditions of human wounds. More specifically, different regions in the human skin naturally experience varying levels of tension (15-30% strain); after injury, a natural tension force from the surrounding tissues often affects cell behavior in the wound.[171] Furthermore, during the proliferative and remodeling phases of wound healing, numerous fibroblasts gather at the wound site to form an intercellular network. Inside such network, the fibroblasts secrete a significant amount of collagen and generate traction forces (i.e., wound contraction, which is a complication of scar formation).[172] Existing anti-scar microneedle patches only focus on traction forces generated by fibroblasts, while neglecting the natural tension force from the surrounding tissues.[25]

In this chapter, we propose a contractile anti-scar microneedle patch, which simultaneously regulates wound tension force and traction force. The whole system consisted of three parts: the backing layer, the middle part, and the tilted part. The backing layer was made of $P_{68}L_8$DMA, which was flexible and elastic enough to resist tension force from the surrounding tissue. The middle part was made of P_7L_2DMA,

which was stiffer to insert into the wound bed to relieve the local stress generated by myofibroblasts. The tilted part was also made of P_7L_2DMA and was inserted into the surrounding tissue for tissue adhesion and force transduction.

From our results, the contractile microneedle patch showed better tissue adhesion than pure backing layer and common microneedle patches. A fibroblast-loaded collagen system was established as an *in vitro* scar model, where the proposed microneedle system significantly reduced some scar-related protein (α-SMA, CXCL 14) expressions. A macrophage-loaded collagen system was also established to investigate the *in vitro* anti-inflammatory effects of the proposed microneedle system. Indeed, expressions of some inflammatory proteins (iNOS, TNF-α) were reduced but the anti-inflammatory protein (IL-10) expression was enhanced. RNA sequencing revealed that our patch could decrease scar formation by downregulating some mechanical signaling pathways, including focal adhesion, ECM-receptor interaction, and PI3K signaling pathway.

To our knowledge, this is the first time for an anti-scar patch to simultaneously regulate wound tension force and traction force generated by fibroblasts without drug assistance. This study lays the foundation for future clinical development of safer and more effective anti-scar microneedle products.

3.2 Methodology

3.2.1 Materials

Propylene glycol (PPG) was bought from Sigma-Aldrich (Hong Kong). Lactide (LA), methacryloyl chloride (MAC), trimethylamine (TEA), stannous octoate, trimethylamine (TEA), Irgacure 819, and 2-hydroxyethyl methacrylate (HEMA) were purchased from Macklin reagent (Shanghai, China). Dichloromethane (DCM) and diethyl ether were purchased from Duksan (Hong Kong). Collagen I (Rat tail, A10483-01), PBS (10010023), 10× PBS (70013), HBSS (14025092), DMEM (11965092), FBS (10099141C), PS (15070063), and trypsin-EDTA (25200056) were purchased from Gibco (Hong Kong). Sponges (E6061) were purchased from Beyotime (China). TRIzol reagent (Invitrogen, 15596026) was purchased from Thermo Fisher (Hong Kong).

3.2.2 Synthesis of P_mL_nDMA

Two kinds of P_mL_nDMA (i.e., P_7L_2DMA and $P_{68}L_8DMA$) were used in this chapter. The synthetic process of P_7L_2DMA has been presented in section 2.2. The synthesis of $P_{68}L_8DMA$ shared a similar process with that of P_7L_2DMA but had a different ratio of PPG to LA. In brief, under nitrogen protection, 40 g of PPG and 11.52 g of LA underwent ring-opening polymerization using stannous octoate as the catalyst for a duration of 6 hours at 150℃. Then 4.22 g MAC and 4.05 g TEA (both diluted in DCM) were added in drops at 0℃ to conjugate methacrylate groups to the polymer chain end. To remove the TEA·HCL generated during this process, the $P_{68}L_8DMA$/TEA·HCL mixture was dissolved in diethyl ether and filtered. Finally, the

residual solvent in the oil solvent phase was completely removed through 2 hours of rotary evaporation, resulting in pure $P_{68}L_8$DMA. To form the photocrosslinkable $P_{68}L_8$DMA precursor, the $P_{68}L_8$DMA precursor was mixed with HEMA solution containing Irgacure 819 (with a concentration of 10 wt% Irgacure 819 in HEMA) at a ratio of 9:1 (w/w).

3.2.3 Fabrication process of microneedles

The microneedle system consisted of inclined microneedle (IMN) parts on the two sides, vertical microneedle (VMN) parts in the center, and an elastic backing layer at the bottom. All microneedle parts were made of P_7L_2DMA, while the elastic backing layer was made of $P_{68}L_8$DMA through micro-molding. In brief, the photocrosslinkable P_7L_2DMA precursor was added into a polydimethylsiloxane (PDMS) mold and put into a vacuum chamber for 30 min to remove the bubbles between the mold and the solution. Then, excess P_7L_2DMA precursor was removed, and a 405-nm blue light was used to crosslink the material for over 2 min. Subsequently, the crosslinked part was gently de-molded. When demolding the IMNs, the demolding direction should align with the inclination direction of the needle tips; deviating from this method could cause structural damage due to interference between the molds and the microneedles. Finally, the microneedle parts were assembled onto the elastic backing layer by co-crosslinking with the $P_{68}L_8$DMA precursor.

In this chapter, one VMN and two IMNs with different inclinations (30° and 42°)

were used. The VMN had a needle height of 500 μm, a needle base diameter of 270 μm, a substrate thickness of 500 μm, and a substrate diameter of 14 mm. The IMNs had a needle length of 600 μm and a needle base diameter of 300 μm. The substrate had a thickness of 0.5mm and a diameter of 14 mm. In addition, the size of the elastic backing layer was 65 × 16 × 0.5 mm.

All the molds of the microneedle parts were manufactured by cast molding technique. Briefly, master molds of the microneedles with predesigned parameters were first fabricated based on copper alloy by machining. Then, the master molds were cast with a PDMS solution. The PDMS solution was prepared by mixing PDMS pre-polymer and curing agent (Sylgard 184, Dow Chemical Company, USA) in a ratio of 10:1. The mixture was degassed in a vacuum chamber for 30 min at room temperature and then cured at 80 ℃ for over 2 h. Finally, the master molds were separated from the cured PDMS, and the PDMS molds were obtained.

3.2.4 Microneedle morphology characterization

The general morphology of the microneedles was observed by an optical microscope (Nikon, Japan) and SEM (Tescan VEGA3, Czech Republic) after gold sputtering using a sputter coater.

3.2.5 Mechanical test

A mechanical testing system (ElectroForce 3200, Bose, America) was used to test the

tissue adhesion of the microneedles. Four groups (i.e., 0°, 30°, 42°, and 90°) were involved in this test, where 0° stood for the elastic backing layer without microneedles, 30° and 42° stood for elastic backing layer integrated with a piece of IMN inclining 30° or 42°, and 90° stood for elastic backing layer integrated with a piece of VMN.

To establish a fibrous tissue model for the test, chicken muscle tissues were used. To avoid the errors caused by tissue deformation, the chicken tissues were cut into flat pieces with 1.5-2 cm thicknesses and attached to glass slides using glue. Initially, the glass slide was clamped by the lower gripper of the mechanical testing system. In contrast, the backing layer was clamped by the upper gripper, with the microneedle side facing the chicken tissue. For the 0° group, the backing layers were directly attached to the chicken tissues with an adhesive area of 40 × 16 mm^2. For the 30°, 42°, and 90° groups, besides keeping the same adhesive area (40 × 16 mm^2) between the backing layers and the chicken tissues, the needle tips were inserted into the tissue in advance. Subsequently, the sensor probe was programmed to move up at 5 mm/min. All data were treated and analyzed by Origin software.

3.2.6 *In vitro* anti-scar assay

NIH3T3 fibroblasts, collagen I, and some auxiliary parts (e.g., sponges, supporting polytetrafluoroethylene plate, plastic pin) were used to create the fibroblast-loaded collagen system as an *in vitro* scar model. NIH3T3 fibroblasts were cultured in

DMEM containing 10% FBS and 1% PS. All cells were cultured in an incubator under humidified conditions at 37°C and 5% CO_2. The culture medium was replaced every two days.

The following procedure describes the fabrication of a single sample. Firstly, 3 mL collagen I working solution (2 mg/mL) was prepared by mixing 2 mL collagen I stock solution (3 mg/mL), 300 μL 10×PBS, 50 μL sterile 1M NaOH solution, and 650 μL sterile distilled water on ice. NIH3T3 fibroblasts were cultured to confluence under the abovementioned conditions and then dissociated using trypsin. A cell suspension containing 1.5×10^6 cells was centrifuged, after which the supernatant was discarded, and the cells were resuspended with 3 mL collagen I working solution, reaching a final cell concentration of 0.5×10^6 cells/cm^3. Subsequently, a mold made of polytetrafluoroethylene with a groove (35 × 15 × 5 mm) was used for casting. Two pieces of sponge (15 × 10 × 5 mm) were placed on the two sides of the groove in advance. Then, the cell-loaded collagen solution was cast in the mold with bubbles removed and incubated at 37°C in a humidified incubator for 60 min to form a firm gel. The cell-loaded collagen scaffold was cultured in Petri dishes on a supporting polytetrafluoroethylene plate (50 × 20 × 2 mm). Plastic pins were pushed through the sponges in the collagen to restrain the scaffold during the pre-culture period (24 h). Finally, the scaffold was subjected to 10% strain to simulate the tension force in real skin tissues. Different treatments (no treatment, VMN, IMN, VIMN) were then applied to the collagen scaffold for another 3 days.

To observe cell morphology and F-actin formation, fibroblasts in collagen scaffolds were fixed for 30 min with 4% paraformaldehyde, then permeabilized with 0.5% Triton X-100 for 10 min and blocked for 1 h at room temperature. Subsequently, samples were incubated in Alexa Fluor® 488-conjugated phalloidin solution (1:200 dilution) for 1 h and 4′,6-diamidino-2-phenylindole (DAPI) solution (1:1000 dilution) for another 10 min in the dark at room temperature. The samples were washed three times by PBS and examined by a confocal microscope (TCS SPE, Leica). To evaluate the expressions of some scar-related proteins, including α-SMA and CXCL 14. After the fixing, permeabilizing, and blocking of the fibroblasts in collagen scaffolds, following the previously mentioned steps, the samples were subsequently incubated with primary antibodies, including anti-α SMA (1:300, Abcam, ab124964), anti-CXCL 14 (1:300, Abcam, ab264467), at temperature of 4℃ for the whole night. Then the samples were incubated with secondary antibodies, Alexa Fluor® 488 (1:500, ab150157, Abcam), for 1 h and DAPI (1:1000 dilution) for another 10 min in the dark at room temperature. The samples were washed three times by PBS and examined by a confocal microscope (TCS SPE, Leica). The three-dimensional images were taken by the Z scanning function of the microscope and analyzed by the LAS X 3D visualization software.

3.2.7 Macrophage-loaded collagen system

RAW 264.7 macrophages, collagen I, and some auxiliary parts (e.g., sponges,

supporting polytetrafluoroethylene plate, plastic pin) were used to create the macrophage-loaded collagen system for investigating the effects of strain and different microneedle treatments on macrophages. RAW 264.7 macrophages were cultured in full DMEM. All cells were cultured at 37°C and 5% CO2 under humidified conditions. The culture medium was replaced every two days. The fabrication process of the macrophage-loaded collagen system was similar to that of the fibroblast-loaded collagen system.

To observe the cell morphology and F-actin formation, macrophages in collagen scaffolds were fixed for 30 min with 4% paraformaldehyde, then permeabilized with 0.5% Triton X-100 for 10 min and blocked for 1 h under room temperature. Subsequently, samples were incubated in Alexa Fluor® 488-conjugated phalloidin solution (1:200 dilution) for 60 min and DAPI solution (1:1000 dilution) for another 10 min in the dark at room temperature. The samples were washed three times by PBS and examined by a confocal microscope (TCS SPE, Leica). To evaluate the expressions of some inflammatory markers, including iNOS (M1 macrophage marker), mannose (M2 macrophage marker), IL-10 (anti-inflammatory factor), and TNF-α (inflammatory factor). After the fixing, permeabilizing, and blocking of the macrophages in collagen scaffolds, following the previously mentioned steps, the samples were subsequently incubated with primary antibodies, including anti-iNOS (1:500, Abcam, ab3523), anti-mannose (1:1000, Abcam, ab64693), anti-TNF-α (1:500, Abcam, ab183218), and anti-IL-10 (1:500, Abcam, ab189392), overnight at 4°C,

followed by incubation with secondary antibodies, Alexa Fluor® 488 (1:500, ab150157, Abcam) for 1 h, and DAPI (1:1000 dilution) for another 10 min in the dark at room temperature. The samples were washed three times by PBS and examined by a confocal microscope (TCS SPE, Leica).

3.2.8 RNA sequencing

After a 3-day culture of the fibroblast-loaded collagen system (0.5×10^6 cells/cm^3), the middle parts of the collagen scaffolds (without the sponges) in different groups (i.e., control, VMN, IMN, VIMN) were enzymatically digested in 50-mL centrifuge tubes by collagenase Type I (Thermo Fisher, 17100-017) for 1 h at 37℃ to harvest the fibroblasts. According to the user manual, the collagenase Type I solution was prepared using HBSS to a final concentration of 5 mg/mL. After the collagen was fully digested without any obvious bulks in the tubes, these samples were subjected to centrifugation at a speed of 1,000 rpm for 5 minutes, and the resulting supernatant was cautiously removed. Then, the total RNA of the fibroblasts was extracted using 100 μL – 1,000 μL TRIzol reagent until the liquid became non-sticky and used for standard RNA sequencing. According to the manufacturer's instructions, RNA sequencing was conducted on an illumina Novaseq 6000 platform (LC-Bio Technology CO., Ltd., China). For samples with biological replicates, DESeq2 was employed for analysis. For samples without biological replicates (inter-sample comparisons), edgeR was used for analysis. In the case of multi-group comparisons, edgeR was employed for analysis. Differentially expressed genes were selected based

on a fold change >2 or < 0.5. The GO analysis and KEGG enrichment were performed using the OmicStudio tools (https://www.omicstudio.cn/tool).

3.2.9 Statistical analysis

GraphPad software was used for statistical analysis. Unless otherwise stated, all tests were repeated at least three times. Results are shown in mean ± standard deviation (SD). A normality test was conducted for each set of data. One-way ANOVA was used in comparing two different groups. P-value ≤ 0.05 was considered statistically significant (*p ≤ 0.05, **p ≤ 0.01, ***p ≤ 0.001).

3.3 Results and discussions

3.3.1 Fabrication and characterization of the contractile microneedle patch

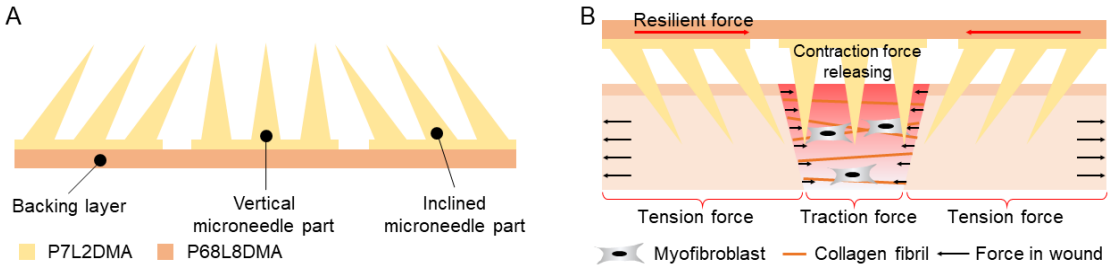

Figure 3-1. Structural design and working principle of the contractile microneedle patch. (A) Illustration of the contractile microneedle patch, consisting of three parts (i.e., backing layer, middle part, inclined part) and made of two materials (i.e., P_7L_2DMA, $P_{68}L_8DMA$). (B) Illustration showing the working principle of the contractile microneedle patch. Two kinds of force exist in wounds: tension force generated by surrounding tissues, and traction force generated by fibroblasts in the wound site. In the contractile microneedle patch, the middle part was designed for

contraction force relief, inclined parts for tissue adhesion, and the elastic backing layer for contractile force generation.

The contractile microneedle patch consisted of an elastic backing layer made of $P_{68}L_8$DMA, an IMN part on the two sides made of P_7L_2DMA, and a VMN part in the center made of P_7L_2DMA (**Figure 3-1**A). When the patch was applied, the elastic backing layer was pre-stretched to generate a contractile force. Subsequently, the IMNs, being sufficiently rigid, penetrate the surrounding area of the wound. On one hand, they could transmit the contractile force to the periphery of the wound to counteract the tension force exerted by the surrounding tissues. On the other hand, they could adhere onto tissue through mechanical self-locking. Meanwhile, the VMNs directly inserted into the wound site to relieve the traction forces generated by fibroblasts in wound tissue (**Figure 3-1**B). By minimizing the stress within the wound, the proposed patch in this chapter could reduce scar formation.

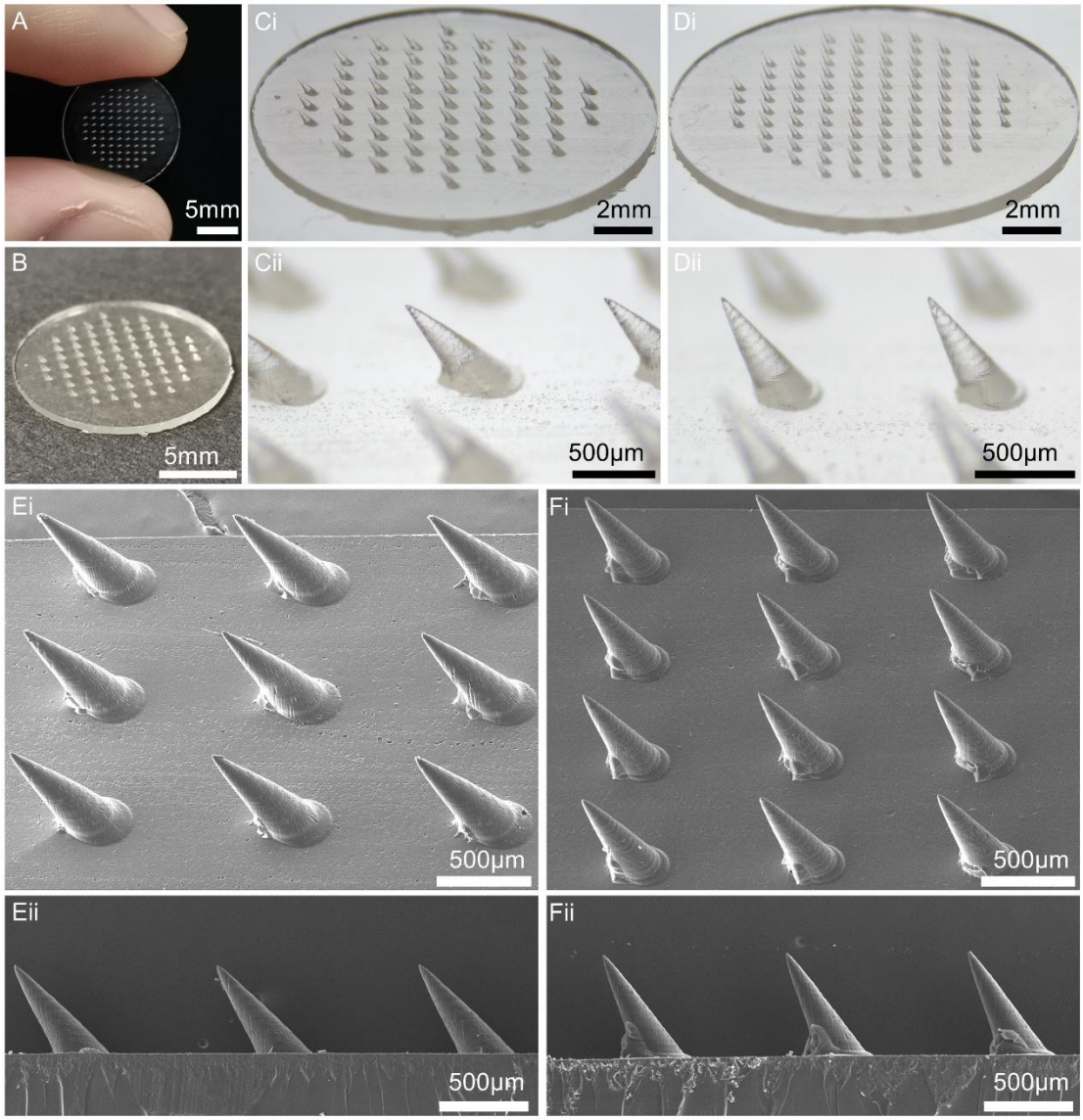

Figure 3-2. Morphology characterization of the IMNs. (A) & (B) General appearance of a single IMN patch. (C) Microscopic images of IMNs with an inclined angle of 30°. (D) Microscopic images of IMNs with an inclined angle of 42°. (E) SEM images of IMNs with an inclined angle of 30°. (F) SEM images of IMNs with an inclined angle of 42°.

The detailed fabrication process has been discussed in section 3.2.3. Briefly, different parts, including the backing layer, VMN part, IMN part, were fabricated by

micromolding individually. Then the microneedle parts were attached to the backing layer by co-crosslinking using P_7L_2DMA precursor. **Figure 3-2**A-B show the general appearance and dimensions of the IMNs. Two IMNs with different inclinations of 30° (**Figure 3-2**C) and 42° (**Figure 3-2**D) were used in this chapter. The microstructures of these two were demonstrated using SEM in **Figure 3-2**E-F.

3.3.2 Tissue adhesion of the contractile microneedle patch

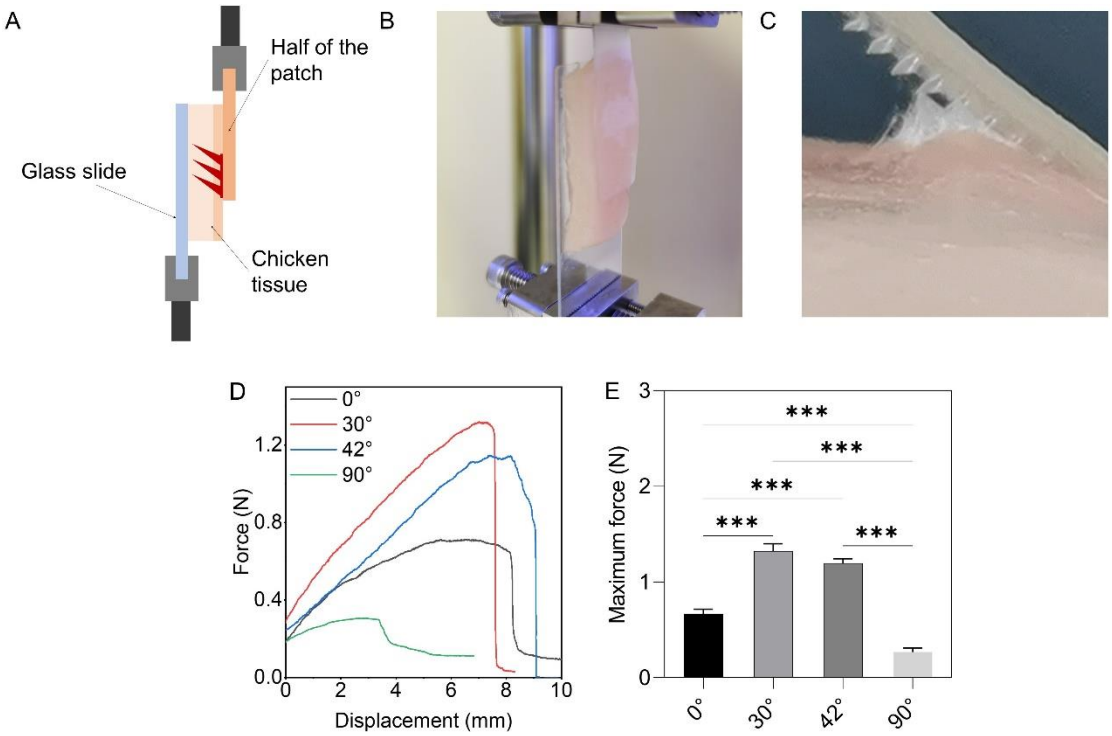

Figure 3-3. Tissue adhesion test. (A) Schematic of the tissue adhesion test setup. (B) Photographic image of the tissue adhesion test setup. (C) Interlocking between the IMN tip and the chicken tissue. (D) Force-displacement curve during the tissue adhesion test of microneedles with different inclined angles (i.e., 0°, 30°, 45°, 90°). (E) Quantitative analysis of the adhesive force of microneedles with different inclined angles (i.e., 0°, 30°, 45°, 90°). The differences are statistically significant when p

values are below 0.001 (***).

To assess the adhesive force of IMNs to biological tissues under the condition of the backing layer generating a contractile force, a tissue adhesion experiment was conducted. **Figure 3-3**A illustrates the experimental setup, while **Figure 3-3**B shows an actual photo of the setup. For convenient tensile measurement and to simulate practical usage, the samples consisted of a single piece of IMNs and a half piece of backing layer. At the beginning of the experiment, the IMNs were pre-inserted into chicken tissue, while the tensile tester clamped onto the backing layer and pulled it upwards until the microneedles detached from the tissue. **Figure 3-3**C demonstrates that when the IMNs were separated from the chicken tissue, the needle tips could lift the chicken fibers. This indicates that the IMNs not only penetrated the tissue but also interlock with it, achieving the desired adhesion effect.

To compare the tissue adhesion forces between different microneedles and the backing layer alone, four sets of samples were used in this experiment, including 0°, 30°, 42°, and 90° (0° stood for pure backing layer, while 90° stood for VMNs). **Figure 3-3**D is the force-displacement curve of different groups and **Figure 3-3**E shows the quantitative results. Pure backing layer (0°) exhibited a certain degree of tissue adhesion (0.67 ± 0.04 N/patch). Meanwhile, the VMN possessed the lowest adhesion force (0.27 ± 0.03 N/patch), as it inherently tended to pop out due to the tissue's elasticity, thereby compromising the adhesion force provided by the backing

layer. Both sets of IMN (1.32 ± 0.06 N/patch in 30° group; 1.2 ± 0.04 N/patch in 42° group) demonstrated significantly higher adhesion forces than pure backing layer, indicating that the IMN-tissue interlocking enhanced adhesion. Furthermore, the inclined angle did not have a significant impact on the adhesion force, possibly because the number of needle tips was insufficient to generate mechanical differences.

3.3.3 *In vitro* anti-scar effect of the contractile microneedle patch

To preliminarily validate the anti-scar effect of the patch, we first needed to establish an *in vitro* scar model. The main cause of scar formation during skin wound healing is the excessive deposition of collagen matrix by fibroblasts. Several studies have also reported skin scar models based on 3D culture of fibroblasts in collagen, which showed great effectiveness on exploring scar formation mechanism.[25, 168, 173, 174] Therefore, in this chapter, we adopted a similar approach to construct the *in vitro* scar model.

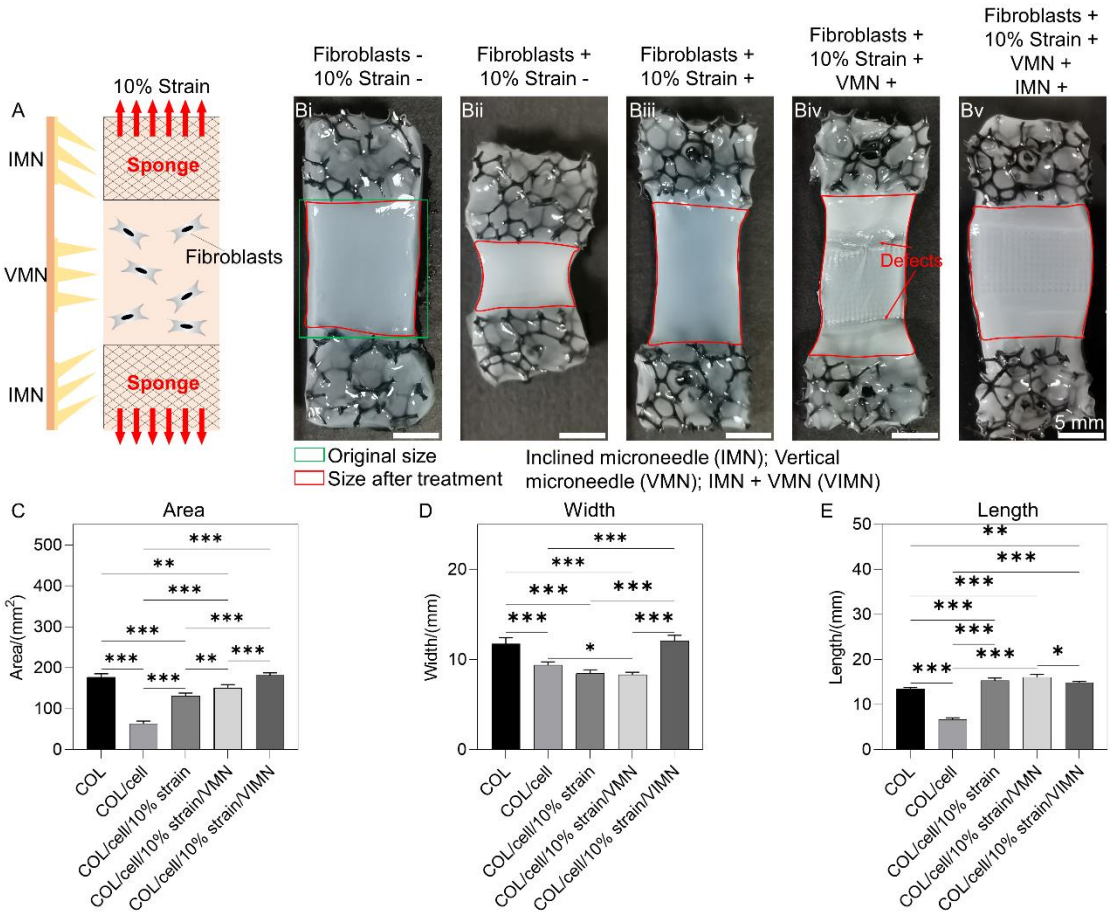

Figure 3-4. Contractile microneedle patch and fibroblasts induced mechanical impacts on collagen matrix deformation. (A) Illustration showing the experimental setup of the *in vitro* scar model. (B) Images of the *in vitro* scar models applied with different treatments for 3 days. (C)-(E) Quantitative analyses of size parameters, including area, width, and length, among the five groups after 3 days of treatments. The differences are statistically significant when p values are below 0.05 (*), 0.01 (**), and 0.001 (***).

As shown in **Figure 3-4**A, the scar model consisted of a rectangular collagen matrix. Fibroblasts were seeded in the central region (0.5×10^6 cells/cm^3), while two pieces of sponge were combined at the two ends to apply tension and strain. The specific

construction process can be found in section 3.2.6. After the preliminary construction of the scar model, it was necessary to fix the two ends and pre-culture it in culture medium for 24 h before conducting formal experiments with different treatments.

Firstly, as shown in **Figure 3-4**B, we investigated the effects of fibroblasts and different treatment conditions on the dimensions and shape of the collagen matrix. Central regions marked by red line in five groups, including (Bi) pure collagen without fibroblasts and strain (COL), (Bii) collagen with fibroblasts but without strain (COL/cell), (Biii) collagen with fibroblasts and 10% strain (COL/cell/10% strain), (Biv) collagen with fibroblasts and 10% strain applied with VMN (COL/cell/10% strain/VMN), and (Bv) collagen with fibroblasts and 10% strain applied with VIMN (COL/cell/10% strain/VIMN), were compared. The area (**Figure 3-4**C), width (**Figure 3-4**D), and length (**Figure 3-4**E) of each group were quantitatively analyzed. From the results, COL showed minimal changes in both area and shape, closely resembling the original dimensions. This suggests that pure collagen exhibits limited swelling deformation in the culture medium. In contrast, COL/cell exhibited significant reductions in all parameters, indicating intense contraction after 3 days of cultivation. Quantitatively, fibroblasts in COL/cell generated substantial contractile forces, resulting in a 64.1% reduction in area, a 20% reduction in width, and a 50.17% reduction in length compared with COL. This result was consistent with the phenomenon of wound contracture caused by scar formation. For COL/cell/10% strain, the 10% strain resulted in a 13.68% increase in length compared with COL.

However, the area decreased by 25.88% and the width decreased by 27.89%, indicating that fibroblasts exerted contractile forces in the width direction, leading to the contraction of the collagen matrix. In COL/cell/10% strain/VMN, the vertical microneedles resulted in a slight increase (15.57%) in overall area compared with COL/cell/10% strain. However, there were no significant differences in length and width, suggesting that vertical microneedles had some effect in preventing collagen contraction. However, due to the 10% strain, the overall deformation trend remained unchanged, and noticeable defects and stress concentration occurred at the boundaries of the microneedle application area. For COL/cell/10% strain/VIMN, the further application of inclined microneedles to counteract the strain at both ends significantly reduced collagen contraction. Apart from a slight increase in length (10.3%), there were no significant changes in area or width compared with COL. This indicates that the combined use of inclined and vertical microneedles released the contraction stress caused by fibroblasts and prevented stress concentration at the boundaries of the microneedle application area.

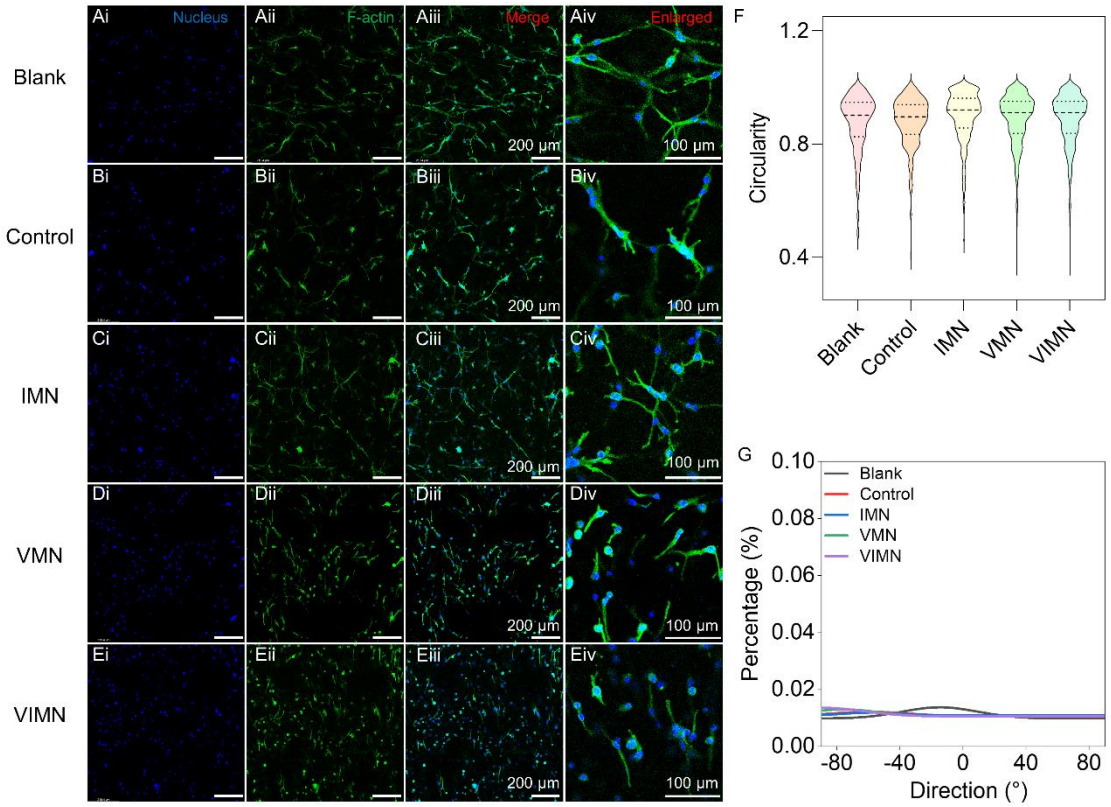

Figure 3-5. Morphology of NIH 3T3 fibroblasts among different groups on Day 1. (A)-(E) Representative immunofluorescence images of NIH 3T3 fibroblasts stained for F-actin in blank, control, inclined microneedle (IMN), vertical microneedle (VMN), IMN+VMN (VIMN) groups. Green, F-actin; blue, nucleus. (F) Quantitative analysis of nuclear circularity among different groups. (G) Quantitative analysis of cell angle distribution among different groups.

To further investigate the impact of contractile patch on fibroblast function in the scar model, immunofluorescence techniques were employed to quantify cell morphology and the expression of relevant functional proteins in different groups, including Blank (without strain), Control (10% strain to simulate natural wound condition), IMN (10% strain + inclined microneedles), VMN (10% strain + vertical microneedles), and

VIMN (10% strain + vertical microneedles + inclined microneedles). **Figure 3-5**A-E illustrate NIH 3T3 fibroblast morphology in the scar model stained for F-actin after 1 day of pre-culture. Based on the quantity and distribution of cells, fibroblasts appear to be in the early stages of spreading, with no formation of interconnected networks between cells. **Figure 3-5**F&G indicate no significant differences in terms of nuclear deformation or directional cell growth, ensuring consistency in cellular condition between groups on day 1.

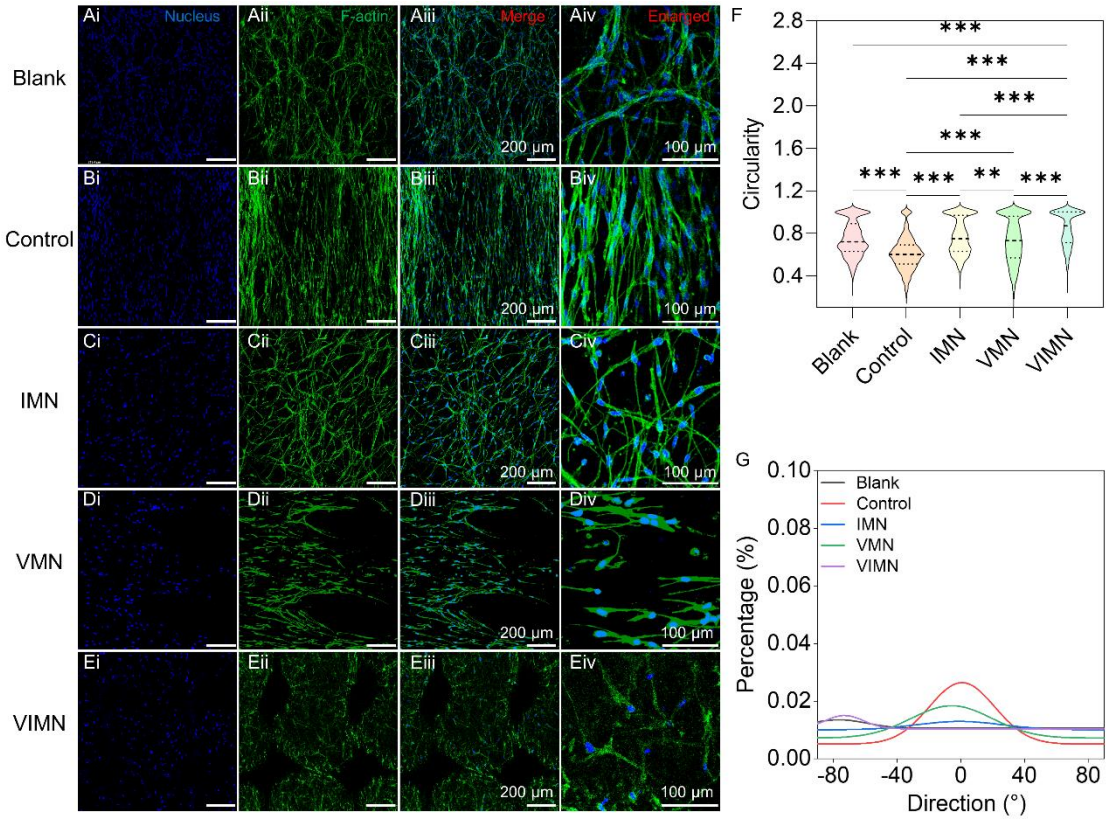

Figure 3-6. Morphology of NIH 3T3 fibroblasts among different groups on Day 4. (A)-(E) Representative immunofluorescence images of NIH 3T3 fibroblasts stained for F-actin in blank, control, inclined microneedle (IMN), vertical microneedle (VMN), IMN+VMN (VIMN). Green, F-actin; blue, nucleus. (F) Quantitative analysis

of nuclear circularity among different groups. (G) Quantitative analysis of cell angle distribution among different groups. The differences are statistically significant when p values are below 0.01 (**), and 0.001 (***).

Figure 3-6A-E illustrates the cellular morphology of fibroblasts in different groups after 4 days of culture in the scar model. Specifically, to observe the impact of stress concentration in the border of treated area on cell growth in VMN, the edge region was selected for analysis. The quantity and density of cells significantly increased in all groups. **Figure 3-6**F&G present the statistical analysis of nuclear circularity and cell orientation on Day 4. The control had the lowest cell roundness value, indicating significant deformation of the cell nuclei under strain, and elongation of the cell cytoskeleton. Additionally, the cell orientation in the control group was significantly higher than that in other groups. The blank group and IMN group exhibited similar nuclear circularity and cell orientation, demonstrating that IMN counteracted the externally applied strain. The VMN group had slightly lower nuclear circularity compared with the IMN group, and significantly higher cell orientation compared with the Blank and IMN groups, indicating that stress concentration at the edge region also had a significant impact on cell growth and deformation. The stress concentration could be reflected by the noticeable deformation of the holes created by needle tips in **Figure 3-6**D. In contrast, the VIMN group had significantly higher nuclear circularity than all other groups, indicating minimal cell deformation. The cell orientation in the VIMN group did not significantly differ from the that in the control and IMN groups,

and the holes created by needle tips did not show noticeable deformation (**Figure 3-6**E). Overall, these findings demonstrated that VIMN could minimize stress in the scar model, reducing its impact on fibroblast growth.

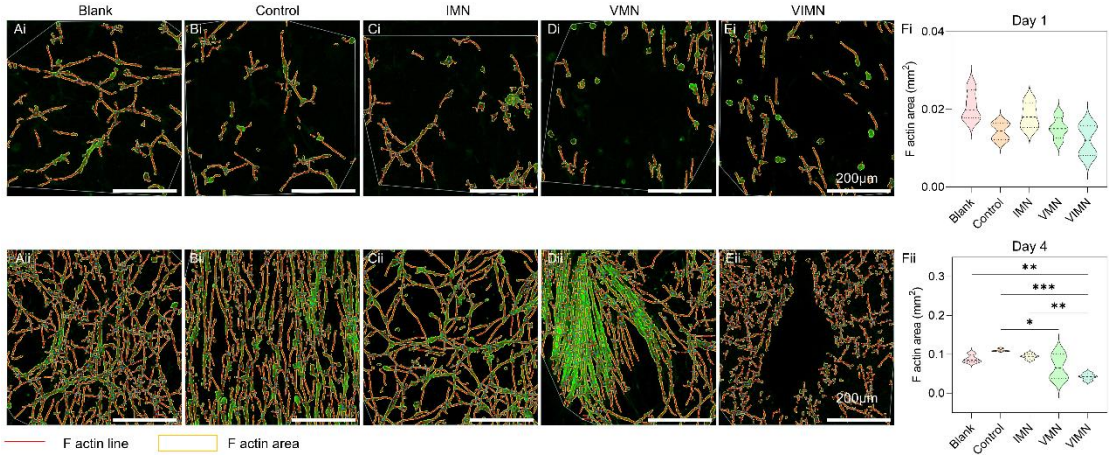

Figure 3-7. Quantitative analysis of F-actin of NIH 3T3 fibroblasts on Days 1 and 4. (A)-(E) Representative immunofluorescence images of F-actin in NIH 3T3 fibroblasts, with lines and areas drawn using AngioTool. (F) Quantitative analysis of F-actin area among different groups on (i) Day 1, and (ii) Day 4. The differences are statistically significant when p values are below 0.05 (*), 0.01 (**), and 0.001 (***).

In addition to nuclear circularity and cell orientation, F-actin area of fibroblasts cultured for 1 and 4 days in the scar model was also quantified (**Figure 3-7**). As shown in **Figure 3-7**A-E, the trajectories of F-actin were marked with red lines, and their areas were outlined with yellow frames. On Day 1, due to the limited culture time, there was little difference in F-actin area among all groups (around 0.02 mm^2). On Day 4, the cell areas in all groups significantly increased. The control group exhibited the highest F-actin area (0.110 ± 0.003 mm^2) due to the pure strain applied,

indicating that a high-stress environment promoted F-actin expression and cytoskeletal remodeling in fibroblasts. The blank (0.089 ± 0.009 mm^2) and IMN (0.095 ± 0.006 mm^2) groups had slightly but insignificantly lower values than the control group. The VMN group (0.068 ± 0.029 mm^2) had significantly lower values than the control group, but F-actin still showed high expression in high-stress areas. In contrast, the F-actin area in VIMN group (0.004 ± 0.007 mm^2) was the smallest among all groups, indicating that VIMN reduced F-actin expression in fibroblasts by minimizing stress in the scar model. In summary, the stress in the scar model promoted F-actin expression and intercellular connections between fibroblasts, which further increased the stress in collagen matrix and sensitivity of cells to mechanical stimulation. Then fibroblasts generated traction forces and caused matrix contraction, leading to a vicious cycle. In contrast, VIMN significantly reduced various stresses in the model, preventing further interconnection of fibroblasts and limiting their ability to generate contraction forces in later stages.

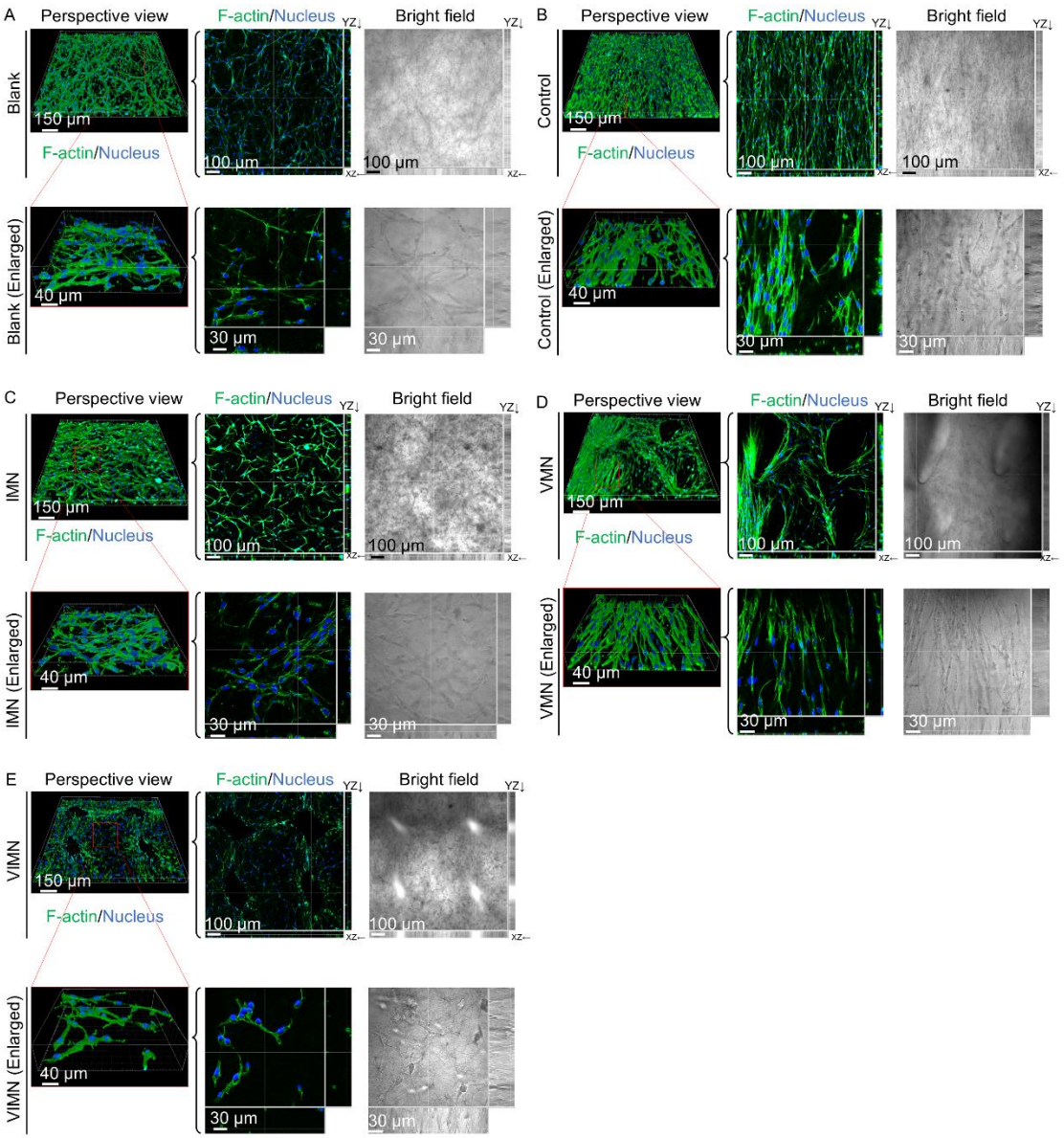

Figure 3-8. 3D cell morphology of NIH 3T3 fibroblasts stained with F-actin in the *in vitro* scar model on Day 4 in (A) blank, (B) control, (C) IMN, (D) VMN, (E) VIMN. Green, F-actin; blue, nucleus.

Figure 3-8 further illustrates the 3D cell morphology and bright-field images of fibroblasts cultured for 4 days in different groups, aiming to better observe the influence of matrix stress on cell morphology and distribution (a supplement to **Figure 3-6**). In the blank and IMN groups, cells exhibited a uniform and random

distribution. In the control group, cells showed a highly oriented growth pattern. Specifically, **Figure 3-8**D provides a more three-dimensional view of the VMN group, where stress concentration at the edges led to severe distortion of microneedle holes and elongation of cells with directional growth around the microneedle holes. In contrast, in the VIMN group (**Figure 3-8**E), microneedle holes did not undergo distortion, and cells exhibited a random and uniform distribution around the holes, with fewer interconnections between cells.

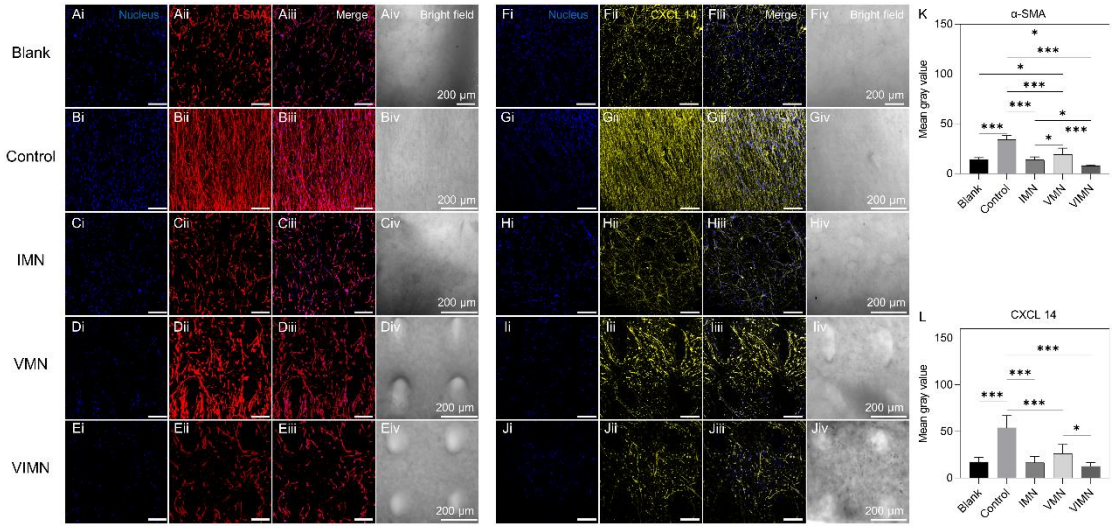

Figure 3-9. α-SMA and CXCL 14 expressions of NIH 3T3 fibroblasts in the *in vitro* scar model on Day 4. (A)-(E) Representative immunofluorescence images and bright field images of NIH 3T3 fibroblasts stained for α-SMA among different groups. Blue, nucleus; red, α-SMA; (F)-(J) Representative immunofluorescence images and bright field images of NIH 3T3 fibroblasts stained for CXCL 14 among different groups. Blue, nucleus; yellow, CXCL 14; (K)-(L) Quantitative analysis of relative fluorescence intensity in different groups for evaluating the expressions of α-SMA and CXCL 14. The differences are statistically significant when p values are below

0.05 (*), and 0.001 (***).

Finally, we evaluated the expressions of scar-related proteins (i.e., α-SMA and CXCL 14) in different groups using immunofluorescence. α-SMA is a marker for myofibroblasts, which are the main contributors to scar formation. CXCL 14 is a chemokine that recruits fibroblasts.[168] From the **Figure 3-9**A-J, it can be observed that the fluorescence intensity of both scar-related proteins in the Control group is significantly higher than in other groups, followed by the VMN group. The remaining three groups show similar fluorescence intensities for both proteins. **Figure 3-9**K shows that the control group had the highest expression level of α-SMA, significantly higher than all other groups. The VMN group had the second-highest expression, at 56.47% of the control group. The blank and IMN groups had similar expression levels, at 40.92% and 40.77% of the control group, respectively. The VIMN group had significantly lower expression levels than all other groups, at only 22.8% of the control group. The expression of CXCL 14 followed a similar trend: The control group had the highest expression level, followed closely by VMN. The expression levels in the blank, IMN, and VIMN groups were similar, much lower than that in the control group.

In summary, the expressions of these scar-related proteins were highly correlated with the magnitude of stress. The high-stress condition in the control group promoted fibroblast differentiation into myofibroblasts and increased expression of CXCL 14.

In blank and IMN groups, although there was no external strain, the formation of fibroblast networks and the resulting traction forces increased local stress, leading to higher expression of scar proteins. In the VMN group, although traction forces from fibroblasts in the central region were avoided, external strain still led to stress concentration in the edge region. Only the VIMN group could simultaneously avoid stress concentration and the traction forces generated by fibroblasts in later stages.

3.3.4 *In vitro* effect of the contractile microneedle patch on inflammatory response

Inflammatory cells play a crucial role in wound healing and scar formation, and excessive inflammatory response can release too many pro-inflammatory cytokines (e.g., TNF-α) by inflammatory cells like macrophages.[5] These pro-inflammatory factors activate fibroblasts to overproduce collagen and related components, leading to the formation of scar tissue. Excessive external mechanical stimuli can induce macrophage transition to a pro-inflammatory phenotype.[175, 176]

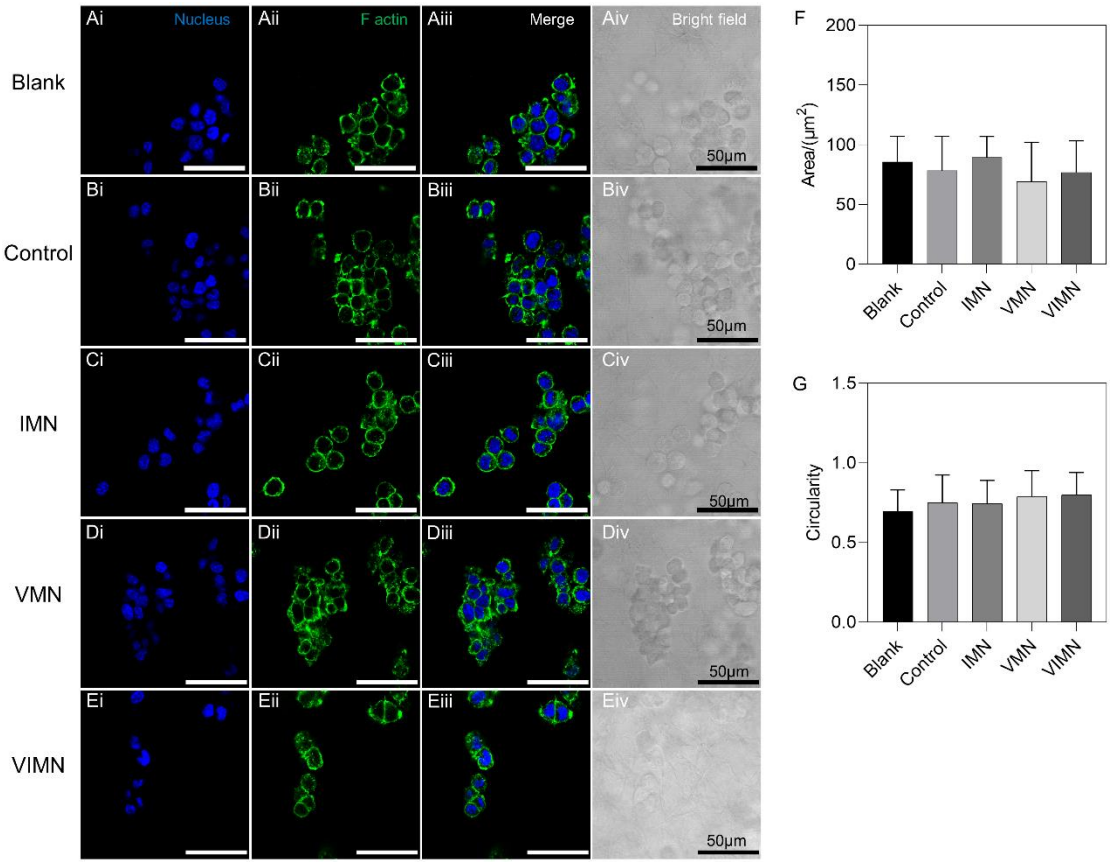

Figure 3-10. Morphology of RAW 264.7 macrophages in the *in vitro* scar model among different groups on Day 4. (A)-(E) Representative immunofluorescence images and bright field images of RAW 264.7 macrophages stained with F-actin. Green, F-actin; blue, nucleus. (F) Quantitative analysis of the cell area among different groups. (G) Quantitative analysis of the nuclear circularity among different groups.

In this section, we investigated the inflammatory response of macrophages in different groups of scar models to validate the effect of the contractile patch. **Figure 3-10**A-E shows the morphology of RAW 264.7 macrophages stained for F-actin in different groups. From the quantitative results (**Figure 3-10**F&G), there were no significant differences in cell area or nuclear circularity among the groups. Even in the control

group under high-stress conditions, there were no noticeable changes in cell morphology. This may be because these cells were encapsulated in a collagen matrix, which required more time or greater mechanical stimulation to induce morphological changes.

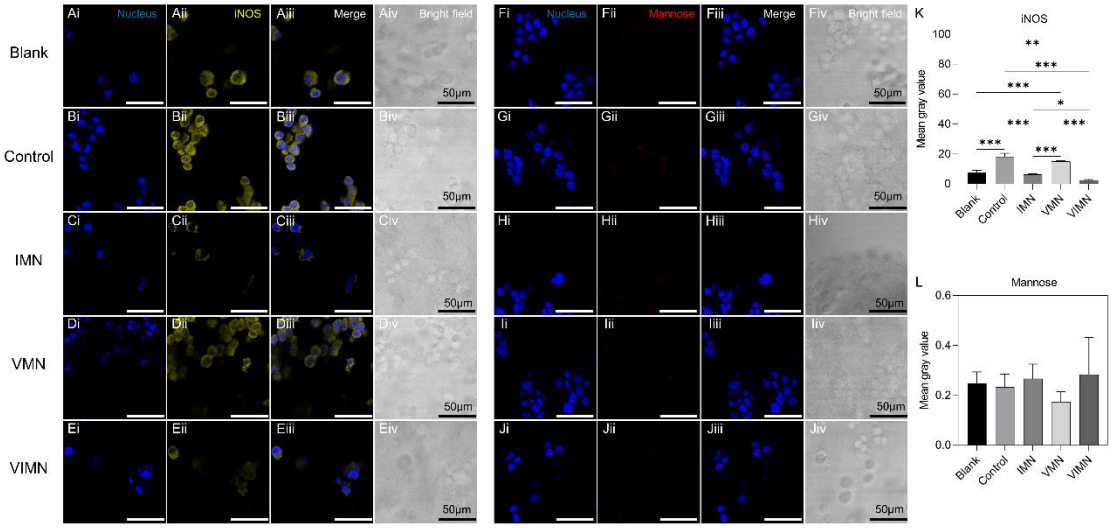

Figure 3-11. iNOS and Mannose expressions of RAW 264.7 macrophages in the *in vitro* scar model on Day 4. (A)-(E) Representative immunofluorescence images and bright field images of RAW 264.7 macrophages stained for iNOS among different groups. Blue, nucleus; yellow, iNOS; (F)-(J) Representative immunofluorescence images and bright field images of RAW 264.7 macrophages stained for Mannose among different groups. Blue, nucleus; red, Mannose; (K)-(L) Quantitative analysis of relative quantity of fluorescence intensity in different groups for evaluating the expression of iNOS and Mannose. The differences are statistically significant when p values are below 0.05 (*), 0.01 (**), and 0.001 (***).

To further characterize the functional transition of macrophages, we evaluated the

expressions of iNOS and Mannose proteins in different groups (**Figure 3-11**). iNOS is a pro-inflammatory marker, while Mannose is an anti-inflammatory marker in macrophages. **Figure 3-11**A-E display the iNOS expression (marked in yellow) in different groups. From preliminary image observation, the iNOS fluorescence intensity is relatively low in the VIMN and IMN groups, while the Control group exhibits significantly higher fluorescence intensity compared to other groups. **Figure 3-11**F-J display the Mannose expression (marked in red) in different groups. The expression of Mannose among all the groups is not evident. From the quantitative analysis in **Figure 3-11**K, the control group had the highest iNOS expression, followed by the VMN group with an expression level approximately 82.78% of the control group. The iNOS expression of blank and IMN groups were similar, at 40.9% and 34.17% of the control group level, respectively. VIMN group had obviously lower expression of iNOS than the other groups, at only 13.2% of the control group. Regarding Mannose, there were no notable distinctions in expression levels among all groups (**Figure 3-11**F-J&L). In summary, the high-stress environment in the control and VMN groups promoted the pro-inflammatory phenotype of the macrophages. On the other hand, the VIMN group, by eliminating tissue stress, avoided this phenotypic transition.

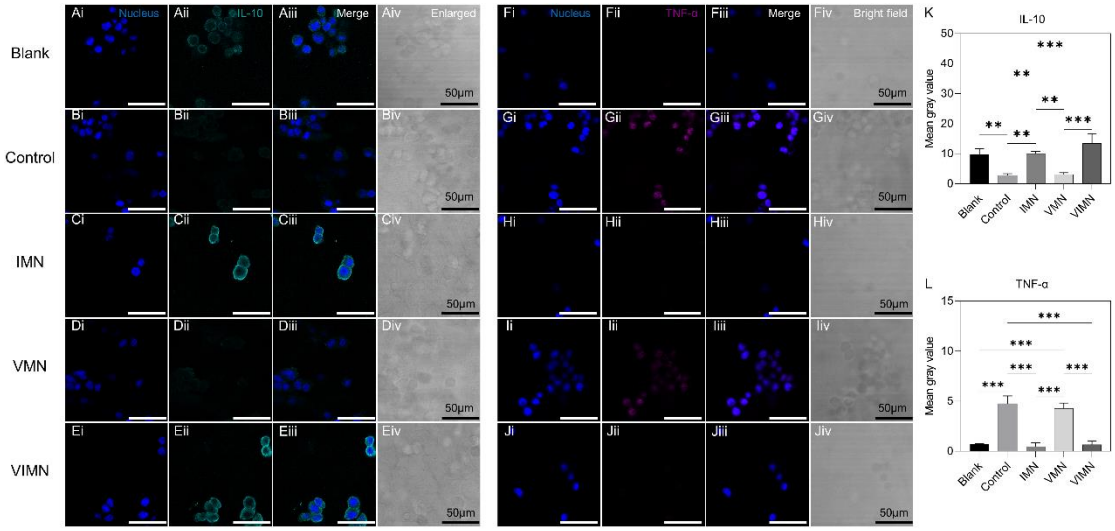

Figure 3-12. IL-10 and TNF-α expressions of RAW 264.7 macrophages in the *in vitro* scar model on Day 4. (A)-(E) Representative immunofluorescence images and bright field images of RAW 264.7 macrophages stained for IL-10 among different groups. Blue, nucleus; cyan, IL-10; (F)-(J) Representative immunofluorescence images and bright field images of RAW 264.7 macrophages stained for TNF-α among different groups. Blue, nucleus; magenta, TNF-α; (K)-(L) Quantitative analysis of relative fluorescence intensity in different groups for evaluating the expressions of IL-10 and TNF-α. The differences are statistically significant when p values are below 0.01 (**), and 0.001 (***).

In addition, we characterized the expressions of TNF-α and IL-10 proteins in different groups. TNF-α is a typical pro-inflammatory cytokine, while IL-10 is a typical anti-inflammatory cytokine. **Figure 3-12**A-E display the IL-10 expression (marked in cyan) in different groups. From preliminary image observation, the IL-10 fluorescence intensity is relatively high in the VIMN and IMN groups, while the Control group and VMN group show no significant IL-10 expression. **Figure 3-12**F-J

display the TNF-α expression (marked in magenta) in different groups. The control group shows an obvious signal of TNF-α expression. The VMN group also shows a weak signal. The remaining groups all show no significant TNF-α expression. Quantitative results (**Figure 3-12**K) showed that IL-10 expression in the VIMN group was the highest, significantly higher than the control group (approximately 476% of the control group's expression level). The expression levels in the blank and IMN groups were similar, at 348% and 356% of the control group's value, respectively; although slightly lower than the VIMN group, there were no significant differences. The expression level of IL-10 in the VMN group was similar to the control group. On the other hand, the expression of TNF-α showed the opposite trend. The expression levels in the control and VMN groups were similar and significantly higher than in the other groups. The expression levels in the blank, control, and VIMN groups were relatively low, at 14.2%, 10.1%, and 13.62% of the control group's value, respectively, with no significant differences among the three.

In summary, for the model with macrophages, traction force generated by fibroblasts was absent, indicating that there was no other stress in the collagen matrix except the one generated by external strain. The introduction of IMN could counteract external strain and reduce the generation of stress concentration, thereby reducing the pro-inflammatory phenotype transition and pro-inflammatory factor expressions in the macrophages. Based on previous studies,[175, 176] the potential mechanism of this phenomenon may involve mechanical stimuli activating the Piezo 1 ion channels in

macrophages, thereby further influencing macrophage polarization and stiffness sensing. In the future, we will investigate the signaling pathways of this mechanism.

3.3.5 Bioinformatic analysis of fibroblasts in the scar model

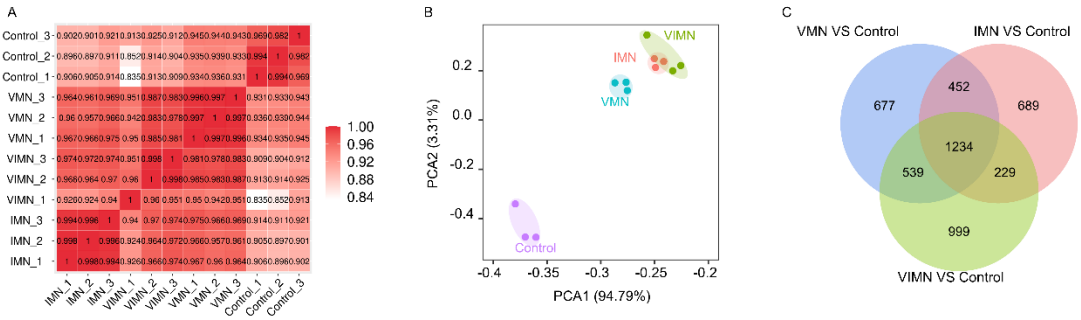

Figure 3-13. (A) Pearson correlation evaluation between different samples. (B) Principal component analysis (PCA) plot showing the obvious separation of gene expressions in different groups. (C) Venn diagram of differentially expressed genes between treatment groups (VMN, IMN, and VIMN) and control group.

To further elucidate the anti-scar mechanisms in the *in vitro* model, we performed bioinformatics analysis on the differentially expressed genes between the treatment groups (IMN, VMN, VIMN) and the control group. Pearson correlation evaluation (**Figure 3-13**A) demonstrated that the correlation coefficients among samples within each group were greater than 0.95, indicating good sample stability and consistency within each group. In a PCA plot (**Figure 3-13**B), the control group was noticeably separated from the other three groups, indicating significant differences between the control and the rest. The Venn diagram (**Figure 3-13**C) showed that VMN, IMN, and VIMN had numerous differentially expressed genes (2902 genes for VMN versus

control, 2604 genes for IMN versus control, and 3001 genes for VIMN versus control), with 1234 genes intersecting among them.

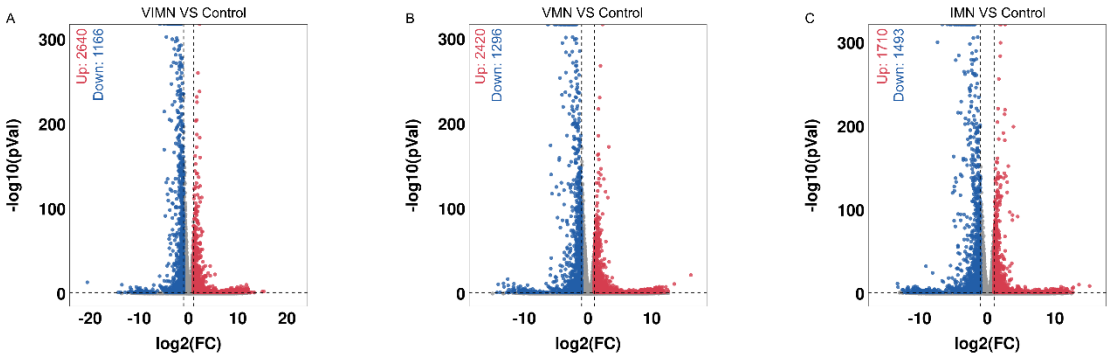

Figure 3-14. Volcano plots of transcriptomic analysis of differentially expressed genes in (A) VIMN versus control, (B) VMN versus control, (C) IMN versus control.

The Volcano plots (**Figure 3-14**) further exhibited 2640 up-regulated and 1166 down-regulated genes (VIMN versus control), 2420 up-regulated and 1296 down-regulated genes (VMN versus control), 1710 up-regulated and 1493 down-regulated genes (IMN versus control) according to the empirical Bayes method (fold change ≥ 2; $p < 0.05$). Based on these results, we selected the VIMN group with the most differentially expressed genes for further evaluation.

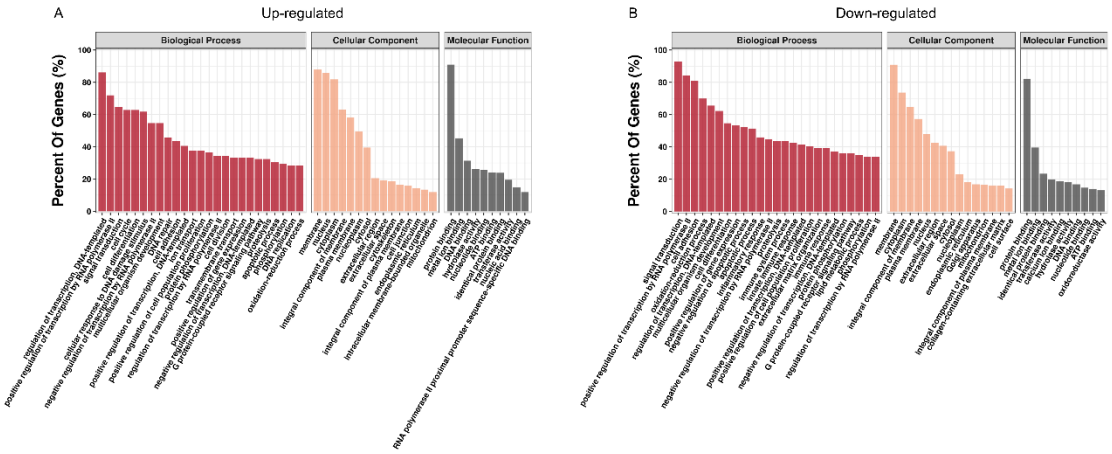

Figure 3-15. Gene Ontology (GO) classification of (A) up-regulated and (B) down-regulated genes in NIH 3T3 fibroblasts (VIMN versus control).

We performed GO analysis on the differentially expressed genes between the VIMN and control groups, focusing on biological process, molecular function, and cellular component. From the significantly enriched GO terms (**Figure 3-15**), we identified several down-regulated terms (over 80% of genes enriched), including signal transduction, cell adhesion, protein binding, membrane, and cytoplasm. These terms are all related to the interaction between cells and the extracellular matrix.

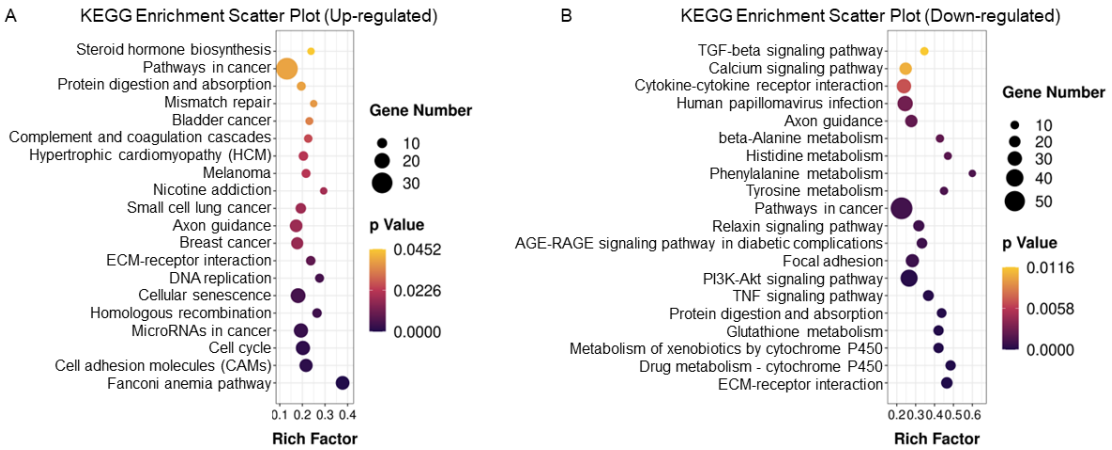

Figure 3-16. (A) Up-regulated, and (B) down-regulated KEGG enrichment scatter

plot of VIMN versus Control.

Based on the preliminary GO analysis, we then performed the Kyoto Encyclopedia of Genes and Genomes (KEGG) pathway analysis (**Figure 3-16**), revealing significant downregulation of ECM-receptor interaction, PI3K-Akt, and focal adhesion pathways between VIMN and control groups. Hence, we concluded that the mechanotransduction and ECM deposition were inhibited by VIMN treatment.

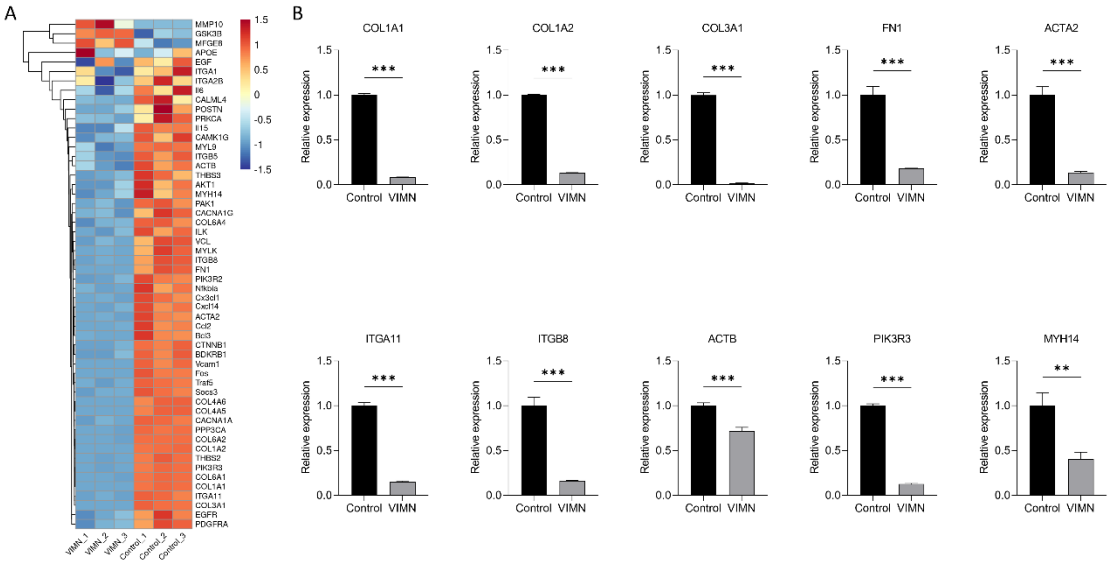

Figure 3-17. (A) Heatmap evaluation and quantitative statistics of differentially expressed genes involved in ECM–receptor interaction, TNF signaling pathway, PI3K-Akt signaling pathway, focal adhesion, and calcium signaling pathway. (B) Downregulated genes related to mechanical transduction and scar formation.

In addition, from the heatmap analysis (**Figure 3-17**), multiple genes related to mechanical transduction (ITGA, ITGB, ACTB, VCL, PI3KR2, PI3KR3, MYH14) and

scar formation (COL1A1, COL1A2, COL3A1, FN1, ACTA2, EGFR) were down-regulated after VIMN treatment. In summary, VIMN treatment inhibited ECM-receptor interaction, subsequently suppressing the PI3K-Akt pathway and focal adhesion pathway, ultimately affecting actin polymerization, filopodia lamellipodia formation, and other cellular cytoskeletal remodeling activities. Consequently, scar formation caused by external stress and mechanical transduction was reduced.

3.4 Summary

In this chapter, we designed and evaluated a contractile microneedle patch that regulated the stress environment in wound area for scar reduction. The whole system consisted of three parts: the backing layer, the middle part, and the tilted part. The backing layer was flexible and elastic to resist tension force from the surrounding tissue. The middle part was stiffer for insertion into the wound bed and releasing the local stress generated by myofibroblasts. The tilted part was inserted into the surrounding tissue for tissue adhesion and force transduction. The contractile microneedle patch showed better tissue adhesion than pure backing layer and common microneedle patches. Using two *in vitro* scar models, the proposed microneedle system significantly reduced some scar-related protein (α-SMA, CXCL 14) expressions and countered inflammation by down-regulating some inflammatory proteins (iNOS, TNF-α) while up-regulating anti-inflammatory protein (IL-10). RNA sequencing revealed that our patch could decrease the scar formation by down-regulating some mechanical signaling pathways, including ECM-receptor interaction,

PI3K signaling pathway, and focal adhesion.

Chapter 4 Self-powered cardiac patch integrated with microneedle and aligned piezoelectric microfibers for myocardial infarction treatment

4.1 Introduction

As one of the most vigorous organs, the heart is the power source of the blood circulation system. A decrease or even blockage of blood flow in the heart due to vascular occlusion can cause myocardial infarction (i.e., heart attack) and damage cardiac muscles. As cardiomyocytes are highly differentiated with limited proliferation, the damage is irreversible and would further deteriorate into heart failure, which is the leading cause of death worldwide, resulting in enormous health and financial burden.[177]

Current therapies for myocardial infarction include pharmacotherapy, stent implantation, and cell transplantation.[178] Although conventional pharmacotherapy can delay the progression of heart failure and decrease mortality, it cannot restore the functions of cardiomyocytes and vasculature.[179] Stent implantation is also accompanied by complication and immune attack. Cell transplantation suffers from low cell viability and retention and limited cell source.[180]

In recent years, engineered cardiac patches, which can provide mechanical support, physical and chemical stimulation to cardiomyocytes, promoting their growth and regeneration, have gained significant attention as a potential alternative. Specifically,

the physical stimulation mainly contains micro/nano-topographical structures, mechanical stimulation, and electrical stimulation.[50, 77, 181, 182] Micro/nano-topographical structures are primarily used to induce the directional growth of cardiac cells to mimic the in *vivo* environment. In natural cardiac tissue, cardiomyocytes are highly organized, forming transverse and longitudinal fiber bundles, which facilitate coordinated contraction and relaxation. Additionally, mechanical stimulation is crucial for cardiac functional repair. Mechanical stretching and pressure can simulate the physiological environment that cardiomyocytes experience in the heart, promoting cell proliferation, differentiation, and morphological changes. Electrical stimulation is also widely applied in cardiac repair research. Cardiomyocytes coordinate contraction and relaxation through the conduction of electrical signals between cells. Electrical stimulation can simulate this process and promote synchronized contraction of cardiomyocytes and normal heart function. Compared to topographical structures and mechanical stimulation, electrical stimulation is more direct and effective because the contractile function of cardiomyocytes relies on the conduction of electrical signals, i.e., the opening and closing of intracellular ion channels and the flow of ions. However, there are still two major challenges in achieving electrical stimulation in cardiac patches. One is the availability of long-term power supply. Currently, long-term power supply can only be achieved using an external power source and delivering electricity into the body through power cables. This poses a high risk of infection and inconvenience for patients. The second challenge is achieving electrical stimulation that matches the original heartbeat rhythm. External artificial electrical

stimulation often requires complex sensing instruments and current output devices to achieve synchronized electrical stimulation with the heart, which is expensive and relies on professional operators. Piezoelectric polymers (e.g., PVDF, PVDF-TrFE, poly (L-lactic acid) (PLLA)) have proved their capacity to generate electrical currents under mechanical stimuli, as well as good biocompatibility. With cyclic stretching of surrounding heart tissues, piezoelectric patch can generate electricity matching the natural heartbeat. So far, most of piezoelectric patches are used for energy harvesting or biosensing.[183] Hence, implantable piezoelectric cardiac patch for myocardial infarction or cardiac regeneration still needs to be investigated.

In this chapter, we propose a self-powered cardiac patch integrated with microneedle and aligned PVDF microfibers for myocardial infarction treatment. The microneedle was based on P_mL_nDMA, which has good biocompatibility and tunable mechanical properties. By tuning the ratio of propylene glycol to lactide in P_mL_nDMA, the patch could withstand long-term cyclic stretching. On the other hand, the highly aligned PVDF fibers coated on the microneedle was fabricated by EHD printing. The final system could simultaneously provide electrical stimulation, topological induction, and mechanical stimulation to cells. With all these properties, the cardiac patch could be promising for cardiac tissue regeneration.

4.2 Methodology

4.2.1 EHD printing of PVDF

The PVDF powder, with an average molecular weight of 500,000g/mol, was purchased from Arkema Investment Co. Ltd and used without further purification. PVDF powder was added to a solvent composed of DMF and acetone. The suspension was heated at 40℃ overnight to form a transparent PVDF solution.

A custom-built EHD printing device (EFL-BP6601, Suzhou Intelligent Manufacturing Research Institute, Suzhou, China) was used. 20 wt% PVDF in DMF/acetone (8:2) solvent was taken as an example. The PVDF solution was added to the stainless barrel of the printer. The inner diameter of the nozzle was 350μm. A glass slide with 700-μm thickness was used as substrate. The distance between the nozzle and substrate was 0.5mm. The air pressure for material extrusion was 1-2kPa. The voltage between the nozzle and substrate was 2-3kV exerted by a power supplier (DW-P403, Dongwen Inc.) to generate jetting flow.

To peel off the PVDF fibers from the substrate, a polycaprolactone frame was printed around the PVDF fibers with fused deposition modeling. The frame could combine with and support the PVDF fiber and was peeled off along with the PVDF fiber.

4.2.2 Piezoelectric property characterization of PVDF

4.2.2.1 FTIR of PVDF

To further confirm the polarization of PVDF, infrared radiation spectroscopy was conducted using an attenuated total reflectance FTIR spectrophotometer (ATR-FTIR,

Thermo Nicolet iS5, US). Infrared spectroscopy absorption at 763 and 840 cm^{-1} were selected to represent α and β phases in PVDF.[184] F(β), which is the relative faction of the β phase, was calculated using the formula as follows:

$$F(\beta)=\frac{A_\beta}{\frac{K_\beta}{K_\alpha}A_\alpha+A_\beta}$$

A_α and A_β are the absorbances at 763 and 840 cm^{-1}, respectively. K_α and K_β are the absorption coefficients at 763 and 840 cm^{-1}, respectively. $K_\alpha = 6.1 \times 104\ cm^2/mol$ and $K_\beta = 7.7 \times 104\ cm^2/mol$,[184] so the formula becomes:

$$F(\beta)=\frac{A_\beta}{1.262A_\alpha+A_\beta}$$

4.2.2.2 Measurement of output current in PVDF fiber

To measure the output current of the polarized PVDF fibers under cyclic stretching, a multimeter (Keithley 2000) was used for electrical signal collection. Meanwhile, a homemade mechanical testing system was used for cyclic stretching and could tune the stretching rate and amplitude. Two copper tapes were attached to the PVDF fibers as electrodes to ensure sufficient contact between fibers and electrodes.

To further remove the influence of triboelectricity or other noise from the environment, the whole circuit was packaged with polydimethylsiloxane (PDMS). In brief, uncured PDMS solution was prepared by mixing PDMS precursor and curing agent in a ratio of 10:1. PVDF fibers with electrodes were first placed in a mold with a square groove. Then, uncured PDMS solution was poured into the mold, degassed in a vacuum chamber for 30 min, and finally put into the thermostat for curing at 70℃

for 2 h. The packaged circuit was used for testing.

4.2.3 Fabrication process of the cardiac patch

P_mL_nDMA with different ratios of propylene glycol and lactide (i.e., P_7L_2DMA, $P_{68}L_8$DMA) was chosen as the base material of microneedles. The synthetic process has been discussed in section 2.2.2 and section 3.2.2. To form a photocrosslinkable P_mL_nDMA precursor, a mixture of P_mL_nDMA and HEMA solution containing Irgacure 819 (with a concentration of 10 wt% Irgacure 819 in HEMA) was prepared at a ratio of 9:1 (w/w).

Firstly, 50 μL P_7L_2DMA precursor was added into a PDMS mold (Y61, Weixinyiyao technology, China) and put into a vacuum chamber to remove the bubbles between the mold and solution for 20 min. As P_7L_2DMA was only used to form the needle tip, excessive P_7L_2DMA precursor was scraped off. Then, the P_7L_2DMA precursor in the needle tip cavities of the mold was semi-crosslinked using a 405-nm blue light source for 5-7 s. Subsequently, the PVDF fibers fabricated in section 4.2.1 were dipped with $P_{68}L_8$DMA precursor, forming a thin coating, then placed in the mold with the semi-crosslinked P_7L_2DMA needle tips. A 405-nm blue light was used again to semi-crosslink the $P_{68}L_8$DMA precursor coated on the PVDF fibers to combine the PVDF layer with the P_7L_2DMA needle tips. Finally, 100 μL $P_{68}L_8$DMA precursor was added into the mold, vacuumed for 20 min, and fully crosslinked using 405-nm blue light for 1 min to obtain the PVDF-coated microneedle cardiac patch.

4.2.4 Morphology and elemental analysis

The general cardiac patch morphology was detected using SEM (Tescan VEGA3, Czech Republic) after gold sputtering using a sputter coater. To observe the distribution of PVDF fibers on the cardiac patch, an energy-dispersive X-ray (EDX) spectrometer (Oxford) was used for elemental analysis. To observe PVDF fiber distribution on a glass slide after EHD printing, an inverted microscope (Nikon, Japan) was used.

4.2.5 Mechanical test

A mechanical testing system (ElectroForce 3200, Bose, America) was used for the tensile and cyclic stretching tests of P_mL_nDMA (i.e., P_7L_2DMA, $P_{34}L_4$DMA, $P_{68}L_8$DMA) and $P_{68}L_8$DMA/PVDF composite. For sample preparation, pure P_mL_nDMA materials were fabricated into dumbbell-shaped specimens using a mold casting technique, while $P_{68}L_8$DMA/PVDF samples were produced by coating PVDF fibers on the pure $P_{68}L_8$DMA materials. The initial length of each sample was 5 mm. For the tensile test, the extension rate was 0.1mm/s. For the cyclic stretching test, the samples were stretched with different maximal stretching ratios under the same frequency of 1 Hz. The maximal stretching ratios were 1.025, 1.05, 1.1, 1.2 for P_7L_2DMA and 1.2, 1.4, 1.6, 1.8 for $P_{68}L_8$DMA and $P_{68}L_8$DMA/PVDF. All the data were treated and analyzed by Origin software.

4.2.6 Calcium transient in H9c2 cells on culture dish

Before cell seeding, rat cardiomyoblasts (H9c2) (CRL-1446, ATCC) were cultured in DMEM (Gibco, Hong Kong) containing 10% (v/v) FBS (Gibco, Hong Kong) and 1% (v/v) PS (Gibco, Hong Kong). All cells were cultured at 37°C and 5% CO2 under humidified conditions. The culture medium was replaced every two days. H9c2 cells were then seeded at 1×10^5 cells per well in 24-well plates and observed 3 days after seeding. Calcium-sensitive Fluo-4 AM (10mM in DMSO, Thermo Fisher) was used to prepare the Fluo-4 AM loading solution consisting of 3μM Fluo-4 AM (reconstituted in DMSO) and 0.1% Pluronic F-127 in HBSS. Then, H9c2 cells in 24-well plates were loaded with Fluo-4 AM loading solution according to the user manual. Finally, the calcium activity of H9c2 cells was observed by a fluorescence microscope (Nikon, Japan).

4.2.7 Static and dynamic culture of H9c2 cells

Flat patches of P68L8DMA and P68L8DMA/PVDF with a thickness of 1 mm were first produced to prepare the samples for cell seeding. Then, PCL-based square frames, designed to avoid cells escaping from the material surface, with 5 × 5 × 1 mm in dimensions, were printed using a fused deposition modeling (FDM) 3D printer. Finally, the PCL-based square frames were combined firmly with the $P_{68}L_8$DMA and $P_{68}L_8$DMA /PVDF patches using the $P_{68}L_8$DMA precursor. These samples were sterilized using ultraviolet light and 75% (v/v) ethanol. For better cell adhesion, all the samples were pre-treated with a gelatin (0.2mg/mL)/fibronectin (5μg/mL) solution for

over 2 h. H9c2 cells were seeded at 1×10^4 cells/cm^2 on each sample and cultured in full DMEM. For observation of cell morphology, 4% paraformaldehyde was used to fix cells, which were then permeabilized with 1% Triton X-100 for 30 min and blocked for 1 h under room temperature. Subsequently, samples were incubated in Alexa Fluor 488-conjugated phalloidin solution (1:200 dilution) for 45 min and DAPI solution (1:1000 dilution) for another 5 min in the dark at room temperature. The samples were washed three times by PBS and then examined by a fluorescence microscope (Nikon, Japan).

For the dynamic culture of H9c2 cells, a custom-made mechanical stretching device was used to stretch the H9c2 cells on $P_{68}L_8$DMA and $P_{68}L_8$DMA/PVDF. Briefly, two sides of the samples were anchored by two magnetic clamps coated with plastic membranes. The stretching of the samples was induced by the movement of the two magnetic clamps. To control the movement of the magnetic clamps, a linear motor, which was placed outside the petri dish beneath the samples and magnetic clamps, was equipped with two magnets to attract the magnetic clamps. Finally, the movement of the magnetic clamps was controlled by programming the linear motor to stretch the samples under a certain frequency and amplitude.

After seeding H9c2 cells on the samples for 3 days, allowing for sufficient cell adhesion, the cell-loaded samples were placed on the mechanical stretching device. Cyclic stretching (1 Hz, 5% strain) was applied for 24 h. For observation of some

cardiac function-related proteins (α-actinin, MLC-2V, COX-43), 4% paraformaldehyde was used to fix cells, which were then permeabilized with 1% Triton X-100 for 10 min and blocked for 1 h under room temperature. Subsequently, samples were incubated with primary antibodies, including anti-α-actinin (1:300, Abcam, ab137346), anti-MLC-2V (1:500, Abcam, ab48003), and COX-43 (1:500, Abcam, ab11370), at a temperature of 4 ℃ for the whole night. Then the samples were incubated with secondary antibodies, Alexa Fluor® 488 (1:500, ab150157, abcam), for 1 h and DAPI (1:1000 dilution) for another 10 min in the dark at room temperature. The samples were washed three times by PBS and examined by confocal microscope (TCS SPE, Leica).

4.2.8 *In vivo* therapeutic test

New Zealand rabbits with weight from 2.5 to 3.5 kg were employed to establish this MI model. The animal experiment was finished with the help of Wuhan Servicebio Technology Co., Ltd. Before this procedure, the rabbits were anesthetized and positioned in the supine position. A median sternotomy was performed to expose the anterior surface of the heart, and the pericardium was incised. To induce an acute myocardial infarction (MI), the ligation of the left anterior descending (LAD) artery was performed at the midpoint between the initial point and the apex of the heart by suture.

Five groups were involved in the test: control (no induced MI or treatment), MI (no

treatment), PTFE (PTFE membrane treatment with 20-mm diameter and 0.8-mm thickness), MN (pure microneedle patch treatment), and MN+PVDF (PVDF fiber-coated microneedle patch treatment). For the control group, rabbits underwent no induced MI or treatment, and 6 samples were collected on day 1. For the remaining groups, rabbits were induced with acute MI and treated accordingly, and 6 samples were collected on days 1, 7, and 28. Two extra samples were collected to confirm microneedle insertion. Considering the mortality (20% after 1 day, 30% after 7 days, and 50% after 28 days), the total quantity of rabbits was 120. For the implantation of PTFE, PTFE membranes were attached to the wound site using tissue adhesive (3M^{TM} Vetbond^{TM}). To implant MN and MN+PVDF, a customized apparatus consisting of an external pump, a suction cup, and a suction tube was used to create negative pressure to press the microneedle into the cardiac tissue. Then, to ensure long-term attachment of the microneedles to the heart surface, extra PTFE membranes were stuck to the heart surface by tissue adhesive, covering the microneedle samples.

4.2.9 Histology evaluation

The tissue sections were treated with H&E, Masson's trichrome, and Picrosirius red staining to observe the cardiac tissue's general morphology, fibrosis, and collagen content. Quantitative data of scar area, collagen content, and collagen I/III ratio were measured using ImageJ. LY6G, α-SMA, and TUNEL immunostaining (Servicebio, China) were conducted to evaluate the inflammation, angiogenesis, and cell apoptosis. Quantitative data of fluorescence intensity, arterial density, and TUNEL^{+} apoptotic

cell numbers were measured or counted using ImageJ.

4.2.10 Statistical analysis

GraphPad software was used for statistical analysis. Unless otherwise stated, all tests were repeated at least three times. Results are shown in mean ± standard deviation (SD). A normality test was conducted for each set of data. One-way ANOVA was used in comparing two different groups. P-value ≤ 0.05 was considered statistically significant (*p ≤ 0.05, **p ≤ 0.01, ***p ≤ 0.001).

4.3 Results and discussions

4.3.1 Fabrication and characterization of the cardiac patch

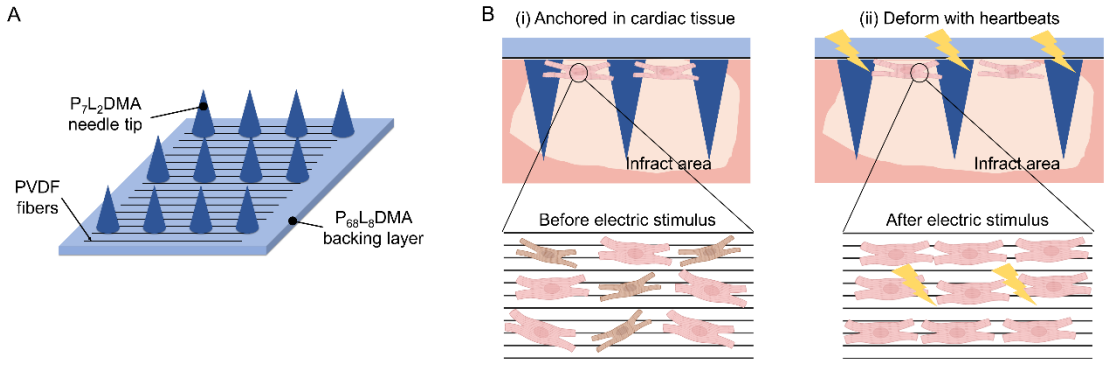

Figure 4-1. Schematic diagrams showing the (A) structural design of the cardiac patch, consisting of a $P_{68}L_8$DMA backing layer, P_7L_2DMA needle tips, and PVDF fibers coated on the surface of the backing layer, and (B) working principle of the cardiac patch. The cardiac microneedle patch is anchored in the cardiac tissue and deforms with heartbeats. The PVDF fibers could generate electricity during cyclic deformation and provide an electric stimulus to restore cardiomyocyte functions.

The self-powered cardiac patch consisted of a $P_{68}L_8$DMA backing layer, P_7L_2DMA needle tips, and PVDF fibers coated on the surface of the backing layer (**Figure 4-1**A). Similar to the design in Chapter 3, needle tips were fabricated using P_7L_2DMA to be stiff enough to insert into the cardiac tissue while the backing layer was made of $P_{68}L_8$DMA to be elastic enough to deform with cardiac tissues. PVDF fibers coated on the backing layer would also be stretched with the heartbeats and generate electricity due to its piezoelectric property to stimulate the damaged cardiomyocytes and to restore cardiac function (**Figure 4-1**B).

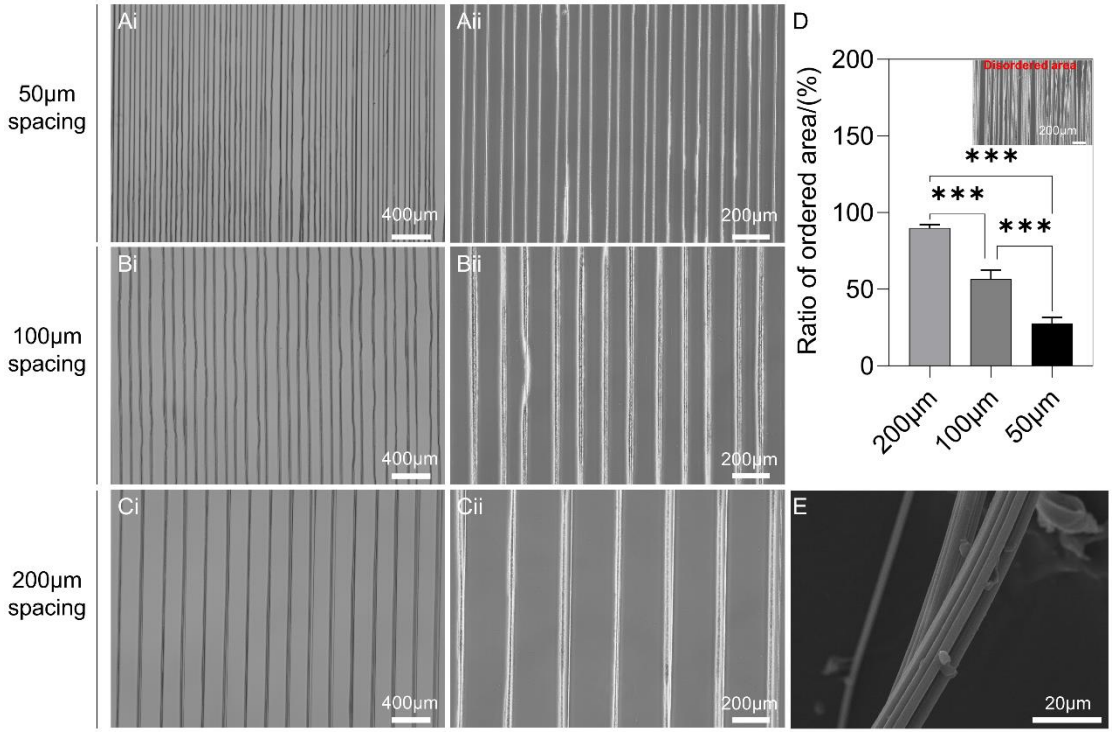

Figure 4-2. EHD printing of PVDF fibers. (A) Printed PVDF fibers with 50-μm spacing. (B) Printed PVDF fibers with 100-μm spacing. (C) Printed PVDF fibers with 200-μm spacing. (D) Quantitative analysis of the ratio of ordered area in the whole printing area. (E) SEM image of stacked PVDF fibers. The differences were

statistically significant when p values are below 0.001 (***).

PVDF made the patch self-powered and can only generate piezoelectricity by stretching and polarization in a strong electrical field. The high voltage electric field during EHD printing can polarize the PVDF fibers when stretching the jet of PVDF solution. In fact, as shown in **Figure 4-2**, EHD printing could get highly aligned PVDF fibers compared with other methods (e.g., spin coating, electrospinning, hot-press).[185] DMF/acetone mixture was used as the solvent to dissolve the PVDF powder for printing according to previous studies. [186, 187] After optimization of printing parameters, we found that 20 wt% PVDF in DMF/acetone mixture at 8:2 (w/w) ratio showed the best printability. With this material ratio, highly aligned PVDF fibers with tunable spacing, including 50 μm, 100 μm, and 200 μm (**Figure 4-2**A-C), could be obtained (the number of printing layer was set to 10). However, due to the limitations of the EHD printing, when the printing spacing decreases, the adjacent fibers may adhere to each other due to electrostatic attraction and form a disordered area. As shown in **Figure 4-2**D, the ratios of ordered area with 200-μm, 100-μm, and 50-μm spacings were 89.97%, 56.57%, and 27.63%, respectively. When the printing spacing was below 50 μm, over 90% of the printed PVDF fibers were disordered and the printing process was uncontrollable. **Figure 4-2**E is the SEM image of the stacked PVDF fibers, indicating that several layers of PVDF fibers could be produced by EHD printing. Therefore, ordered areas of the aligned PVDF fibers with 50-μm spacing were used for further fabrication.

After fabricating the aligned PVDF fiber sheet, a multistep micromolding technique was used to fabricate the PVDF-coated microneedle cardiac patch. P_7L_2DMA precursor was first added into a PDMS mold and vacuumed to remove the bubbles. Excessive P_7L_2DMA precursor outside of the needle tip cavities was scraped off and the remaining P_7L_2DMA precursor was semi-crosslinked using 405-nm blue light for 5-7 s. Subsequently, the PVDF fibers were dipped with $P_{68}L_8$DMA precursor forming a thin layer on fibers and then placed in the mold with semi-crosslinked P_7L_2DMA needle tips. Blue light (405 nm) was used again to semi-crosslink the $P_{68}L_8$DMA precursor coated on the PVDF fibers to combine the PVDF layer with the P_7L_2DMA needle tips. Finally, 100 μL $P_{68}L_8$DMA precursor was added into the mold, vacuumed for 20 min, and fully crosslinked using 405-nm blue light for 1 min to obtain the PVDF-coated microneedle patch cardiac patch.

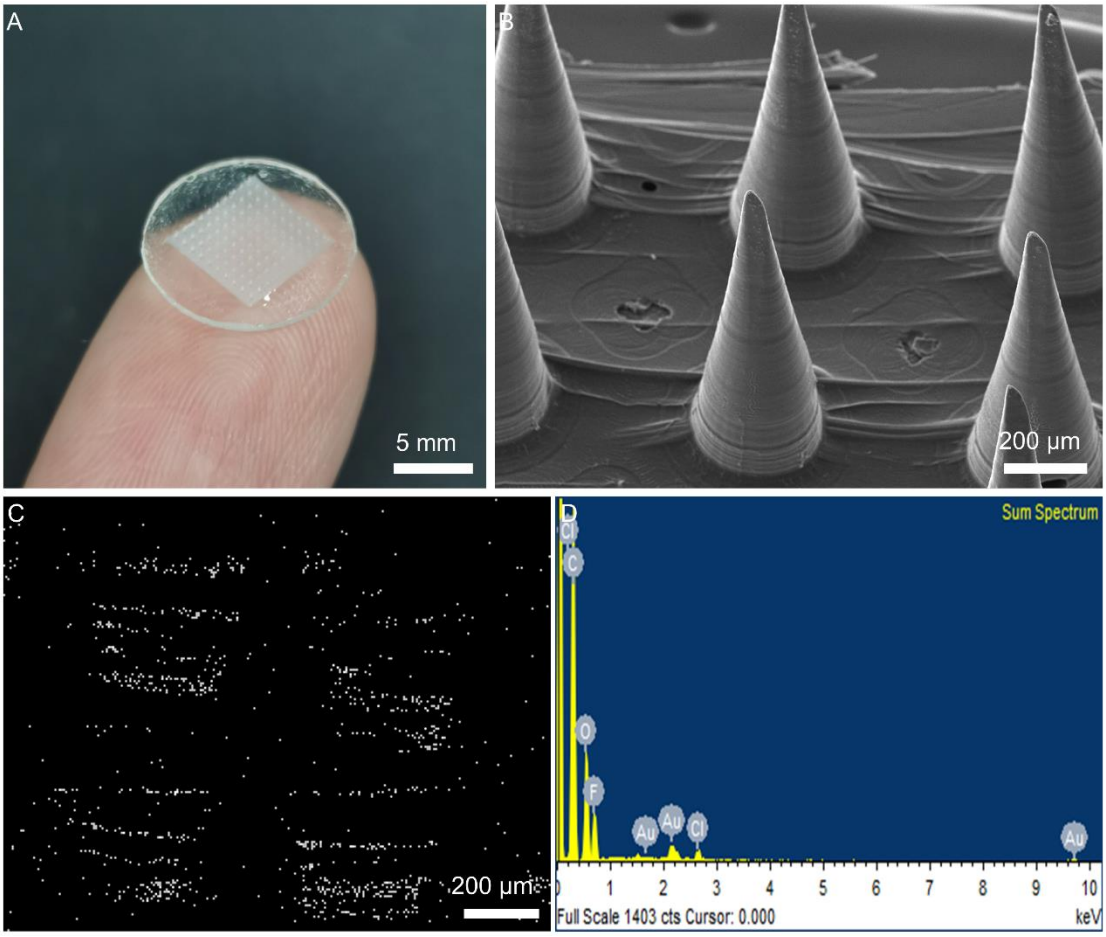

Figure 4-3. Morphology characterization and elemental analysis of the cardiac patch. (A) General appearance of the cardiac patch. (B) SEM image of the cardiac patch showing the needle tips and the coated aligned PVDF fibers. (C) Analysis of fluorine distribution using SEM-EDS. (D) SEM-EDS sum spectrum showing the elemental composition of the cardiac patch.

Figure 4-3A shows the general appearance of the cardiac patch. The diameter of the backing layer was 12 mm and the dimension of the PVDF-coated microneedle area was 6.5 × 6.5 mm to fit the size of a rabbit heart. **Figure 4-3**B is SEM image showing the microstructure of the PVDF-coated microneedle with 600-µm height, 250-µm base diameter, and 500-µm spacing. To further confirm the successful coating of the

PVDF fibers and its distribution, a SEM-EDS analysis was conducted. As shown in **Figure 4-3**C, fluorine, which only existed in PVDF, was marked with white color, indicating that the fibers shown in **Figure 4-3**B were indeed PVDF. **Figure 4-3**D is the SEM-EDS sum spectrum, which further shows the elemental composition of the sample. From the quantitative result, the weight percent of fluorine was 19.81% and the atomic percent of fluorine was 14.90%.

4.3.2 Piezoelectricity of PVDF fibers

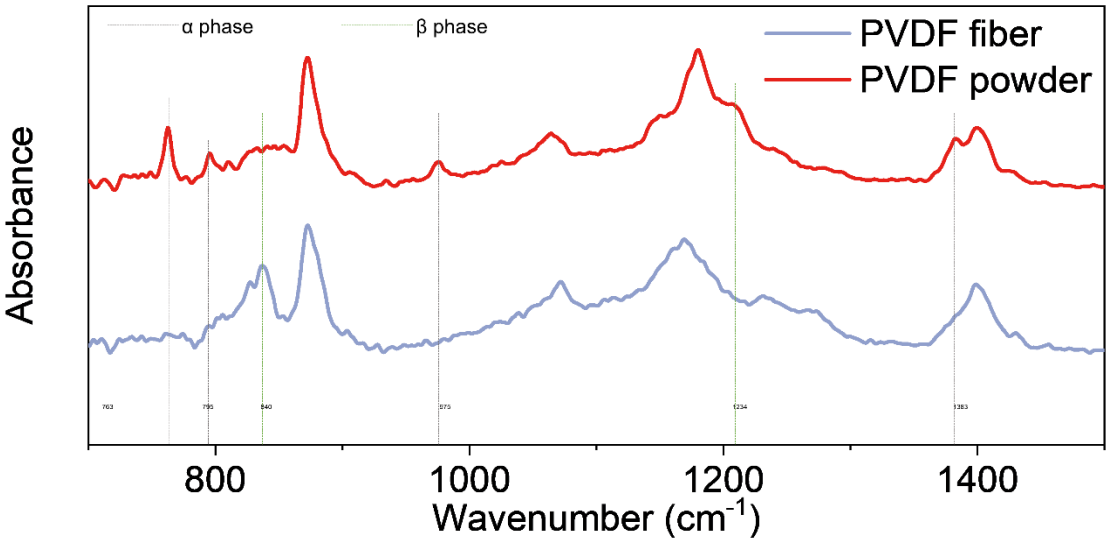

Figure 4-4. FTIR spectra of PVDF fiber printed by EHD printing and PVDF powder.

There are three main crystalline phases (i.e., α, β, and γ) in PVDF and β phase is primarily responsible for its piezoelectric properties. After polariztion, the non-polar α phase can be transformed to β phase.[188, 189]. In section 4.3.1, after the polarization of EHD printing, non-polar α phase in PVDF solution transform into β phase. **Figure 4-4** shows the FTIR spectra of PVDF fiber created by EHD printing and raw PVDF

powder. The curve of PVDF fiber had strong peaks at 840 cm^{-1} and should be strong in β phase, while the curve of PVDF powder had strong peaks at 763 and 795cm^{-1}, indicating the α phase. We substituted the absorbance values at 763 and 840 cm^{-1} into the formula:

$$F(\beta)=\frac{A_\beta}{1.262A_\alpha+A_\beta}\times 100\%$$

F(β) (i.e., relative fraction of the β-phase content in the total crystallinity) before and after polarization were 35.7% and 78.3% respectively. The increase in F(β) indicated β-phase content increase after EHD printing and that the polarization was successful.

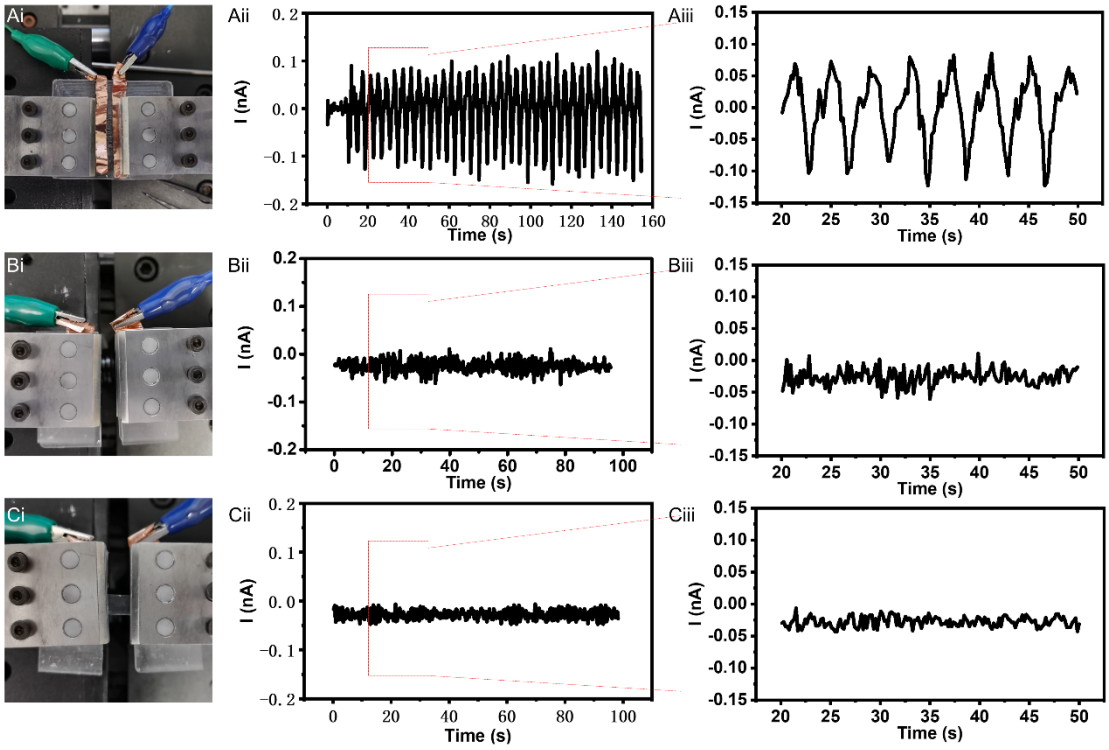

Figure 4-5. Comparison of piezoelectric property between (A) 1 layer of PVDF fiber under 50% stretch, (B) open circuit, and (C) PDMS. (Ai), (Bi), and (Ci) are images of experiment setting. (Aii), (Bii), and (Cii) are the current change under cyclic stretching in different groups. (Aiii), (Biii), and (Ciii) are enlarged charts of (Aii),

(Bii), and (Cii).

To further confirm the piezoelectricity of PVDF fiber, a multimeter was used to directly measure the output current of PVDF fibers, as shown in **Figure 4-5**Ai. Details about the circuit are discussed in section 4.2.2.2. In **Figure 4-5**Aii, one layer of PVDF fiber could generate periodic current with a 0.1-nA amplitude under 50% strain at 0.2 Hz. **Figure 4-5**Aiii shows detailed current curve indicating good responsiveness of PVDF fiber to cyclic stretching. To exclude external noise and triboelectricity, two control groups, namely open circuit (**Figure 4-5**B) and PDMS (**Figure 4-5**C), were used for further investigation. In **Figure 4-5**Bii-iii and **Figure 4-5**Cii-iii, the two control groups did not generate effective periodic current signal but random noise. These results proved that the PVDF fibers possessed good piezoelectricity after EHD printing.

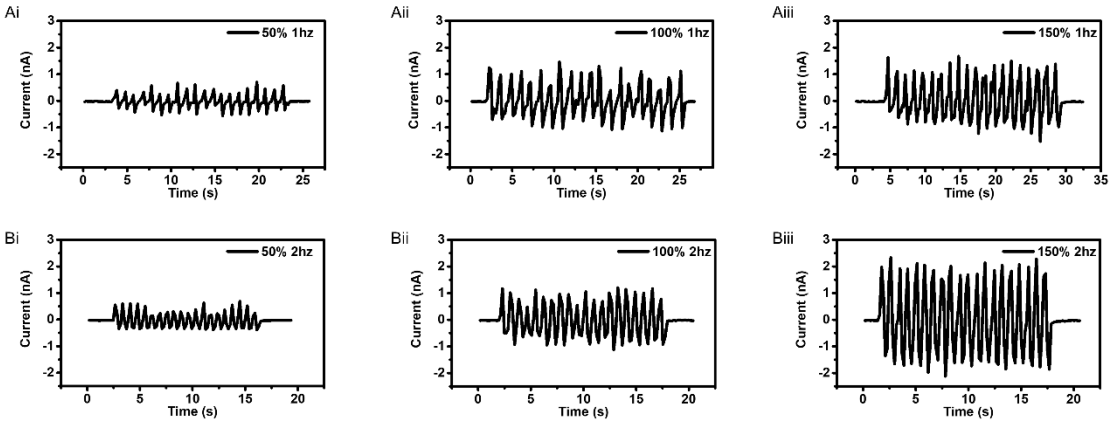

Figure 4-6. Current output of 10 layers of PVDF fiber under (A) 1-Hz stretching frequency with (i) 50%, (ii) 100%, and (iii) 150% strain rate; (B) 2-Hz stretching frequency with (i) 50%, (ii) 100%, and (iii) 150% strain rate.

To investigate the effects of stretching frequency and amplitude on current signal, two different stretching frequencies (i.e., 1 Hz and 2 Hz) and three different stretching amplitudes (i.e., 50%, 100%, and 150%) were exerted on 10 layers of PVDF fibers. In **Figure 4-6**A and **Figure 4-6**B, the amplitude of the current signal increased with stretching amplitude, from 0.5 nA under 50% stretching (**Figure 4-6**Ai and **Figure 4-6**Bi) to about 2 nA under 150% stretching (**Figure 4-6**Aiii and **Figure 4-6**Biii). Stretching frequency did not show significant influence on the current output when comparing **Figure 4-6**A to **Figure 4-6**B.

4.3.3 Mechanical property of the cardiac patch

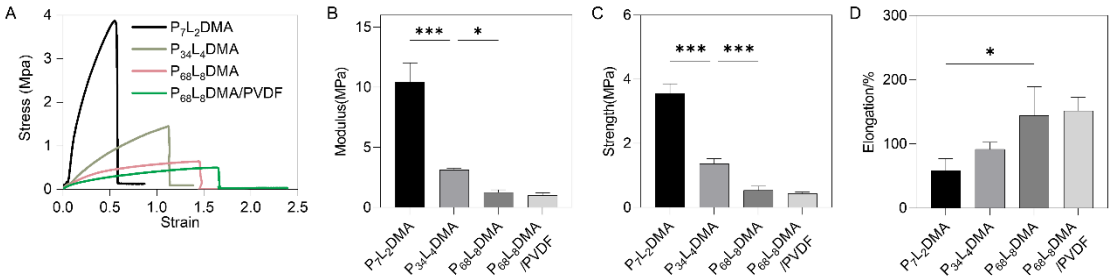

Figure 4-7. Mechanical properties of P_7L_2DMA, $P_{34}L_4DMA$, $P_{68}L_8DMA$, and $P_{68}L_8DMA$/PVDF composite. (A) Stress-strain curve of different materials. Quantitative comparation of (B) modulus, (C) strength, and (D) elongation. The differences are statistically significant when p values are below 0.05 (*) and 0.001 (***).

As mentioned above, the microneedle tips should be stiff enough to penetrate the cardiac tissue while the backing layer should be elastic enough to deform with the

heartbeat and withstand long-term cyclic stretching. To choose the most suitable base material, tensile (**Figure 4-7**) and cyclic stretching tests (**Figure 4-8**) were conducted on P_mL_nDMA with different ratios of propylene glycol to lactide (i.e., P_7L_2DMA, $P_{34}L_4DMA$, $P_{68}L_8DMA$) and $P_{68}L_8DMA$/PVDF composite. **Figure 4-7**A shows the stress-strain curve of different groups. P_7L_2DMA had the highest modulus (10.41 MPa, **Figure 4-7**B) and strength (3.55 MPa, **Figure 4-7**C) but the lowest elongation rate (58.68%, **Figure 4-7**D) among all groups. On the contrary, $P_{68}L_8DMA$ had the lowest modulus (1.26 MPa, **Figure 4-7**B) and strength (0.538 MPa, **Figure 4-7**C) but the highest elongation rate (141.66%, **Figure 4-7**D). $P_{34}L_4DMA$ had a medium value compared with P_7L_2DMA and $P_{68}L_8DMA$. After coating with PVDF fibers, the modulus, strength, and elongation rate of $P_{68}L_8DMA$/PVDF composite showed no significant change, potentially because the PVDF fiber sheet was too thin compared with $P_{68}L_8DMA$.

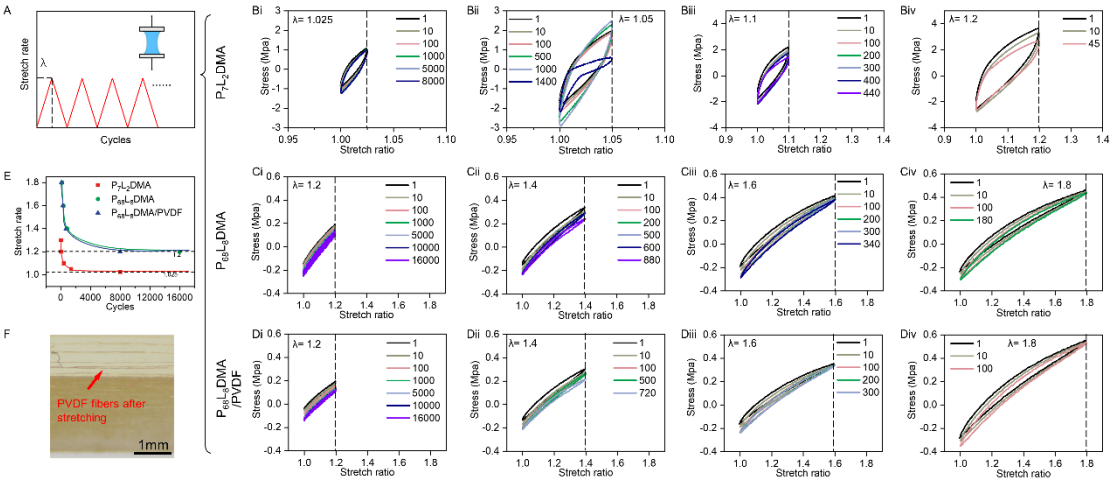

Figure 4-8. Cyclic stretching test of P_7L_2DMA, $P_{68}L_8DMA$ and $P_{68}L_8DMA$/PVDF composite. (A) Cyclic mechanical test setting. (Bi)-(Biv) Stress-stretch ratio

hysteresis curve of P_7L_2DMA under 2 hz with different maximum stretch ratio λ from 1.025 to 1.2. (Ci)-(Civ) Stress-stretch ratio hysteresis curve of $P_{68}L_8$DMA under 2 hz with different maximum stretch ratio λ from 1.2 to 1.8. (Di)-(Div) Stress-stretch ratio hysteresis curve of $P_{68}L_8$DMA/PVDF under 2 hz with different maximum stretch ratio λ from 1.2 to 1.8. (E) Fatigue limit curve of three P_7L_2DMA, $P_{68}L_8$DMA, and $P_{68}L_8$DMA /PVDF composite. (F) Images showing the PVDF fibers after the cyclic stretching.

For the backing layering to withstand long-term cyclic stretching, the fatigue limit is important, as shown in **Figure 4-8. Figure 4-8**A shows the experimental setup of cyclic stretching, where λ stands for the maximal stretch ratio (i.e., maximum length/initial length) and the stretching frequency was set to 1 Hz. **Figure 4-8**B shows the stress-stretch ratio curve of P_7L_2DMA at different cycles under different λ values (i.e., 1.025, 1.05, 1.1, 1.2). With the λ increasing, the maximal cycle number that P_7L_2DMA could withstand decreased. In addition, according to the stress-stretch ratio curve of P_7L_2DMA, the tensile part was significantly higher than the release part, suggesting high hysteresis of P_7L_2DMA. This indicates that large energy loss or dissipation occurs during the loading and unloading cycles and that P_7L_2DMA is not perfectly elastic. **Figure 4-8**C shows the stress-stretch ratio curve of $P_{68}L_8$DMA at different cycles under different λ value (i.e., 1.2, 1.4, 1.6, 1.8). Different from P_7L_2DMA, $P_{68}L_8$DMA had much less hysteresis, as the tensile part and release parts of the curves could almost overlap with each other. Therefore, $P_{68}L_8$DMA could

respond to the cyclic stretching faster which is crucial in high frequency movement. **Figure 4-8**D shows the stress-stretch ratio curve of $P_{68}L_8$DMA/PVDF composite at different cycles under different λ values (i.e., 1.2, 1.4, 1.6, 1.8). They show no significant difference to pure $P_{68}L_8$DMA. From **Figure 4-8**E, only when λ was less than or equal to 1.025, P_7L_2DMA could bear over 8000 stretching cycles, indicating that P_7L_2DMA cannot withstand cyclic stretching under too large strain. Additionally, $P_{68}L_8$DMA has higher fatigue limit than P_7L_2DMA. It could bear over 16,000 cycles of stretching under a maximal stretch ratio of 1.2. This is much higher than that of P_7L_2DMA, indicating that $P_{68}L_8$DMA is much more suitable to withstand long-term cyclic stretching. **Figure 4-8**F shows that the PVDF fibers still adhere to the $P_{68}L_8$DMA layer after the cyclic stretching test, indicating the tight combination of the fibers and $P_{68}L_8$DMA.

According to the tensile and cyclic stretching tests, P_7L_2DMA was chosen as the needle tip and $P_{68}L_8$DMA the backing layer. Nonetheless, their long-term mechanical properties after immersion in water are also crucial, as the cardiac patch would remain in the body for an extended period and come into contact with bodily fluids.

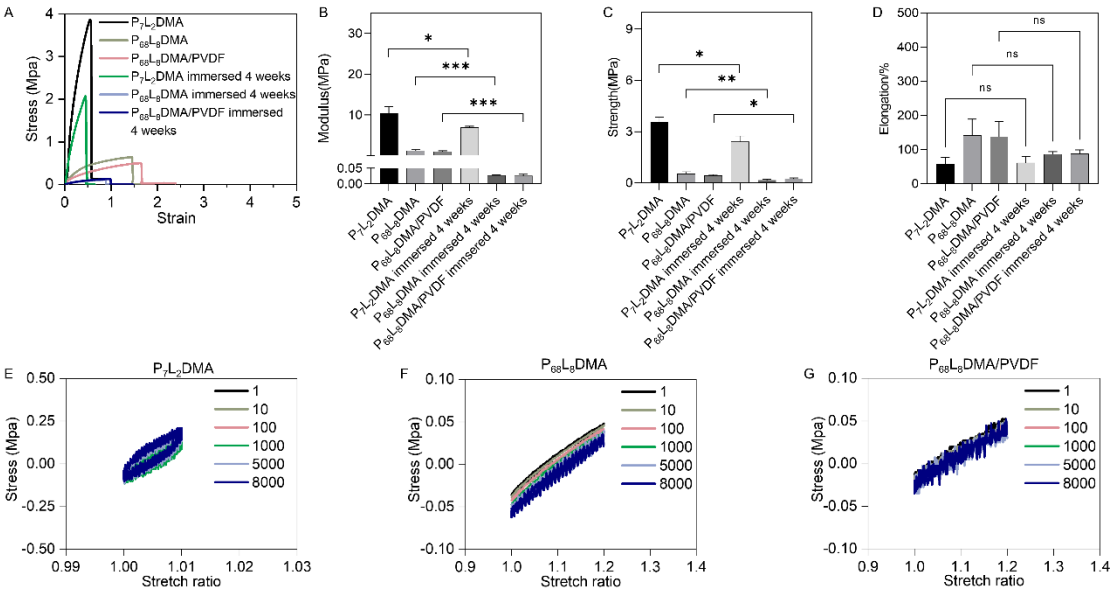

Figure 4-9. Mechanical properties of P_7L_2DMA, $P_{68}L_8DMA$, and $P_{68}L_8DMA/PVDF$ composite after being immersed in water for 4 weeks. (A) Stress-strain curve of P_7L_2DMA, $P_{68}L_8DMA$, and $P_{68}L_8DMA/PVDF$ without water immersion, and 4-week water immersion. Quantitative comparation of (B) modulus, (C) strength, and (D) elongation of P_7L_2DMA, $P_{68}L_8DMA$, and $P_{68}L_8DMA/PVDF$ with or without a 4-week water immersion. (E) Stress-stretch ratio hysteresis curve of P_7L_2DMA after 4-week water immersion under 2 Hz with maximum stretch ratio λ of 1.01. (F) Stress-stretch ratio hysteresis curve of $P_{68}L_8DMA$ after 4-week water immersion under 2 Hz with maximum stretch ratio λ of 1.2. (G) Stress-stretch ratio hysteresis curve of $P_{68}L_8DMA/PVDF$ after 4-week water immersion under 2 Hz with maximum stretch ratio λ of 1.2. The differences are statistically significant when p values are below 0.05 (*), 0.01 (**), and 0.001 (***).

Figure 4-9 illustrates the alterations in the mechanical properties of P_7L_2DMA, $P_{68}L_8DMA$, and $P_{68}L_8DMA/PVDF$ composite after being immersed in water for 4

weeks. **Figure 4-9**A shows the stress-strain curves of different groups. P_7L_2DMA exhibits significantly higher strength compared to the other groups, even after being immersed in water for 4 weeks, although its strength slightly decreases but remains higher than the other groups. In contrast, its maximum elongation rate was significantly lower than the other groups both before and after immersion in water. The mechanical curves of $P_{68}L_8$DMA and $P_{68}L_8$DMA/PVDF groups were similar, indicating that the PVDF fibers did not affect the mechanical property of $P_{68}L_8$DMA. After immersion in water, the strength of $P_{68}L_8$DMA significantly decreased. From **Figure 4-9**B-D, after water immersion, modulus of P_7L_2DMA decreased significantly from 10.42 MPa to 6.93 MPa, and strength decreased from 3.55 MPa to 2.42 MPa, while elongation rate did not change significantly. Modulus of $P_{68}L_8$DMA also decreased significantly from 1.26 MPa to 0.027 MPa, and strength decreased from 0.538 MPa to 0.165 MPa, while elongation rate also did not change significantly. Mechanical properties of $P_{68}L_8$DMA and $P_{68}L_8$DMA/PVDF composite showed no significant difference. **Figure 4-9**E-G are the cyclic stretching results of P_7L_2DMA, $P_{68}L_8$DMA and $P_{68}L_8$DMA/PVDF composite after being immersed in water for 4 weeks. The fatigue limit of P_7L_2DMA decreased after water immersion, as the maximal stretch ratio dropped from 1.025 to 1.01 (**Figure 4-9**E). On the contrary, fatigue limits of both $P_{68}L_8$DMA and $P_{68}L_8$DMA/PVDF composite did not change significantly after immersion; they could still withstand a maximal stretch ratio of 1.2 (**Figure 4-9**F-G).

In conclusion, P_7L_2DMA was more suitable as the base material of the needle tips, due to its high stiffness. In contrast, $P_{68}L_8$DMA was more suitable as the base material of the backing layer, due to its good elasticity and high fatigue limit. As a result, these two materials were chosen as the base materials of the cardiac patch.

4.3.4 Calcium transient of H9c2 cardiomyoblasts

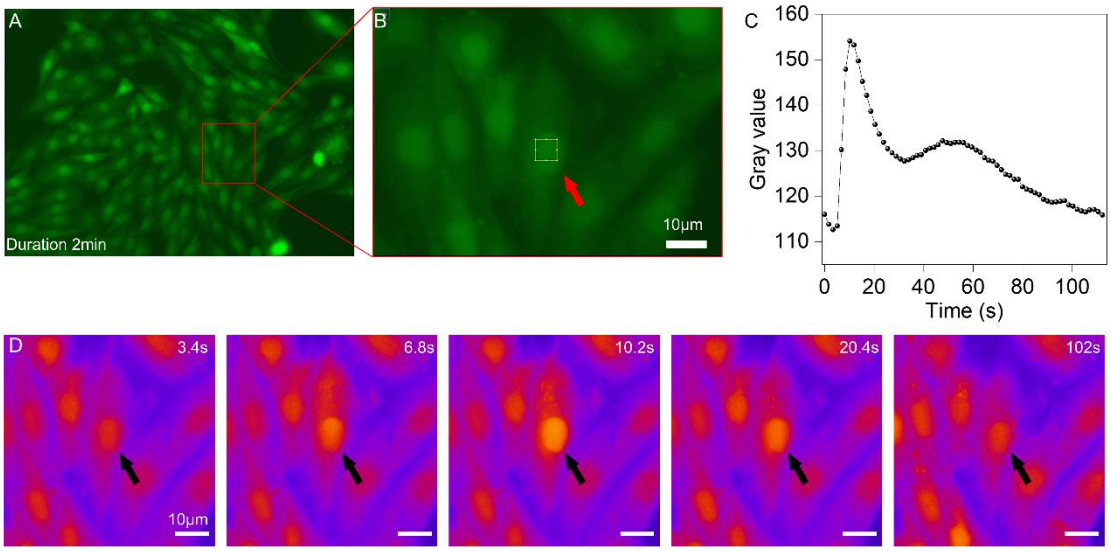

Figure 4-10. Calcium transient test in H9c2 cardiomyoblasts on culture dish for the verification of cell function. (A) Representative fluorescence image of intracellular calcium levels in H9c2 cardiomyoblasts using Fluo-4. (B) Enlarged view of (A); red arrow indicates the targeted area for gray value testing. (C) Gray value change during the whole process. (D) Image series showing change in fluorescence intensity in the targeted testing area (black arrow).

In this chapter, H9c2 cardiomyoblasts, which are commonly used in cardiac research and can differentiate into cardiomyocytes, were chosen for evaluating performance of

materials.[190] Cardiomyocytes contract and relax primarily by modulating the concentration of calcium ions inside and outside the cells. Therefore, calcium ion regulation is an important indicator for evaluating the cardiac function of the cells. In this section, calcium transient test (**Figure 4-10**) was conducted to confirm the calcium ion regulation of the H9c2 cardiomyoblasts *in vitro*. **Figure 4-10**A shows the intracellular calcium levels using Fluo-4 and **Figure 4-10**B is the targeted area for the following gray value testing (**Figure 4-10**C). The calcium levels in H9c2 cardiomyoblasts increased immediately in the initial 15 s and returned to the baseline in the following 80 s. To visualize the variation in fluorescence intensity, which indicates the change of intracellular calcium level, image series (**Figure 4-10**D) were taken. The concentration of calcium ions inside the cells (pointed by black arrows) had a rapid increase followed by a gradual decline, consistent with the trend in **Figure 4-10**C. In summary, the H9c2 cardiomyoblasts possessed normal regulatory function of calcium ions and were used in the following cell experiments.

4.3.5 Static culture of H9c2 cardiomyoblasts on the cardiac patch

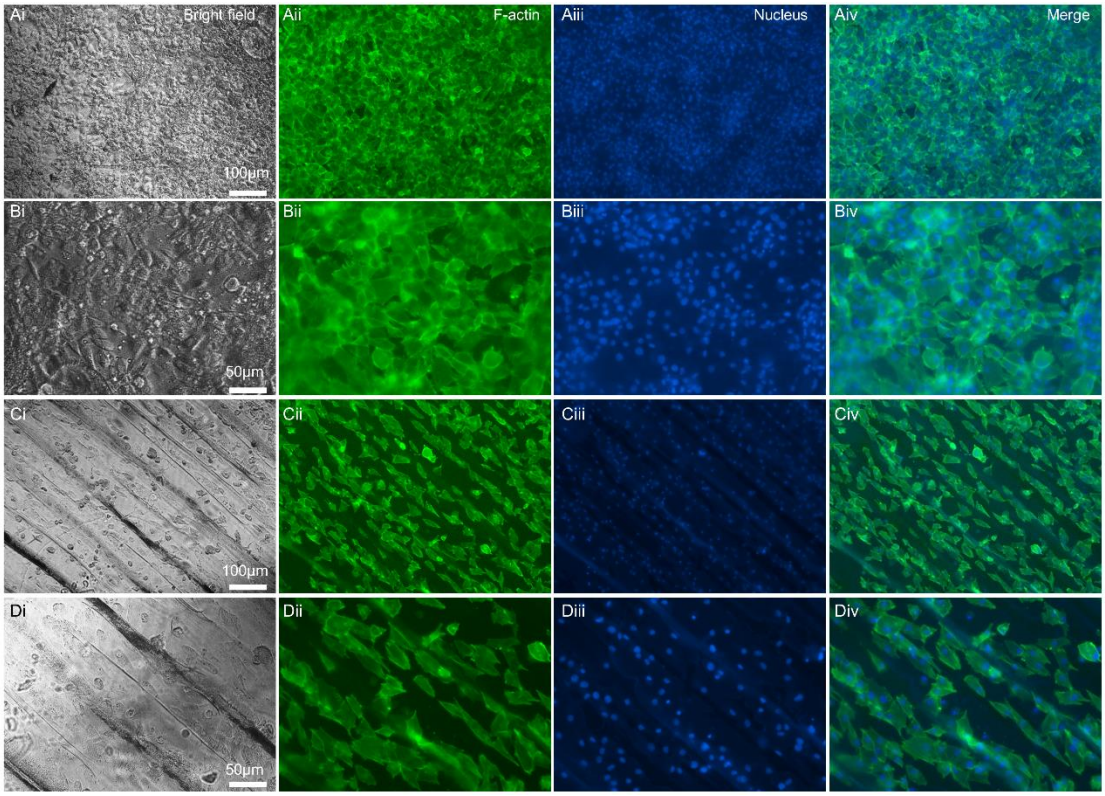

Figure 4-11. Morphology of H9c2 cardiomyoblasts on $P_{68}L_8$DMA and $P_{68}L_8$DMA/PVDF composite under 1 day of static culture. (A) Bright field image and fluorescence images of H9c2 cardiomyoblasts on $P_{68}L_8$DMA with F-actin stained in green and nuclei stained in blue, and (B) its enlarged view. (C) Bright field image and fluorescence images of H9c2 cardiomyoblasts on $P_{68}L_8$DMA/PVDF with F-actin stained in green and nuclei stained in blue, and (D) its enlarged view.

To further confirm the biocompatibility and cell adhesion property of the base materials, a preliminary static culture of H9c2 cardiomyoblasts on the cardiac patch was conducted. As the biocompatibility of P_7L_2DMA has been shown in chapter 2 and the cells mainly contact the $P_{68}L_8$DMA backing layer and PVDF fibers *in vivo*, H9c2 cardiomyoblasts were cultured on $P_{68}L_8$DMA and $P_{68}L_8$DMA/PVDF composite

samples. From **Figure 4-11**, H9c2 cells adhered to $P_{68}L_8$DMA and PVDF fibers well after 1 day. In addition, H9c2 cells exhibited a random distribution on $P_{68}L_8$DMA (**Figure 4-11**A-B) but a highly aligned growth along the PVDF fibers on $P_{68}L_8$DMA /PVDF composite (**Figure 4-11**C-D). Hence, PVDF fibers could induce oriented growth of H9c2 cells even in static cell culture. H9c2 cells may also prefer to adhere to the PVDF fibers, which is beneficial to functionalization in dynamic cell culture.

4.3.6 Dynamic culture of H9c2 cardiomyoblasts on the cardiac patch

To investigate the effects of cyclic stretching and piezoelectricity of the PVDF on H9c2 cardiomyoblast functions, 5% cyclic stretching at 1 Hz was applied to mimic the rhythmic contraction of the native myocardium. To uncouple the influence of mechanical stimulation from that of electrical stimulation, four groups (i.e., $P_{68}L_8$DMA/Static, $P_{68}L_8$DMA/Dynamic, $P_{68}L_8$DMA/PVDF/Static, and $P_{68}L_8$DMA/PVDF/Dynamic) were set. Samples for cell loading were made of $P_{68}L_8$DMA/PVDF composite where part of the area was coated with PVDF and the remaining was free of PVDF to make sure that cells in $P_{68}L_8$DMA/Dynamic and $P_{68}L_8$DMA/PVDF/Dynamic underwent the same stretching.

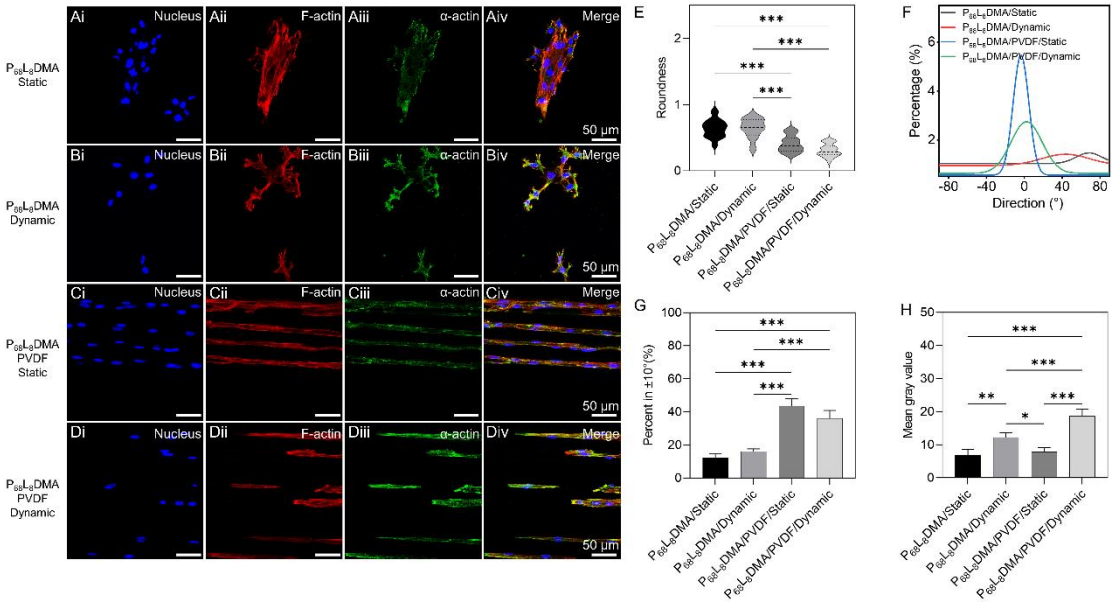

Figure 4-12. α-actinin and F-actin expressions of H9c2 cardiomyoblasts cultured on (A) $P_{68}L_8DMA$ under static culture condition, (B) $P_{68}L_8DMA$ under dynamic culture condition, (C) $P_{68}L_8DMA$/PVDF under static culture condition, and (D) $P_{68}L_8DMA$/PVDF under dynamic culture condition. (E) Quantitative analysis of the nucleus roundness of H9c2 cardiomyoblasts in different groups. (F) Quantitative analysis of the percentage of cells within ±10° of the main direction. (G) Analysis of cell angle distribution in different groups. (H) Quantitative analysis of the fluorescence intensity of α-actinin in different groups. The differences are statistically significant when p values are below 0.05 (*), 0.01 (**), and 0.001 (***).

To assess the effects of topological structure, mechanical and electrical stimuli on cell morphology and cardiac functions, the cytoskeleton, nuclei, and α-actinin were stained (**Figure 4-12**A-D). For cells on $P_{68}L_8DMA$ (**Figure 4-12**Aii-Bii), the cyclic stretching induced F-actin re-organization on $P_{68}L_8DMA$ surface and the cells extended more filamentous pseudopodia, which is important for cell migration. This

suggests that if stretching is prolonged, the cellular cytoskeleton may undergo further reorganization and influence cell orientation. For cells on $P_{68}L_8$DMA/PVDF (**Figure 4-12**Cii-Dii), the cellular morphological changes after cyclic stretching appeared to be not significant, thus further quantitative analysis was required. α-actinin, a cardiac-specific protein, is a structural protein that anchors actin filaments to the Z-discs in the sarcomeres of cardiac muscle cells. Such anchoring allows for proper alignment and organization of the contractile apparatus, enabling efficient contraction and relaxation of the heart. It was expressed in all groups, but its expression is more pronounced in groups $P_{68}L_8$DMA/Dynamic and $P_{68}L_8$DMA/PVDF/Dynamic. Therefore, mechanical and electrical stimulus may contribute to α-actinin expression, which needs further quantitative analysis is needed (**Figure 4-12**Aiii-Diii). The merged views ensure that α-actinin and F-actin do not completely overlap and are expressed in different regions of the cell (**Figure 4-12**Aiv-Div).

To further assess the changes in cell morphology and cardiac functions, the nucleus roundness (**Figure 4-12**E), which reflects cell deformation, angle distribution (**Figure 4-12**F-G), fluorescence intensity of α-actinin (**Figure 4-12**H) were analyzed quantitatively. From **Figure 4-12**E, mechanical stimulus with 5% strain under 1 Hz for 24 h did not influence the nucleus roundness, as there was no significant difference between the static culture and dynamic culture. However, both $P_{68}L_8$DMA/PVDF/Static and $P_{68}L_8$DMA/PVDF/Dynamic groups showed lower roundness than $P_{68}L_8$DMA/Static and $P_{68}L_8$DMA/Dynamic groups, indicating that the

aligned PVDF could induce nuclear elongation and F-actin re-organization along the fiber direction. From **Figure 4-12**F-G, cyclic stretching did not affect cell orientation. The percentage of cells in main direction of $P_{68}L_8$DMA/Static (12.36 ± 1.78%) and $P_{68}L_8$DMA/Dynamic (16.07 ± 1.28%) groups had no difference, and likewise for $P_{68}L_8$DMA/PVDF/Static (43.58 ± 3.48%) and $P_{68}L_8$DMA/PVDF/Dynamic (36.09 ± 3.87%) groups. However, the aligned PVDF fibers could induce cell orientation. From **Figure 4-12**H, mechanical stimulation could enhance α-actinin expression, as $P_{68}L_8$DMA/Dynamic group showed higher α-actinin expression than both $P_{68}L_8$DMA/static and $P_{68}L_8$DMA/PVDF/Static. In addition, PVDF or aligned cell growth did not significantly influence α-actinin expression, as the $P_{68}L_8$DMA/Static and $P_{68}L_8$DMA/PVDF/Static groups showed no difference. Finally, cells in $P_{68}L_8$DMA/PVDF/Dynamic group show the highest α-actinin expression, indicating that not only mechanical stretching but also electrical stimulation caused by PVDF enhance α-actinin expression. The results demonstrate that the PVDF fibers could not only induce the alignment of H9c2 cardiomyoblasts to mimic the natural structure of myocardium. Its piezoelectricity could also facilitate α-actinin expression.

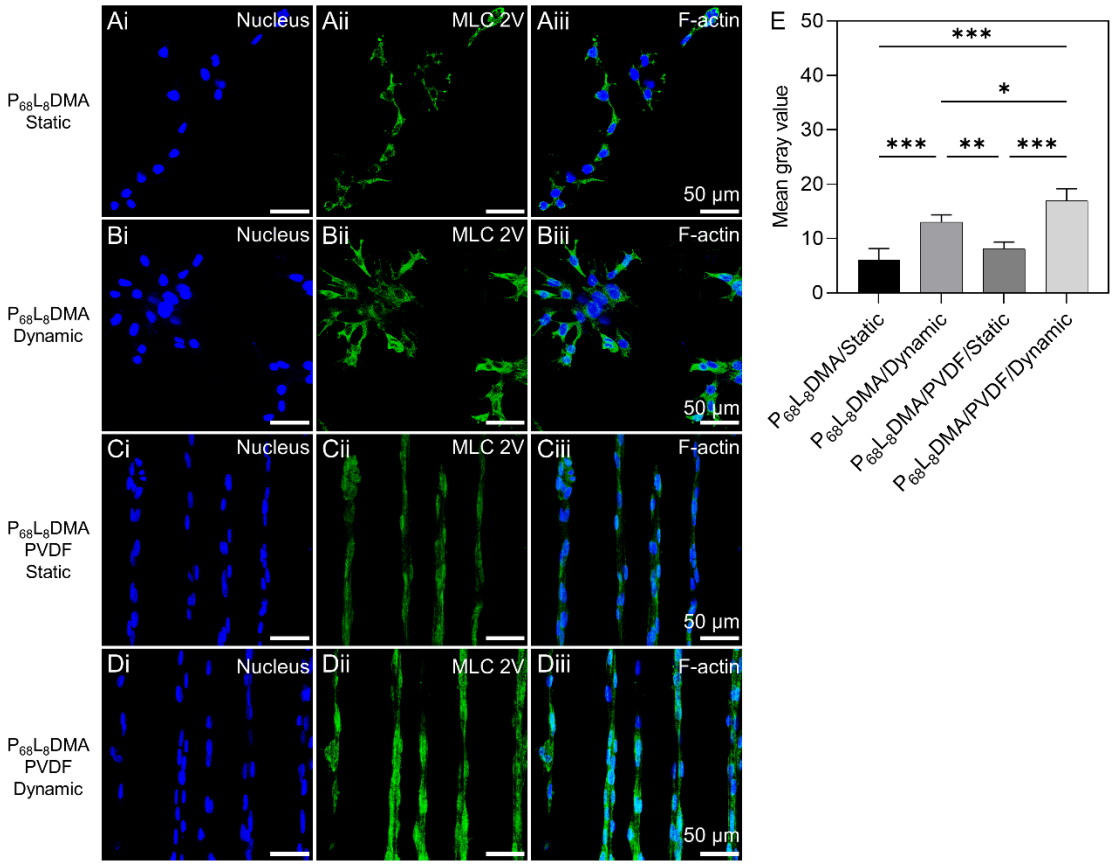

Figure 4-13. MLC-2V expression of H9c2 cardiomyoblasts cultured on (A) $P_{68}L_8$DMA under static culture condition, (B) $P_{68}L_8$DMA under dynamic culture condition, (C) $P_{68}L_8$DMA/PVDF under static culture condition, and (D) $P_{68}L_8$DMA/PVDF under dynamic culture condition. (E) Quantitative analysis of the fluorescence intensity of MLC-2V in different groups. The differences are statistically significant when p values are below 0.05 (*), 0.01 (**), and 0.001 (***).

MLC-2V, another key protein associated with the myosin-heavy chain in the sarcomeres of cardiomyocytes, is involved in the regulation of muscle contraction by modulating myosin motor protein activity. **Figure 4-13** demonstrates MLC-2V expressions of H9c2 cardiomyoblasts in different groups. From the preliminary observation of the images (**Figure 4-13**A-D), it can be seen that $P_{68}L_8$DMA/Dynamic

and $P_{68}L_8$DMA/PVDF/Dynamic groups have higher fluorescence intensity of MLC-2V, indicating that stretching has an effect on the expression of MLC-2V. However, further quantitative analysis is needed to determine the effect of electrical stimulation on the expression of MLC-2V. **Figure 4-13**E shows the quantitative data that $P_{68}L_8$DMA/static and $P_{68}L_8$DMA/PVDF/Static have similar MLC-2V and are significantly lower than $P_{68}L_8$DMA/Dynamic and $P_{68}L_8$DMA/PVDF/Dynamic groups. $P_{68}L_8$DMA/PVDF/Dynamic group has the highest expression of MLC-2V, significantly higher than all other groups. Similar to α-actinin, mechanical stimulation could significantly improve MLC-2V expression while adding PVDF did not have any influence on MLC-2V levels. In addition, $P_{68}L_8$DMA/PVDF/Dynamic had the highest MLC-2V levels, indicating that the generated electrical stimulation under cyclic stretching enhanced MLC-2V expression and the cardiac function of the loaded H9c2 cardiomyoblasts.

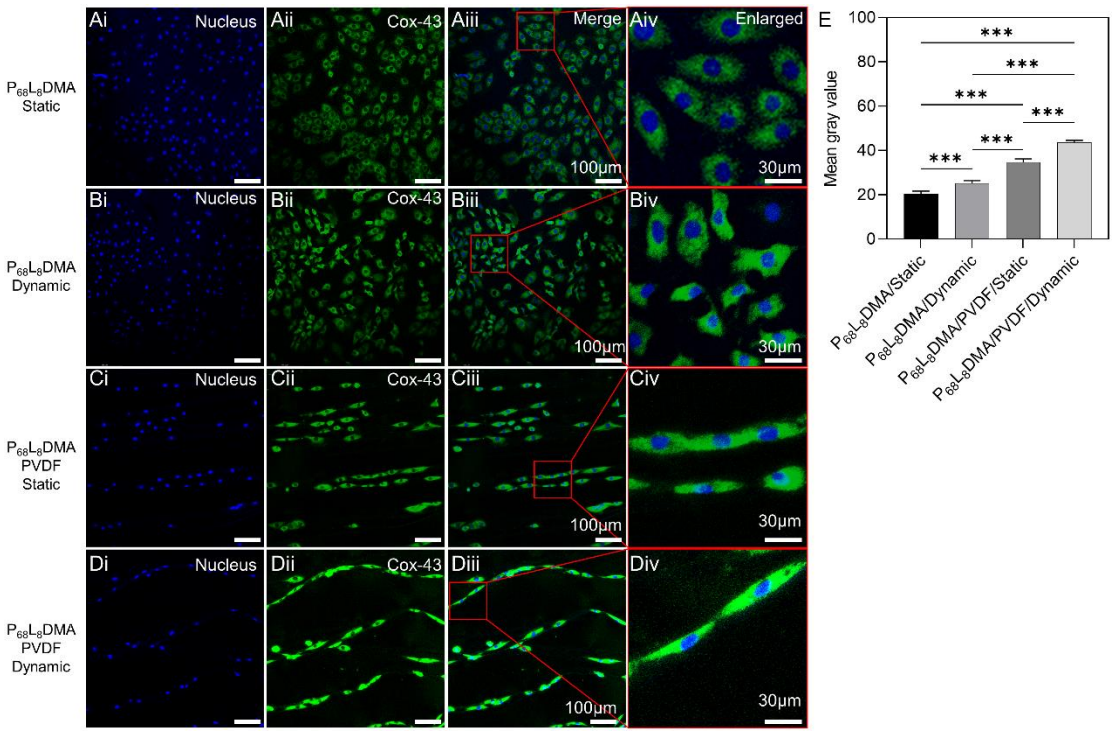

Figure 4-14. COX-43 expression of H9c2 cardiomyoblasts cultured on (A) $P_{68}L_8DMA$ under static culture condition, (B) $P_{68}L_8DMA$ under dynamic culture condition, (C) $P_{68}L_8DMA$/PVDF under static culture condition, and (D) $P_{68}L_8DMA$/PVDF under dynamic culture condition. (E) Quantitative analysis of the fluorescence intensity of COX-43 in different groups. The differences are statistically significant when p values are below 0.001 (***).

In cardiac tissue, COX-43 forms gap junctions between cardiomyocytes, allowing for the rapid propagation of electrical impulses that coordinate the contraction of the heart. These gap junction channels facilitate the synchronized contraction of cardiac muscle cells, ensuring efficient pumping of blood. From the preliminary observation of the images (**Figure 4-14**A-D), it can be seen that $P_{68}L_8DMA$/PVDF/Dynamic has the highest fluorescence intensity of COX-43 followed by $P_{68}L_8DMA$/PVDF/Static. From

the quantitative data (**Figure 4-14**E), cells cultured on $P_{68}L_8$DMA/PVDF expressed more COX-43 protein than cells cultured on $P_{68}L_8$DMA, indicating that cell alignment influences the formation of gap junctions. Stretching also enhanced the COX-43 expression according to the contrast between $P_{68}L_8$DMA/Static and $P_{68}L_8$DMA/Dynamic. Cells in $P_{68}L_8$DMA/PVDF/Dynamic show the highest COX-43 expression due to a synergistic effect of cell alignment, mechanical stimulation, and electrical stimulation.

4.3.7 *In vivo* therapeutic effect of the cardiac patch in rabbit model of acute MI

To investigate the *in vivo* effect of the cardiac patch, rabbit model of acute MI was used. Compared with rat models, rabbits more closely resemble humans in terms of electrophysiological properties, mechanical properties, coronary architecture, and cardiac responses to ischemia. In addition, rabbits are bigger than mice, making it much easier to perform experimental procedures such as sample implantation, cannulation of certain blood vessels, and implantation of external devices (e.g., ECG recorders).[191, 192]

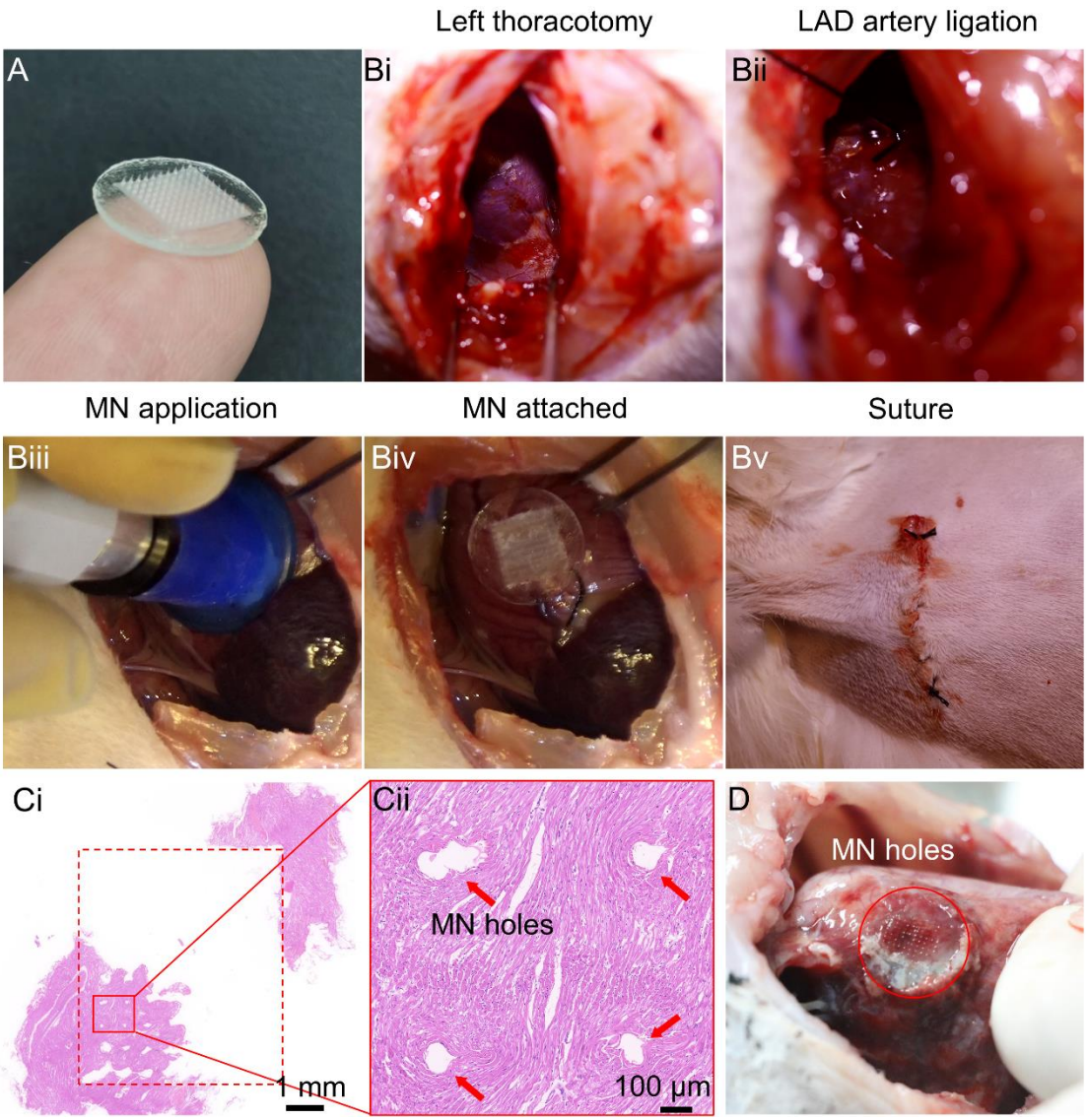

Figure 4-15. *In vivo* implantation of the cardiac patch in a rabbit model. (A) General appearance of the cardiac patch. (Bi)-(Bv) Implantation process of the cardiac patch. (Ci) H&E-stained longitudinal section of cardiac tissue showing the microneedle holes. Red dotted line indicates the area where microneedles interacted with the cardiac tissue. (Cii) Enlarged view showing the distribution of the microneedle holes in the cardiac tissue. Red arrows indicate the microneedle holes. (D) Microneedle holes on the heart surface created by cardiac patch after 7 days of implantation.

As shown in **Figure 4-15**A, to prevent easy detachment during *in vivo* implantation, the cardiac patch was designed with only a central square region containing the needle tip and fibers. The surrounding $P_{68}L_8$DMA surface, whose adhesive property has been shown in Chapter 3, can provide additional adhesive support. **Figure 4-15**Bi-Bv demonstrate the implantation process of the cardiac patch, including left thoracotomy, LAD artery ligation, microneedle application, and suture. **Figure 4-15**C is the H&E staining image of cardiac tissues after microneedle insertion on Day 1. The cardiac patch created an array of holes within a square region (marked by red dotted line, **Figure 4-15**Ci), confirming the successful insertion of the needle tips. From the enlarged view (**Figure 4-15**Cii), there was no obvious inflammatory cell aggregation around the holes, indicating good biocompatibility of the cardiac patch. **Figure 4-15**D also shows the microneedle holes created on the heart surface after 7 days of implantation, which further confirmed successful insertion.

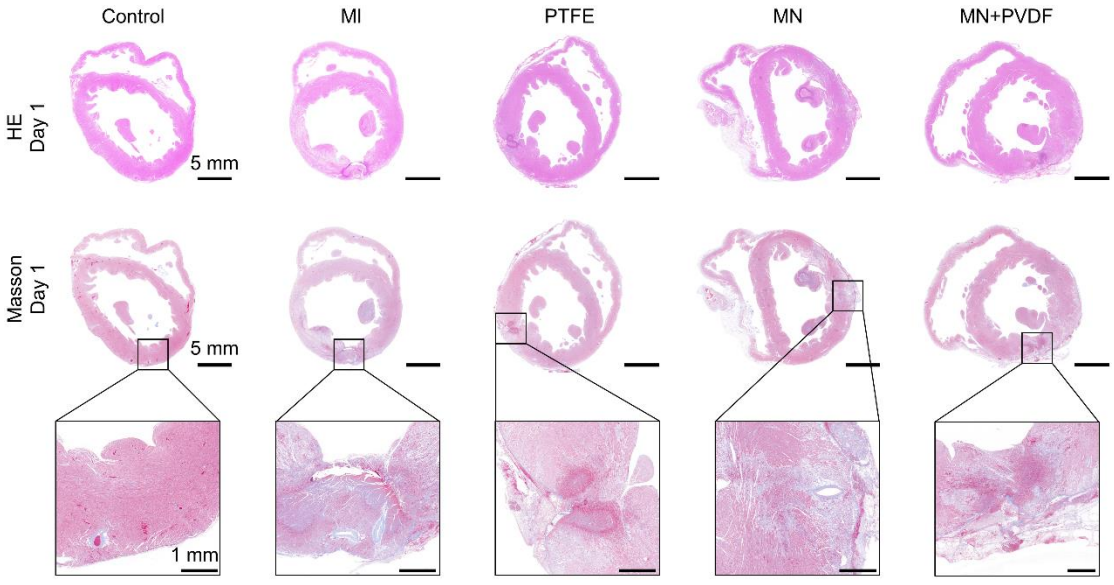

Figure 4-16. Representative images of H&E and Masson's trichrome-stained cardiac

tissue sections 1 day after MI in different groups, including control, MI, PTFE, microneedle (MN), and MN+PVDF. Blue, scar tissue; red, viable myocardium; snapshots, enlarged view of the black box area.

To further clarify how the microneedles and PVDF fibers affected heart morphology and fibrosis, H&E and Masson's trichrome staining of heart tissue sections on days 1, 7, and 28 were used. On day 1 after treatment (**Figure 4-16**), compared with the normal tissue (Control), the other four groups all showed initial fibrosis in the ligation area but no obvious change in the left ventricular wall thickness.

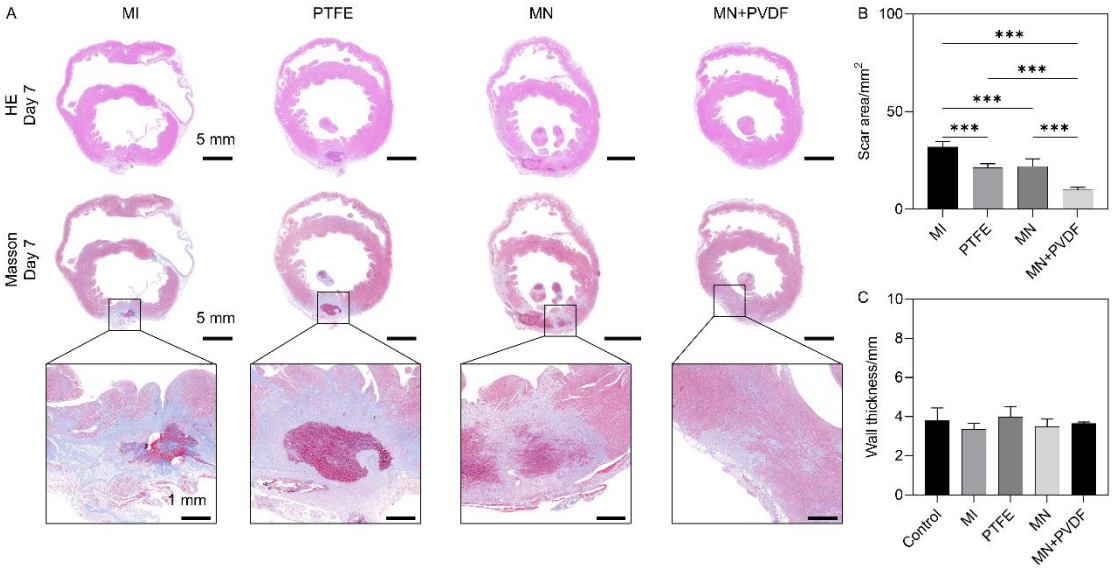

Figure 4-17. (A) Representative images of H&E and Masson's trichrome-stained cardiac tissue sections 7 days after MI in different groups, including MI, PTFE, MN, and MN+PVDF. Blue, scar tissue; red, viable myocardium; snapshots, enlarged view of the black box area. Quantitative analysis of (B) the scar area and (C) left ventricular wall thickness 7 days after MI. The differences are statistically significant

when p values are below 0.001 (***).

Figure 4-17A shows the general morphology of heart sections from different groups after 7 days, as stained with H&E and Masson's trichrome. From the images, it is evident that the MI group exhibits significant scar tissue formation, accompanied by severe fat infiltration (top-right area in the tissue section).[193] The PTFE and MN groups also show large areas of scar tissue. In contrast, the MN+PVDF group only shows minimal fibrosis in the ligated area. From the quantitative analysis (**Figure 4-17**B), the healthy myocardium in the ligation area was replaced by collagenous scar tissue in MI (31.97 ± 2.36 mm^2), PTFE (21.25 ± 1.75 mm^2), and MN (22 ± 3.36 mm^2). PTFE and MN groups showed similar performance and significantly reduced the scar formation compared with MI, proving that the mechanical support provided by these patches could alleviate fibrosis. MN+PVDF group only had a scar area of 9.92 ± 1.13 mm^2, which was significantly lower than other groups, indicating potential enhancement of cardiac function by electrical stimulation of the PVDF fibers. Meanwhile, all groups showed no obvious thinning of the left ventricular wall compared with normal tissue (**Figure 4-17**C), indicating that the MI in all groups were still in the early stage.

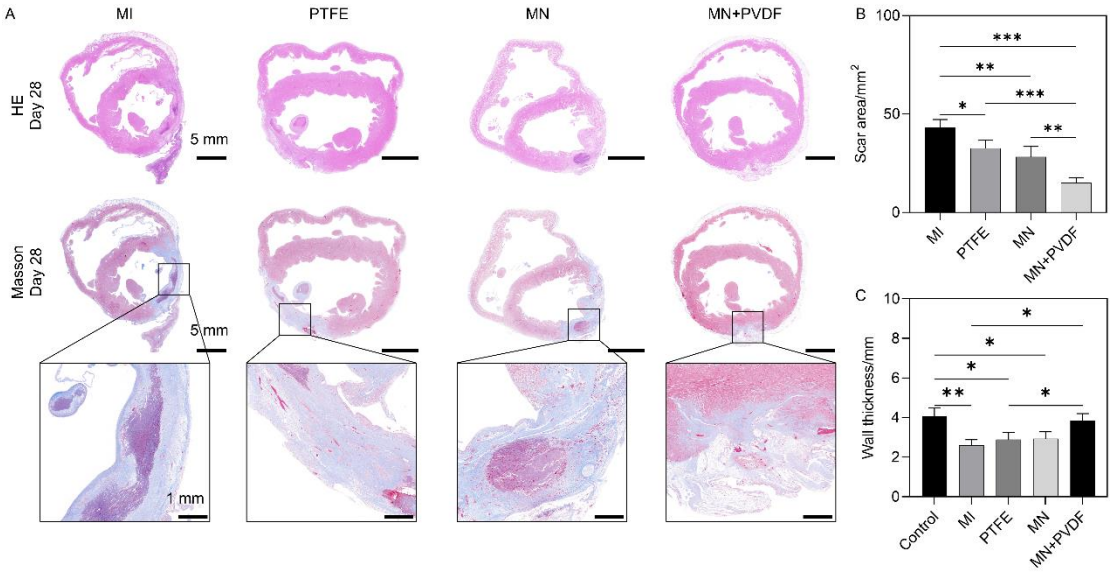

Figure 4-18. (A) Representative images of H&E and Masson's trichrome-stained cardiac tissue sections 28 days after MI in different groups, including MI, PTFE, MN, and MN+PVDF. Blue, scar tissue; red, viable myocardium; snapshots, enlarged view of the black box area. Quantitative analysis of (B) the scar area and (C) left ventricular wall thickness 28 days after MI. The differences are statistically significant when p values are below 0.05 (*), 0.01 (**), and 0.001 (***).

After 28 days of treatment, cardiac fibrosis was further exacerbated in different groups (**Figure 4-18**A). The MI group exhibits the most severe myocardial fibrosis accompanied by some degree of ventricular wall atrophy, followed by the PTFE and MN groups. The MN+PVDF group, on the other hand, still shows a small area of fibrosis. **Figure 4-18**B shows specific values with a scar area of 43.12 ± 3.54 mm^2 in MI group, 32.65 ± 3.6 mm^2 in PTFE group, 28.35 ± 4.58 mm^2 in MN group, and 14.94 ± 2.28 mm^2 in MN+PVDF group. In addition, from **Figure 4-18**C, MI (2.60 ± 0.23 mm), PTFE (2.89 ± 0.29 mm), and MN (2.93 ± 0.29 mm) showed significant

thinning of the left ventricle wall compared with normal tissue (4.07 ± 0.30 mm) and MN+PVDF (3.85 ± 0.29 mm). Such thinning phenomenon is known as ventricular remodeling with necrosis of cardiac tissues,[194, 195] which would result in expansion of the ventricular chamber, impairment of contractile function, and increase of mechanical stress on the ventricular wall. Therefore, the MN+PVDF group slowed down ventricular remodeling by a combination of mechanical and electrical stimulations.

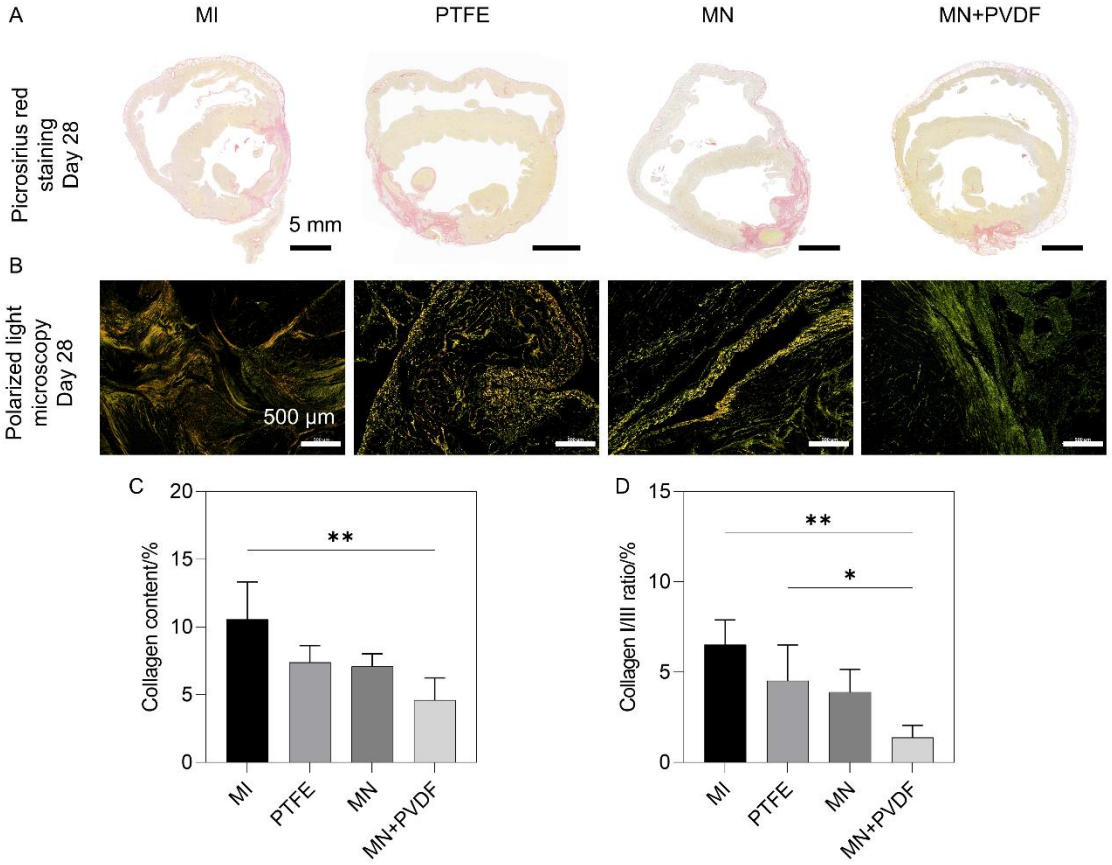

Figure 4-19. Collagen content analysis of cardiac tissue sections 28 days after MI in different groups. (A) Identification of collagens via picrosirius red staining among the four groups, including MI, PTFE, MN, and MN+PVDF. Red and pink, collagen; yellow and brown, muscle fibers. (B) Representative polarized light images of the

picrosirius red-stained sections among the four groups. Yellow and brown, collagen I; Green, collagen III. (C) Quantitative analysis of collagen content. (D) Quantitative analysis of collagen I/III ratio. The differences are statistically significant when p values are below 0.05 (*) and 0.01 (**).

Picrosirius red staining (**Figure 4-19**A) and polarization microscopy (**Figure 4-19**B) were employed to assess collagen fiber content and composition within the scar tissues in different groups on day 28. The total collagen content was calculated by ratio of the collagen area (red and pink) and the whole tissue area (collagen plus yellow and brown areas). From **Figure 4-19**C, only MI (10.58 ± 2.38%) and MN+PVDF (4.61 ± 1.07%) showed significant difference to each other. PTFE (7.39 ± 1.07%) and MN (7.11 ± 0.79%) had similar collagen deposition, both showing no obvious distinction from MI. Furthermore, collagen I was marked by yellow and brown staining while collagen III was identified by green staining under polarized light. Collagen III provides elasticity and enhances flexibility, which may enhance the heart function. From **Figure 4-19**D, collagen I/III ratio was the highest in MI and PTFE (6.52 ± 1.19% and 4.53 ± 1.71%); the ratio in MN (3.89 ± 1.10%) was slightly lower but such difference was not statistically significant. MN+PVDF had the lowest ratio (1.38 ± 0.59%) and it was significantly lower than those of MI and PTFE groups. In general, significant decrease in collagen deposition and collagen I/III ratio were observed in MN+PVDF group, showing the benefits of microneedles combined with PVDF fibers in reducing scar area and modifying the composition of collagen in the

infarct area (mainly elevating the collagen III ratio).

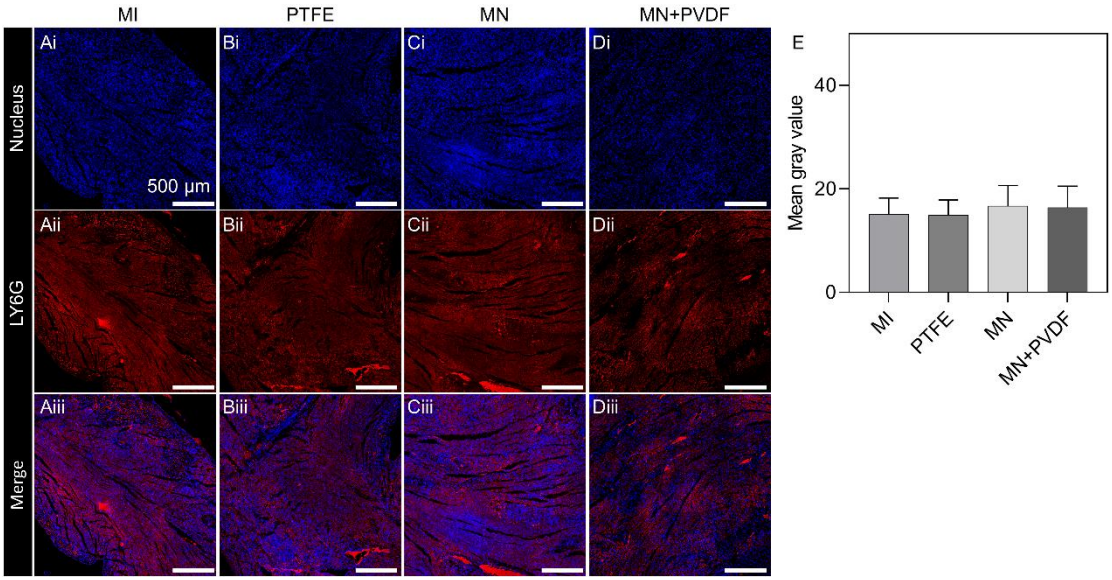

Figure 4-20. Representative fluorescence images showing LY6G expression in cardiac tissue sections 1 day after MI in (A) MI, (B) PTFE, (C) MN, and (D) MN+PVDF groups. Blue, nucleus; red, LY6G. (E) Quantitative analysis of the fluorescence intensity of LY6G among four groups.

Then, immunostaining (LY6G, α-SMA, and TUNEL) of tissue sections was used to assess cardiac regeneration . **Figure 4-20** demonstrates LY6G expression as the marker of macrophages and neutrophils.

As shown in **Figure 4-20**A-D, immune cells are uniformly distributed and present in similar numbers in the ligated areas (infarct areas) of all groups. This indicates that immune cells infiltrate the myocardium after arterial ligation. Treatment with PTFE, MN, and MN+PVDF did not result in increased infiltration of immune cells. From

quantitative analysis (**Figure 4-20**E), LY6G expression was indistinguishable among all groups, and there was no elevated infiltrations or aggregation of inflammatory cells in the heart treated with MN or MN+PVDF. Hence, the microneedle patch had good biocompatibility and their insertion did not cause serious foreign body reaction.

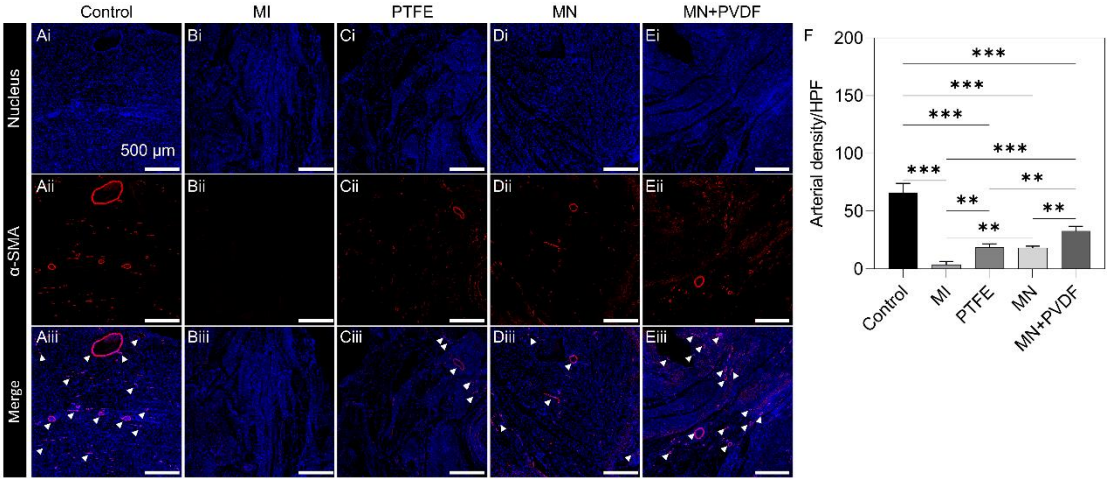

Figure 4-21. Representative fluorescence images showing α-SMA expression in cardiac tissue sections 28 day after MI in (A) Control, (B) MI, (C) PTFE, (D) MN, and (E) MN+PVDF groups. Blue, nucleus; red, α-SMA. (F) Quantitative analysis of arterial density among five groups. White triangles indicate the vessels. The differences are statistically significant when p values are below 0.01 (**) and 0.001 (***).

Electrical stimulation can enhance the induction of angiogenesis.[196, 197] To investigate vessel formation in the infarcted region, tissue sections were stained for α-SMA to mark the vascular smooth muscle cells, and the red circular cavities were identified as vessels (**Figure 4-21**A-E). The arterial density was assessed based on α-

SMA$^+$ vessels per HPF using samples collected on day 28 (**Figure 4-21**F). Naturally, the control group had the highest arterial density (66 ± 7 per HPF) since it had no induced MI, while the MI group had the lowest density (3.75 ± 2.38 per HPF) due to no treatment. The values in PTFE group (18.75 ± 2.59 per HPF) and MN group (18.25 ± 1.40 per HPF) showed no significant difference, and significantly higher than that in MI group but lower than that in MN+PVDF group (32.75 ± 3.56 per HPF). With the mechanical support of PTFE membrane and microneedle patches, vessels in the tissue might not undergo rapid necrosis. Assisted by electrical stimulation of PVDF fibers, the arterial density was markedly elevated. Hence, the combined therapy of mechanical and electrical stimulations could alleviate angionecrosis and facilitate angiogenesis to a certain degree.

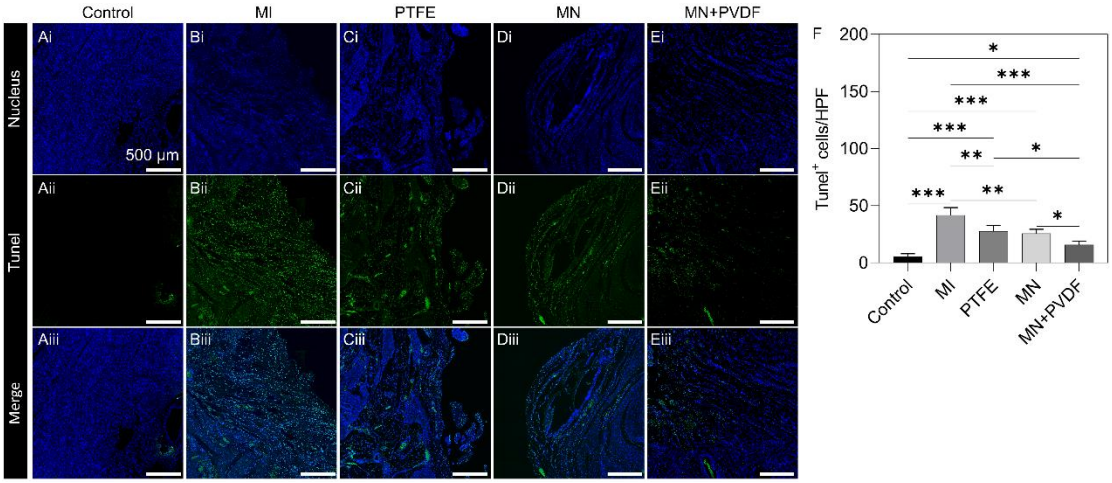

Figure 4-22. Representative fluorescence images showing the presence of TUNEL$^+$ apoptotic cells (green) in cardiac tissue sections 28 days after MI in (A) Control, (B) MI, (C) PTFE, (D) MN, and (E) MN+PVDF. (F) Quantitative analysis of TUNEL$^+$ apoptotic cell numbers among the five groups. The differences are statistically

significant when p values are below 0.05 (*), 0.01 (**), and 0.001 (***).

Finally, apoptosis in the infarcted area was evaluated by counting $TUNEL^+$ cells per HPF, as shown in **Figure 4-22**. From the quantitative analysis (**Figure 4-22**F), MI group had the most $TUNEL^+$ cells per HPF of 41.75 ± 5.72. The value in PTFE group (27.75 ± 4.44 per HPF) was almost identical to that in MN group (25.75 ± 3.19 per HPF). However, MN+PVDF group had significantly fewer $TUNEL^+$ cells (15.75 ± 2.86 per HPF). The mechanical support was crucial to reduce apoptosis, and electrical stimulation could further alleviate necrocytosis, slowing down the deterioration of MI.

4.4 Summary

In conclusion, we designed a self-powered cardiac patch integrated with microneedles and aligned piezoelectric PVDF microfibers for cardiac tissue regeneration. The needle tip of the microneedle was made of stiff P_7L_2DMA for tissue anchoring while the backing layer was made of elastic $P_{68}L_8$DMA to withstand long-term cyclic stretching. The aligned PVDF fibers were fabricated by EHD printing and attached on the $P_{68}L_8$DMA backing layer. Once the microneedles were inserted into the cardiac tissue and deformed with the heartbeats, the aligned PVDF fibers could generate electrical stimulation and provide topological induction for cell growth.

The EHD-printed PVDF fibers exhibited good current output under cyclic stretching. The $P_{68}L_8$DMA backing layer also showed great fatigue properties to withstand long-

term cyclic stretching without breaking under 20% strain. From the *in vitro* cell experiment, the aligned PVDF fibers could induce the oriented growth of H9c2 cardiomyoblasts. Under dynamic cell culture, the electrical stimulation caused by PVDF fibers significantly enhanced cardiac functional protein (α-actinin, MLC-2V, COX-43) expressions in H9c2 cardiomyoblasts and elongated cell morphology. From the *in vivo* experiment using rabbit MI model, the mechanical support of the microneedle patch and the electrical stimulation generated by the PVDF fibers could reduce fibrosis and avoid ventricular remodeling. In addition, collagen composition (Collagen I/III ratio) in the infarcted region was modified by the cardiac patch to have a higher Collagen III proportion, which was better for cardiac function. Moreover, implantation of the cardiac patch did not cause obvious inflammation but significantly promoted angiogenesis and reduced apoptosis in the infarcted area.

As a result, the proposed self-powered cardiac patch offers a simple and effective approach for treating myocardial infarction. In the future, when combined with drug delivery, it holds great potential for significantly enhancing the therapeutic efficacy of clinical myocardial infarction treatment.

Chapter 5 Conclusions and recommendations for future work

5.1 Major findings and conclusion

In the first study, a P_7L_2DMA/GelMA core-shell microneedle patch with mangiferin loaded in the shell and hMSC-derived exosomes loaded in the core were fabricated for scarless skin wound healing. The GelMA shell provided a swelling interface for tissue interlocking and rapidly released magniferin at early wound healing stage for anti-inflammation. Meanwhile, the P_7L_2DMA core offered long-term encapsulation and release of exosomes (30% release in 3 weeks), sustainably promoting angiogenesis and suppressing inflammation. The differential drug release led to *in vivo* suppression of pro-inflammatory cytokine TNF-α and enhancement of anti-inflammatory cytokine IL-10, enhanced cell migration and tube formation of HUVECs *in vitro*, and neovascularization with markers of the NF-κB signaling pathway (α-SMA, TGF-β, CTGF, Col I) *in vivo*. Altogether, our core-shell microneedles not only realized scarless skin regeneration by exploiting the release properties of the materials, but also demonstrated for the first time prolonged encapsulation and release of therapeutic exosomes from hydrogel. This provides an important guideline for future biomaterial studies taking advantage of the long-term benefits of exosome treatments, especially using hydrogel microneedles, for multi-phase tissue regeneration.

In the second project featured a contractile microneedle anti-scar patch to

simultaneously eliminate tension forces from the surrounding tissue during early wound healing and release the wound contraction force generated by fibroblasts during late-stage healing. The whole system consisted of three parts: the backing layer, the middle part, and the tilted part. The backing layer was made of $P_{68}L_8$DMA, which was flexible and elastic enough to generate contractile force to resist tension force from the surrounding tissue. The middle part was made of P_7L_2DMA, which was stiffer to insert into the wound bed for releasing the local stress generated by myofibroblasts. The tilted part was also made of P_7L_2DMA used to insert into the surrounding tissue for tissue adhesion and force transduction. The contractile microneedle patch showed better tissue adhesion than pure backing layer and common microneedle patches. Using a fibroblast-loaded collagen system as an *in vitro* scar model, the proposed microneedle system significantly reduced some scar-related protein (α-SMA, CXCL 14) expressions. A macrophage-loaded collagen system was also established *in vitro* to show that the proposed microneedle system reduced the expressions of some inflammatory proteins (iNOS, TNF-α) but enhanced the anti-inflammatory protein (IL-10) expression. This project is also the first to introduce tension force and inflammatory cells in the *in vitro* scar model when investigating the effects of microneedles on scar formation. RNA sequencing revealed that our patch could decrease the scar formation by down-regulating some mechanical signaling pathways, including focal adhesion, ECM-receptor interaction, and PI3K signaling pathway.

In the third project, we developed a self-powered cardiac patch integrated with microneedle and aligned PVDF microfibers to achieve piezoelectric therapy for myocardial infarction. The microneedle tips were made of stiff P_7L_2DMA for tissue anchoring while the backing layer was made of elastic $P_{68}L_8$DMA to withstand long-term cyclic stretching. The aligned PVDF fibers were fabricated by EHD printing and attached on the $P_{68}L_8$DMA backing layer. Once the microneedles were inserted into the cardiac tissue and deformed with the heartbeats, the aligned PVDF fibers could generate electrical stimulation and provide topological induction for cell growth. The EHD-printed PVDF fibers exhibited good current output under cyclic stretching. The $P_{68}L_8$DMA backing layer also showed great fatigue properties to withstand long-term cyclic stretching without breaking under 20% strain. From the *in vitro* cell experiment, the aligned PVDF fibers could induce the oriented growth of H9c2 cardiomyocytes. Under dynamic cell culture, the electrical stimulation caused by the PVDF fibers significantly enhanced the cardiac functional protein (α-actinin, MLC-2V, COX-43) expressions and elongated the cell morphology. From the rabbit MI model, the mechanical support of the microneedle patch and electrical stimulation generated by the PVDF fibers could remarkably reduce fibrosis and avoid ventricular remodeling. In addition, collagen composition (Collagen I/III ratio) in the infarcted region was modified by the cardiac patch to have a higher Collagen III proportion, which was better for cardiac function. Moreover, the cardiac patch did not cause obvious inflammation but significantly promoted angiogenesis and reduced apoptosis in the infarcted area.

5.2 Recommendations for future work

There are still many aspects that need further exploration for the work presented in this thesis.

For the first project, the double-layer microneedles that can load and release two different drugs is not only applicable to skin repair but also in other tissues that require long-term healing, such as tendons and cartilage. Additionally, to further validate the functionality of this microneedle system in scar prevention and skin repair, animal models with a higher likelihood of scarring, such as rabbit ears or pigs, need to be adopted. Furthermore, extending the observation period to over 14 days would enhance comprehension of the sustained release capabilities of the microneedles and their impact on tissue healing and scar formation. For clinical translation, we think the focus is on how to stabilize the manufacturing process of the core-shell structured microneedles to enable mass production, as the dehydration process of the hydrogel is not very stable.

For the second project, although the efficacy of the contractile microneedle patch has been demonstrated in an *in vitro* scar model, further animal experiments are necessary. For example, validating its anti-scar effects in rabbit ear scar models or pig models would be beneficial. Additionally, finite element simulations are essential to investigate the changes in stress distribution in the model after patch insertion. This

would provide a more intuitive demonstration of the stress release function of the microneedles and the stress concentration at the microneedle-tissue boundary where tension force exists, thus better correlating with the immunofluorescence results. Furthermore, the *in vitro* scar models can benefit from more cell types as real wounds often involve interactions between multiple cell types, which would contribute to a deeper understanding of scar formation under stress. For clinical translation, we believe the key aspect is to ensure that the force applied by the patch during use is consistent, which requires the development of appropriate auxiliary equipment.

For the third project, finite element simulations are also necessary to analyze the changes in stress in the heart tissue when the microneedles are inserted. This would provide a better understanding of the stress distribution in the infarcted area and the stress changes in the microneedles during deformation. These simulations would be valuable for material selection and system design for cardiac patches. In addition, when validating the efficacy of the cardiac patch *in vitro*, it would be better to use cells that are more representative of human cardiomyocytes, such as HL-1 cells, primary cardiac cells, or iPSC-derived cardiac cells. These cells exhibit more pronounced contraction and electrical conduction, providing more comprehensive data. In animal experiments, data such as echocardiography and electrocardiography can also reflect cardiac function and hence should be included to validate the cardiac patch more comprehensively. For clinical translation, we think the main challenge lies in the significant trauma caused by the transplantation process. In the future, it is

hoped that further development of minimally invasive transplantation based on the cardiac patch can be achieved, along with the incorporation of more drug factors to enhance its effectiveness in treating myocardial infarction.

References

[1] V. Perez-Puyana, M. Jiménez-Rosado, A. Romero, A. Guerrero, Polymer-based scaffolds for soft-tissue engineering, Polymers 12(7) (2020) 1566.
[2] H.S. Kim, X. Sun, J.-H. Lee, H.-W. Kim, X. Fu, K.W.J.A.d.d.r. Leong, Advanced drug delivery systems and artificial skin grafts for skin wound healing, 146 (2019) 209-239.
[3] D. Chouhan, N. Dey, N. Bhardwaj, B.B. Mandal, Emerging and innovative approaches for wound healing and skin regeneration: current status and advances, Biomaterials 216 (2019) 119267.
[4] A.L. Moore, C.D. Marshall, L.A. Barnes, M.P. Murphy, R.C. Ransom, M.T. Longaker, Scarless wound healing: Transitioning from fetal research to regenerative healing, WIREs Dev. Biol. 7(2) (2018) e309.
[5] B.J. Larson, M.T. Longaker, H.P. Lorenz, Scarless Fetal Wound Healing: A Basic Science Review, Plastic and Reconstructive Surgery 126(4) (2010) 1172-1180.
[6] Neutrophils and Wound Repair: Positive Actions and Negative Reactions, Adv. Wound Care 2(7) (2013) 379-388.
[7] M. Walraven, W. Talhout, R.H.J. Beelen, M. van Egmond, M.M.W. Ulrich, Healthy human second-trimester fetal skin is deficient in leukocytes and associated homing chemokines, Wound Repair Regen. 24(3) (2016) 533-541.
[8] G.G. Walmsley, Z.N. Maan, V.W. Wong, D. Duscher, M.S. Hu, E.R. Zielins, T. Wearda, E. Muhonen, A. McArdle, R. Tevlin, D.A. Atashroo, K. Senarath-Yapa, H.P. Lorenz, G.C. Gurtner, M.T. Longaker, Scarless Wound Healing: Chasing the Holy Grail, Plastic and Reconstructive Surgery 135(3) (2015) 907-917.
[9] J. Kim, P. Hematti, Mesenchymal stem cell–educated macrophages: A novel type of alternatively activated macrophages, Exp. Hematol. 37(12) (2009) 1445-1453.
[10] S. Mascharak, H.E. desJardins-Park, M.F. Davitt, M. Griffin, M.R. Borrelli, A.L. Moore, K. Chen, B. Duoto, M. Chinta, D.S. Foster, A.H. Shen, M. Januszyk, S.H. Kwon, G. Wernig, D.C. Wan, H.P. Lorenz, G.C. Gurtner, M.T. Longaker, Preventing Engrailed-1 activation in fibroblasts yields wound regeneration without scarring, Science 372(6540) (2021) eaba2374.
[11] X. Zhang, Y. Wang, J. Chi, Y. Zhao, Smart Microneedles for Therapy and Diagnosis, Research 2020 (2020)
[12] J. Lee, D.-H. Kim, K.J. Lee, I.H. Seo, S.H. Park, E.H. Jang, Y. Park, Y.-N. Youn, W. Ryu, Transfer-molded wrappable microneedle meshes for perivascular drug delivery, J. Controlled Release 268 (2017) 237-246.

[13] L. Barnum, M. Samandari, T.A. Schmidt, A. Tamayol, Microneedle arrays for the treatment of chronic wounds, Expert Opin. Drug Deliv. 17(12) (2020) 1767-1780.
[14] J. Tang, J. Wang, K. Huang, Y. Ye, T. Su, L. Qiao, M.T. Hensley, T.G. Caranasos, J. Zhang, Z. Gu, K. Cheng, Cardiac cell–integrated microneedle patch for treating myocardial infarction, Sci. Adv. 4(11) (2018) eaat9365.
[15] W. Yao, C. Tao, J. Zou, H. Zheng, J. Zhu, Z. Zhu, J. Zhu, L. Liu, F. Li, X. Song, Flexible two-layer dissolving and safing microneedle transdermal of neurotoxin: A biocomfortable attempt to treat Rheumatoid Arthritis, Int. J. Pharm. 563 (2019) 91-100.
[16] Z. Yao, T. Xue, C. Cai, J. Li, M. Lu, X. Liu, T. Jin, F. Wu, S. Liu, C. Fan, Parathyroid Hormone - Loaded Microneedle Promotes Tendon Healing Through Activation of mTOR, Adv. Therap. 3(8) (2020) 2000025.
[17] A. Than, C. Liu, H. Chang, P.K. Duong, C.M.G. Cheung, C. Xu, X. Wang, P. Chen, Self-implantable double-layered micro-drug-reservoirs for efficient and controlled ocular drug delivery, Nat. Commun. 9(1) (2018) 1-12.
[18] L. Huang, H. Fang, T. Zhang, B. Hu, S. Liu, F. Lv, Z. Zeng, H. Liu, W. Zhou, X. Wang, Drug-loaded balloon with built-in NIR controlled tip-separable microneedles for long-effective arteriosclerosis treatment, Bioact. Mater. 23 (2023) 526-538.
[19] X. Zhang, M.M. Hasani-Sadrabadi, J. Zarubova, E. Dashtimighadam, R. Haghniaz, A. Khademhosseini, M.J. Butte, A. Moshaverinia, T. Aghaloo, S. Li, Immunomodulatory microneedle patch for periodontal tissue regeneration, Matter 5(2) (2022) 666-682.
[20] G. Yang, Q. Chen, D. Wen, Z. Chen, J. Wang, G. Chen, Z. Wang, X. Zhang, Y. Zhang, Q. Hu, L. Zhang, Z. Gu, A Therapeutic Microneedle Patch Made from Hair-Derived Keratin for Promoting Hair Regrowth, ACS Nano 13(4) (2019) 4354-4360.
[21] M. Han, H. Yang, X. Lu, Y. Li, Z. Liu, F. Li, Z. Shang, X. Wang, X. Li, J. Li, H. Liu, T. Xin, Three-Dimensional-Cultured MSC-Derived Exosome-Hydrogel Hybrid Microneedle Array Patch for Spinal Cord Repair, Nano Lett. 22(15) (2022) 6391-6401.
[22] S. Li, Y. Li, F. Yu, N. Li, C. Liu, J. Mao, H. Sun, Y. Hu, Y. Zhu, M. Zhou, L. Ding, Human Endometrium-Derived Adventitial Cell Spheroid-Loaded Antimicrobial Microneedles for Uterine Regeneration, Small 18(31) (2022) 2201225.
[23] K.-H. Busch, A. Aliu, N. Walezko, M. Aust, Medical Needling: Effect on Skin Erythema of Hypertrophic Burn Scars, Cureus 10(9) (2018) e3260.
[24] M.C. Aust, K. Reimers, H.M. Kaplan, F. Stahl, C. Repenning, T. Scheper, S. Jahn, N. Schwaiger, R. Ipaktchi, J. Redeker, M.A. Altintas, P.M. Vogt, Percutaneous collagen induction–regeneration in place of cicatrisation?, Journal of Plastic, Reconstructive & Aesthetic Surgery 64(1) (2011) 97-107.
[25] Q. Zhang, L. Shi, H. He, X. Liu, Y. Huang, D. Xu, M. Yao, N. Zhang, Y. Guo, Y. Lu, H. Li, J. Zhou, J. Tan, M. Xing, G. Luo, Down-Regulating Scar Formation by Microneedles Directly via a Mechanical Communication Pathway, ACS Nano 16(7) (2022) 10163-10178.
[26] R. Jamaledin, C.K.Y. Yiu, E.N. Zare, L.-N. Niu, R. Vecchione, G. Chen, Z. Gu, F.R. Tay, P. Makvandi, Advances in Antimicrobial Microneedle Patches for

Combating Infections, Adv. Mater. 32(33) (2020) 2002129.
[27] K. Tsioris, W.K. Raja, E.M. Pritchard, B. Panilaitis, D.L. Kaplan, F.G. Omenetto, Fabrication of Silk Microneedles for Controlled-Release Drug Delivery, Adv. Funct. Mater. 22(2) (2012) 330-335.
[28] B. Gao, M. Guo, K. Lyu, T. Chu, B. He, Intelligent Silk Fibroin Based Microneedle Dressing (i-SMD), Adv. Funct. Mater. 31(3) (2021) 2006839.
[29] M. Wang, Y. Han, X. Yu, L. Liang, H. Chang, D.C. Yeo, C. Wiraja, M.L. Wee, L. Liu, X. Liu, C. Xu, Upconversion Nanoparticle Powered Microneedle Patches for Transdermal Delivery of siRNA, Adv. Healthc. Mater. 9(2) (2020) 1900635.
[30] Y. Chen, Y. Yang, Y. Xian, P. Singh, J. Feng, S. Cui, A. Carrier, K. Oakes, T. Luan, X. Zhang, Multifunctional graphene-oxide-reinforced dissolvable polymeric microneedles for transdermal drug delivery, ACS Appl. Mater. Interfaces 12(1) (2019) 352-360.
[31] H. Chang, S.W. Chew, M. Zheng, D.C.S. Lio, C. Wiraja, Y. Mei, X. Ning, M. Cui, A. Than, P. Shi, Cryomicroneedles for transdermal cell delivery, Nat. Biomed. Eng. (2021) 1-11.
[32] K. Lee, Y. Xue, J. Lee, H.J. Kim, Y. Liu, P. Tebon, E. Sarikhani, W. Sun, S. Zhang, R. Haghniaz, A patch of detachable hybrid microneedle depot for localized delivery of mesenchymal stem cells in regeneration therapy, Adv. Funct. Mater. 30(23) (2020) 2000086.
[33] R. Dong, B.J.N.T. Guo, Smart wound dressings for wound healing, 41 (2021) 101290.
[34] A. Ullah, H. Khan, H.J. Choi, G.M. Kim, Smart microneedles with porous polymer coatings for pH-responsive drug delivery, Polymers 11(11) (2019) 1834.
[35] Y. Zhang, P. Feng, J. Yu, J. Yang, J. Zhao, J. Wang, Q. Shen, Z. Gu, Ros-responsive microneedle patch for acne vulgaris treatment, Adv. Therap. 1(3) (2018) 1800035.
[36] H. Lee, C. Song, Y.S. Hong, M.S. Kim, H.R. Cho, T. Kang, K. Shin, S.H. Choi, T. Hyeon, D.-H. Kim, Wearable/disposable sweat-based glucose monitoring device with multistage transdermal drug delivery module, Sci. Adv. 3(3) (2017) e1601314.
[37] S. Lyu, Z. Dong, X. Xu, H.-P. Bei, H.-Y. Yuen, C.-W. James Cheung, M.-S. Wong, Y. He, X. Zhao, Going below and beyond the surface: Microneedle structure, materials, drugs, fabrication, and applications for wound healing and tissue regeneration, Bioact. Mater. 27 (2023) 303-326.
[38] H.S. Gill, D.D. Denson, B.A. Burris, M.R. Prausnitz, Effect of microneedle design on pain in human subjects, The Clinical journal of pain 24(7) (2008) 585.
[39] R. Nagarkar, M. Singh, H.X. Nguyen, S. Jonnalagadda, A review of recent advances in microneedle technology for transdermal drug delivery, J. Drug Deliv. Sci. Technol. (2020) 101923.
[40] O. Khandan, M.Y. Kahook, M.P. Rao, Fenestrated microneedles for ocular drug delivery, Sens. Actuators, B 223 (2016) 15-23.
[41] W. Martanto, S.P. Davis, N.R. Holiday, J. Wang, H.S. Gill, M.R. Prausnitz, Transdermal Delivery of Insulin Using Microneedles in Vivo, Pharm. Res. 21(6)

(2004) 947-952.
[42] T. Omatsu, K. Chujo, K. Miyamoto, M. Okida, K. Nakamura, N. Aoki, R. Morita, Metal microneedle fabrication using twisted light with spin, Opt. Express 18(17) (2010) 17967-17973.
[43] S.P. Narayanan, S. Raghavan, Fabrication and characterization of gold-coated solid silicon microneedles with improved biocompatibility, The International Journal of Advanced Manufacturing Technology 104(9) (2019) 3327-3333.
[44] F.S. Iliescu, J.C.M. Teo, D. Vrtacnik, H. Taylor, C. Iliescu, Cell therapy using an array of ultrathin hollow microneedles, Microsyst. Technol. 24(7) (2018) 2905-2912.
[45] M.A. Boks, W.W. Unger, S. Engels, M. Ambrosini, Y. van Kooyk, R. Luttge, Controlled release of a model vaccine by nanoporous ceramic microneedle arrays, Int. J. Pharm. 491(1-2) (2015) 375-383.
[46] S. Lee, S. Fakhraei Lahiji, J. Jang, M. Jang, H. Jung, Micro-Pillar Integrated Dissolving Microneedles for Enhanced Transdermal Drug Delivery, Pharmaceutics 11(8) (2019) 402.
[47] S. Li, S. Dong, W. Xu, S. Tu, L. Yan, C. Zhao, J. Ding, X. Chen, Antibacterial Hydrogels, Adv. Sci. 5(5) (2018) 1700527.
[48] S. Naahidi, M. Jafari, M. Logan, Y. Wang, Y. Yuan, H. Bae, B. Dixon, P. Chen, Biocompatibility of hydrogel-based scaffolds for tissue engineering applications, Biotechnol. Adv. 35(5) (2017) 530-544.
[49] J. Li, D.J. Mooney, Designing hydrogels for controlled drug delivery, Nat. Rev. Mater. 1(12) (2016) 1-17.
[50] L. Sun, X. Zhu, X. Zhang, G. Chen, F. Bian, J. Wang, Q. Zhou, D. Wang, Y. Zhao, Induced cardiomyocytes-integrated conductive microneedle patch for treating myocardial infarction, Chem. Eng. J. 414 (2021) 128723.
[51] Y.-C. Yang, Y.-T. Lin, J. Yu, H.-T. Chang, T.-Y. Lu, T.-Y. Huang, A. Preet, Y.-J. Hsu, L. Wang, T.-E. Lin, MXene Nanosheet-Based Microneedles for Monitoring Muscle Contraction and Electrostimulation Treatment, ACS Appl. Nano Mater. 4(8) (2021) 7917-7924.
[52] Z. Chen, J. He, J. Qi, Q. Zhu, W. Wu, Y. Lu, Long-acting microneedles: a progress report of the state-of-the-art techniques, Drug Discov. Today (2020)
[53] B.Z. Chen, L.Q. Zhang, Y.Y. Xia, X.P. Zhang, X.D. Guo, A basal-bolus insulin regimen integrated microneedle patch for intraday postprandial glucose control, Sci. Adv. 6(28) (2020) eaba7260.
[54] Z. Wang, J. Wang, H. Li, J. Yu, G. Chen, A.R. Kahkoska, V. Wu, Y. Zeng, D. Wen, J.R. Miedema, Dual self-regulated delivery of insulin and glucagon by a hybrid patch, Proceedings of the National Academy of Sciences 117(47) (2020) 29512-29517.
[55] K.T. Tran, T.D. Gavitt, N.J. Farrell, E.J. Curry, A.B. Mara, A. Patel, L. Brown, S. Kilpatrick, R. Piotrowska, N. Mishra, Transdermal microneedles for the programmable burst release of multiple vaccine payloads, Nat. Biomed. Eng. (2020) 1-10.
[56] P. Yang, C. Lu, W. Qin, M. Chen, G. Quan, H. Liu, L. Wang, X. Bai, X. Pan, C. Wu, Construction of a core-shell microneedle system to achieve targeted co-delivery of checkpoint inhibitors for melanoma immunotherapy, Acta Biomater. 104 (2020)

147-157.
[57] X. Zhang, G. Chen, L. Cai, Y. Wang, L. Sun, Y. Zhao, Bioinspired pagoda-like microneedle patches with strong fixation and hemostasis capabilities, Chem. Eng. J. 414 (2021) 128905.
[58] B. Yang, Y. Dong, Y. Shen, A. Hou, G. Quan, X. Pan, C. Wu, Bilayer dissolving microneedle array containing 5-fluorouracil and triamcinolone with biphasic release profile for hypertrophic scar therapy, Bioact. Mater. 6(8) (2021) 2400-2411.
[59] S.Y. Yang, E.D. O'Cearbhaill, G.C. Sisk, K.M. Park, W.K. Cho, M. Villiger, B.E. Bouma, B. Pomahac, J.M. Karp, A bio-inspired swellable microneedle adhesive for mechanical interlocking with tissue, Nat. Commun. 4(1) (2013) 1702.
[60] E.Y. Jeon, J. Lee, B.J. Kim, K.I. Joo, K.H. Kim, G. Lim, H.J. Cha, Bio-inspired swellable hydrogel-forming double-layered adhesive microneedle protein patch for regenerative internal/external surgical closure, Biomaterials 222 (2019) 119439.
[61] K.-Y. Seong, M.-S. Seo, D.Y. Hwang, E.D. O'Cearbhaill, S. Sreenan, J.M. Karp, S.Y. Yang, A self-adherent, bullet-shaped microneedle patch for controlled transdermal delivery of insulin, J. Controlled Release 265 (2017) 48-56.
[62] D. Han, R.S. Morde, S. Mariani, A.A. La Mattina, E. Vignali, C. Yang, G. Barillaro, H. Lee, 4D Printing of a Bioinspired Microneedle Array with Backward-Facing Barbs for Enhanced Tissue Adhesion, Adv. Funct. Mater. 30(11) (2020) 1909197.
[63] X. Zhang, F. Wang, Y. Yu, G. Chen, L. Shang, L. Sun, Y. Zhao, Bio-inspired clamping microneedle arrays from flexible ferrofluid-configured moldings, Sci. Bull. 64(15) (2019) 1110-1117.
[64] S.C. Balmert, C.D. Carey, G.D. Falo, S.K. Sethi, G. Erdos, E. Korkmaz, L.D. Falo Jr, Dissolving undercut microneedle arrays for multicomponent cutaneous vaccination, J. Controlled Release 317 (2020) 336-346.
[65] X. Zhang, G. Chen, Y. Yu, L. Sun, Y. Zhao, Bioinspired Adhesive and Antibacterial Microneedles for Versatile Transdermal Drug Delivery, Research 2020 (2020)
[66] P. Zan, A. Than, P.K. Duong, J. Song, C. Xu, P. Chen, Antimicrobial Microneedle Patch for Treating Deep Cutaneous Fungal Infection, Adv. Therap. 2(10) (2019) 1900064.
[67] K. Tsioris, W.K. Raja, E.M. Pritchard, B. Panilaitis, D.L. Kaplan, F.G. Omenetto, Fabrication of silk microneedles for controlled-release drug delivery, Adv. Funct. Mater. 22(2) (2012) 330-335.
[68] A.D. Permana, M. Mir, E. Utomo, R.F. Donnelly, Bacterially sensitive nanoparticle-based dissolving microneedles of doxycycline for enhanced treatment of bacterial biofilm skin infection: A proof of concept study, Int. J. Pharm.: X 2 (2020) 100047.
[69] J. Chen, W. Huang, Z. Huang, S. Liu, Y. Ye, Q. Li, M. Huang, Fabrication of Tip-Dissolving Microneedles for Transdermal Drug Delivery of Meloxicam, AAPS PharmSciTech 19(3) (2018) 1141-1151.

[70] T. Zhang, B. Sun, J. Guo, M. Wang, H. Cui, H. Mao, B. Wang, F. Yan, Active pharmaceutical ingredient poly(ionic liquid)-based microneedles for the treatment of skin acne infection, Acta Biomater. 115 (2020) 136-147.

[71] M. Jang, B.M. Kang, H. Yang, J. Ohn, O. Kwon, H. Jung, High-Dose Steroid Dissolving Microneedle for Relieving Atopic Dermatitis, Adv. Healthc. Mater. 10(7) (2021) 2001691.

[72] I.A. Tekko, G. Chen, J. Domínguez-Robles, R.R.S. Thakur, I.M. Hamdan, L. Vora, E. Larrañeta, J.C. McElnay, H.O. McCarthy, M. Rooney, Development and characterisation of novel poly (vinyl alcohol)/poly (vinyl pyrrolidone)-based hydrogel-forming microneedle arrays for enhanced and sustained transdermal delivery of methotrexate, Int. J. Pharm. 586 (2020) 119580.

[73] S. Barrientos, O. Stojadinovic, M.S. Golinko, H. Brem, M. Tomic-Canic, Growth factors and cytokines in wound healing, Wound Repair Regen. 16(5) (2008) 585-601.

[74] E. Korkmaz, E.E. Friedrich, M.H. Ramadan, G. Erdos, A.R. Mathers, O.B. Ozdoganlar, N.R. Washburn, L.D. Falo Jr, Tip-loaded dissolvable microneedle arrays effectively deliver polymer-conjugated antibody inhibitors of tumor-necrosis-factor-alpha into human skin, J. Pharm. Sci. 105(11) (2016) 3453-3457.

[75] E. Korkmaz, E.E. Friedrich, M.H. Ramadan, G. Erdos, A.R. Mathers, O.B. Ozdoganlar, N.R. Washburn, L.D. Falo Jr, Therapeutic intradermal delivery of tumor necrosis factor-alpha antibodies using tip-loaded dissolvable microneedle arrays, Acta Biomater. 24 (2015) 96-105.

[76] J. McCaffrey, R.F. Donnelly, H.O. McCarthy, Microneedles: an innovative platform for gene delivery, Drug Deliv. Transl. Res. 5(4) (2015) 424-437.

[77] H. Shi, T. Xue, Y. Yang, C. Jiang, S. Huang, Q. Yang, D. Lei, Z. You, T. Jin, F. Wu, Q. Zhao, X. Ye, Microneedle-mediated gene delivery for the treatment of ischemic myocardial disease, Sci. Adv. 6(25) (2020) eaaz3621.

[78] M. Qu, H.-J. Kim, X. Zhou, C. Wang, X. Jiang, J. Zhu, Y. Xue, P. Tebon, S.A. Sarabi, S. Ahadian, Biodegradable microneedle patch for transdermal gene delivery, Nanoscale 12(32) (2020) 16724-16729.

[79] P. Makvandi, C.y. Wang, E.N. Zare, A. Borzacchiello, L.n. Niu, F.R. Tay, Metal-based nanomaterials in biomedical applications: Antimicrobial activity and cytotoxicity aspects, Adv. Funct. Mater. 30(22) (2020) 1910021.

[80] C.y. Wang, P. Makvandi, E.N. Zare, F.R. Tay, L.n. Niu, Advances in antimicrobial organic and inorganic nanocompounds in biomedicine, Adv. Therap. 3(8) (2020) 2000024.

[81] S.J. Lam, E.H. Wong, C. Boyer, G.G. Qiao, Antimicrobial polymeric nanoparticles, Prog. Polym. Sci. 76 (2018) 40-64.

[82] M. Zaric, O. Lyubomska, O. Touzelet, C. Poux, S. Al-Zahrani, F. Fay, L. Wallace, D. Terhorst, B. Malissen, S. Henri, Skin dendritic cell targeting via microneedle arrays laden with antigen-encapsulated poly-D, L-lactide-co-glycolide nanoparticles induces

efficient antitumor and antiviral immune responses, ACS Nano 7(3) (2013) 2042-2055.
[83] E. Ramadan, T. Borg, G. Abdelghani, N.M. Saleh, Transdermal microneedle-mediated delivery of polymeric lamivudine-loaded nanoparticles, J. Pharm. Technol. Drug Res 5(1) (2016)
[84] W. Chen, R. Tian, C. Xu, B.C. Yung, G. Wang, Y. Liu, Q. Ni, F. Zhang, Z. Zhou, J. Wang, Microneedle-array patches loaded with dual mineralized protein/peptide particles for type 2 diabetes therapy, Nat. Commun. 8(1) (2017) 1-11.
[85] Q. Zhang, K. Ma, C.-H. Lam, H.-P. Bei, Y. Liu, X. Yang, X. Zhao, Micro- and nano-environment dual-modulated anti-tendon adhesion barrier membranes, Mater. Des. 219 (2022) 110737.
[86] J. Xu, R. Danehy, H. Cai, Z. Ao, M. Pu, A. Nusawardhana, D. Rowe-Magnus, F. Guo, Microneedle patch-mediated treatment of bacterial biofilms, ACS Appl. Mater. Interfaces 11(16) (2019) 14640-14646.
[87] R. Kalluri, V.S. LeBleu, The biology, function, and biomedical applications of exosomes, Science 367(6478) (2020) eaau6977.
[88] A. Golchin, S. Hosseinzadeh, A. Ardeshirylajimi, The exosomes released from different cell types and their effects in wound healing, J. Cell. Biochem. 119(7) (2018) 5043-5052.
[89] S. Nour, N. Baheiraei, R. Imani, M. Khodaei, A. Alizadeh, N. Rabiee, S.M. Moazzeni, A review of accelerated wound healing approaches: biomaterial-assisted tissue remodeling, J. Mater. Sci.: Mater. Med. 30(10) (2019) 1-15.
[90] H.-P. Bei, T. Xu, J. Zhou, Z. Dong, Y. Wang, K.-Y. Wong, H. Wang, X. Zhao, Evaporation-based, co-axial lock-and-key fibrous reservoir for long-term prevention of hypertrophic scars, Appl. Mater. Today 27 (2022) 101463.
[91] X. Sun, Q. Lang, H. Zhang, L. Cheng, Y. Zhang, G. Pan, X. Zhao, H. Yang, Y. Zhang, H.A. Santos, W. Cui, Electrospun Photocrosslinkable Hydrogel Fibrous Scaffolds for Rapid In Vivo Vascularized Skin Flap Regeneration, Adv. Funct. Mater. 27(2) (2017) 1604617.
[92] L. Cheng, X. Sun, X. Zhao, L. Wang, J. Yu, G. Pan, B. Li, H. Yang, Y. Zhang, W. Cui, Surface biofunctional drug-loaded electrospun fibrous scaffolds for comprehensive repairing hypertrophic scars, Biomaterials 83 (2016) 169-181.
[93] X. Sun, R. Zheng, L. Cheng, X. Zhao, R. Jin, L. Zhang, Y. Zhang, Y. Zhang, W. Cui, Two-dimensional electrospun nanofibrous membranes for promoting random skin flap survival, RSC Adv. 6(11) (2016) 9360-9369.
[94] M. Badmus, J. Liu, N. Wang, N. Radacsi, Y. Zhao, Hierarchically electrospun nanofibers and their applications: A review, Nano Mater. Sci. 3(3) (2021) 213-232.
[95] H. Chen, R. Cheng, X. Zhao, Y. Zhang, A. Tam, Y. Yan, H. Shen, Y.S. Zhang, J. Qi, Y. Feng, L. Liu, G. Pan, W. Cui, L. Deng, An injectable self-healing coordinative hydrogel with antibacterial and angiogenic properties for diabetic skin wound repair, NPG Asia Mater. 11(1) (2019) 3.
[96] X. Zhao, X. Sun, L. Yildirimer, Q. Lang, Z.Y. Lin, R. Zheng, Y. Zhang, W. Cui, N. Annabi, A. Khademhosseini, Cell infiltrative hydrogel fibrous scaffolds for accelerated wound healing, Acta Biomater. 49 (2017) 66-77.

[97] W. Jiang, L. Ma, X. Xu, One-dimensional microstructure-assisted intradermal and intracellular delivery, Bio-Des. Manuf. 2(1) (2019) 24-30.
[98] J. Chi, X. Zhang, C. Chen, C. Shao, Y. Zhao, Y. Wang, Antibacterial and angiogenic chitosan microneedle array patch for promoting wound healing, Bioact. Mater. 5(2) (2020) 253-259.
[99] L. Sun, Y. Wang, L. Fan, Y. Zhao, Multifunctional microneedle patches with aligned carbon nanotube sheet basement for promoting wound healing, Chem. Eng. J. 457 (2023) 141206.
[100] M. Yuan, K. Liu, T. Jiang, S. Li, J. Chen, Z. Wu, W. Li, R. Tan, W. Wei, X. Yang, H. Dai, Z. Chen, GelMA/PEGDA microneedles patch loaded with HUVECs-derived exosomes and Tazarotene promote diabetic wound healing, J. Nanobiotechnol. 20(1) (2022) 147.
[101] J. Gan, X. Zhang, W. Ma, Y. Zhao, L. Sun, Antibacterial, adhesive, and MSC exosomes encapsulated microneedles with spatio-temporal variation functions for diabetic wound healing, Nano Today 47 (2022) 101630.
[102] W. Ma, X. Zhang, Y. Liu, L. Fan, J. Gan, W. Liu, Y. Zhao, L. Sun, Polydopamine Decorated Microneedles with Fe-MSC-Derived Nanovesicles Encapsulation for Wound Healing, Adv. Sci. 9(13) (2022) 2103317.
[103] A. Fang, Y. Wang, N. Guan, Y. Zuo, L. Lin, B. Guo, A. Mo, Y. Wu, X. Lin, W. Cai, X. Chen, J. Ye, Z. Abdelrahman, X. Li, H. Zheng, Z. Wu, S. Jin, K. Xu, Y. Huang, X. Gu, B. Yu, X. Wang, Porous microneedle patch with sustained delivery of extracellular vesicles mitigates severe spinal cord injury, Nat. Commun. 14(1) (2023) 4011.
[104] K. Lee, Y. Xue, J. Lee, H.-J. Kim, Y. Liu, P. Tebon, E. Sarikhani, W. Sun, S. Zhang, R. Haghniaz, B. Çelebi-Saltik, X. Zhou, S. Ostrovidov, S. Ahadian, N. Ashammakhi, M.R. Dokmeci, A. Khademhosseini, A patch of detachable hybrid microneedle depot for localized delivery of mesenchymal stem cells in regeneration therapy, Adv. Funct. Mater. 30(23) (2020) 2000086.
[105] Y. Xu, X. Wu, X. Zhang, Y. Zu, Q. Tan, Y. Zhao, Living Microneedle Patch with Adipose-Derived Stem Cells Embedding for Diabetic Ulcer Healing, Adv. Funct. Mater. 33(1) (2023) 2209986.
[106] X. Zhang, G. Chen, Y. Liu, L. Sun, L. Sun, Y. Zhao, Black Phosphorus-Loaded Separable Microneedles as Responsive Oxygen Delivery Carriers for Wound Healing, ACS Nano 14(5) (2020) 5901-5908.
[107] Z. Guo, H. Liu, Z. Shi, L. Lin, Y. Li, M. Wang, G. Pan, Y. Lei, L. Xue, Responsive hydrogel-based microneedle dressing for diabetic wound healing, J. Mater. Chem. B 10(18) (2022) 3501-3511.
[108] Q. Lei, D. He, L. Ding, F. Kong, P. He, J. Huang, J. Guo, C.J. Brinker, G. Luo, W. Zhu, Microneedle Patches Integrated with Biomineralized Melanin Nanoparticles for Simultaneous Skin Tumor Photothermal Therapy and Wound Healing, Adv. Funct. Mater. (2022) 2113269.
[109] Y. Wang, A.a. Sheng, X. Jiang, S. Yang, L. Lin, M. Yang, F. Zhu, Y. Hu, J. Li, L. Chang, Multidrug dissolvable microneedle patch for the treatment of recurrent oral ulcer, Bio-Des. Manuf. 6(3) (2023) 255-267.

[110] T. Ning, F. Yang, D. Chen, Z. Jia, R. Yuan, Z. Du, S. Liu, Y. Yu, X. Dai, X. Niu, Y. Fan, Synergistically Detachable Microneedle Dressing for Programmed Treatment of Chronic Wounds, Adv. Healthc. Mater. 11(11) (2022) 2102180.
[111] Y. Yang, Q. Zhang, T. Xu, H. Zhang, M. Zhang, L. Lu, Y. Hao, J.H. Fuh, X. Zhao, Photocrosslinkable nanocomposite ink for printing strong, biodegradable and bioactive bone graft, Biomaterials 263 (2020) 120378.
[112] P. Guan, C. Liu, D. Xie, S. Mao, Y. Ji, Y. Lin, Z. Chen, Q. Wang, L. Fan, Y. Sun, Exosome-loaded extracellular matrix-mimic hydrogel with anti-inflammatory property Facilitates/promotes growth plate injury repair, Bioact. Mater. 10 (2022) 145-158.
[113] M. Arabpour, A. Saghazadeh, N. Rezaei, Anti-inflammatory and M2 macrophage polarization-promoting effect of mesenchymal stem cell-derived exosomes, Int. Immunopharmacol. 97 (2021) 107823.
[114] H.P. Bei, P.M. Hung, H.L. Yeung, S. Wang, X. Zhao, Bone-a-Petite: Engineering Exosomes towards Bone, Osteochondral, and Cartilage Repair, Small 17(50) (2021) 2101741.
[115] B.F. Hettich, M. Ben‐Yehuda Greenwald, S. Werner, J.C. Leroux, Exosomes for wound healing: purification optimization and identification of bioactive components, Adv. Sci. 7(23) (2020) 2002596.
[116] J.D. Anderson, H.J. Johansson, C.S. Graham, M. Vesterlund, M.T. Pham, C.S. Bramlett, E.N. Montgomery, M.S. Mellema, R.L. Bardini, Z. Contreras, Comprehensive proteomic analysis of mesenchymal stem cell exosomes reveals modulation of angiogenesis via nuclear factor-kappaB signaling, Stem Cells 34(3) (2016) 601-613.
[117] D. Deng, X. Li, J.-J. Zhang, Y. Yin, Y. Tian, D. Gan, R. Wu, J. Wang, B.-M. Tian, F.-M. Chen, X.-T. He, Biotin–Avidin System-Based Delivery Enhances the Therapeutic Performance of MSC-Derived Exosomes, ACS Nano (2023)
[118] X. Tong, Y. Xu, T. Zhang, C. Deng, J. Xun, D. Sun, D. Xu, Exosomes from CD133+ human urine-derived stem cells combined adhesive hydrogel facilitate rotator cuff healing by mediating bone marrow mesenchymal stem cells, Journal of Orthopaedic Translation 39 (2023) 100-112.
[119] T. Xu, Y. Yang, E.H.-L. Yeung, Q. Chen, H.-P. Bei, Q. Yang, M. Yang, Y. Hao, B. Li, X. Zhao, Injectable, Self-Contained, Subaqueously Cross-Linking Laminous Adhesives for Biophysical-Chemical Modulation of Osteochondral Microenvironment, Adv. Funct. Mater. n/a(n/a) 2213428.
[120] J. Fang, H. Liu, W. Qiao, T. Xu, Y. Yang, H. Xie, C.-H. Lam, K.W.K. Yeung, X. Zhao, Biomimicking Leaf-Vein Engraved Soft and Elastic Membrane Promotes Vascular Reconstruction, Adv. Healthc. Mater. 12(2) (2023) 2201220.
[121] Y. Yang, T. Xu, H.P. Bei, Y. Zhao, X. Zhao, Sculpting Bio-Inspired Surface Textures: An Adhesive Janus Periosteum, Adv. Funct. Mater. 31(37) (2021) 2104636.
[122] X. Zhao, I. Olsen, H. Li, K. Gellynck, P.G. Buxton, J.C. Knowles, V. Salih, A.M. Young, Reactive calcium-phosphate-containing poly(ester-co-ether) methacrylate bone adhesives: Chemical, mechanical and biological considerations, Acta Biomater.

6(3) (2010) 845-855.
[123] Y. Piao, H. You, T. Xu, H.-P. Bei, I.Z. Piwko, Y.Y. Kwan, X. Zhao, Biomedical applications of gelatin methacryloyl hydrogels, Eng. Regener. 2 (2021) 47-56.
[124] X. Zhao, S. Liu, L. Yildirimer, H. Zhao, R. Ding, H. Wang, W. Cui, D. Weitz, Injectable Stem Cell-Laden Photocrosslinkable Microspheres Fabricated Using Microfluidics for Rapid Generation of Osteogenic Tissue Constructs, Adv. Funct. Mater. 26(17) (2016) 2809-2819.
[125] X. Zhao, Q. Lang, L. Yildirimer, Z.Y. Lin, W. Cui, N. Annabi, K.W. Ng, M.R. Dokmeci, A.M. Ghaemmaghami, A. Khademhosseini, Photocrosslinkable Gelatin Hydrogel for Epidermal Tissue Engineering, Adv. Healthc. Mater. 5(1) (2016) 108-118.
[126] H. Chen, L. Guo, J. Wicks, C. Ling, X. Zhao, Y. Yan, J. Qi, W. Cui, L. Deng, Quickly promoting angiogenesis by using a DFO-loaded photo-crosslinked gelatin hydrogel for diabetic skin regeneration, J. Mater. Chem. B 4(21) (2016) 3770-3781.
[127] Z. Zeng, G. Jiang, T. Liu, G. Song, Y. Sun, X. Zhang, Y. Jing, M. Feng, Y. Shi, Fabrication of gelatin methacryloyl hydrogel microneedles for transdermal delivery of metformin in diabetic rats, Bio-Des. Manuf. 4(4) (2021) 902-911.
[128] M. Qu, H.-J. Kim, X. Zhou, C. Wang, X. Jiang, J. Zhu, Y. Xue, P. Tebon, S.A. Sarabi, S. Ahadian, M.R. Dokmeci, S. Zhu, Z. Gu, W. Sun, A. Khademhosseini, Biodegradable microneedle patch for transdermal gene delivery, Nanoscale 12(32) (2020) 16724-16729.
[129] W.C. Oliver, G.M. Pharr, An improved technique for determining hardness and elastic modulus using load and displacement sensing indentation experiments, J. Mater. Res. 7(6) (1992) 1564-1583.
[130] M.-L. Laracuente, M.H. Yu, K.J. McHugh, Zero-order drug delivery: State of the art and future prospects, J. Controlled Release 327 (2020) 834-856.
[131] S. Chavoshi, M. Rabiee, M. Rafizadeh, N. Rabiee, A.S. Shamsabadi, M. Bagherzadeh, R. Salarian, M. Tahriri, L. Tayebi, Mathematical modeling of drug release from biodegradable polymeric microneedles, Bio-Des. Manuf. 2(2) (2019) 96-107.
[132] E. Adams, D. Coomans, J. Smeyers-Verbeke, D.L. Massart, Non-linear mixed effects models for the evaluation of dissolution profiles, Int. J. Pharm. 240(1) (2002) 37-53.
[133] V. Papadopoulou, K. Kosmidis, M. Vlachou, P. Macheras, On the use of the Weibull function for the discernment of drug release mechanisms, Int. J. Pharm. 309(1) (2006) 44-50.
[134] A.C. Gonzalez, T.F. Costa, Z.A. Andrade, A.R. Medrado, Wound healing - A literature review, An Bras Dermatol 91(5) (2016) 614-620.
[135] O.S. Manoukian, A. Ahmad, C. Marin, R. James, A.D. Mazzocca, S.G. Kumbar, 22 - Bioactive nanofiber dressings for wound healing, in: M.S. Ågren (Ed.), Wound Healing Biomaterials, Woodhead Publishing2016, pp. 451-481.
[136] 5 - Mathematical models of drug release, in: M.L. Bruschi (Ed.), Strategies to Modify the Drug Release from Pharmaceutical Systems, Woodhead Publishing2015, pp. 63-86.

[137] F. Yang, J. Wang, X. Li, Z. Jia, Q. Wang, D. Yu, J. Li, X. Niu, Electrospinning of a sandwich-structured membrane with sustained release capability and long-term anti-inflammatory effects for dental pulp regeneration, Bio-Des. Manuf. 5(2) (2022) 305-317.
[138] S.J. de Jong, E.R. Arias, D.T.S. Rijkers, C.F. van Nostrum, J.J. Kettenes-van den Bosch, W.E. Hennink, New insights into the hydrolytic degradation of poly(lactic acid): participation of the alcohol terminus, Polymer 42(7) (2001) 2795-2802.
[139] H.S. Kim, X. Sun, J.-H. Lee, H.-W. Kim, X. Fu, K.W. Leong, Advanced drug delivery systems and artificial skin grafts for skin wound healing, Adv. Drug Delivery Rev. 146 (2019) 209-239.
[140] H. Pratsinis, E. Mavrogonatou, D. Kletsas, Scarless wound healing: From development to senescence, Adv. Drug Delivery Rev. 146 (2019) 325-343.
[141] P. Wu, Y. Liang, G. Sun, Engineering immune-responsive biomaterials for skin regeneration, Biomater Transl. 2(1) (2021) 61-71.
[142] S. Saha, P. Sadhukhan, P.C. Sil, Mangiferin: A xanthonoid with multipotent anti-inflammatory potential, BioFactors 42(5) (2016) 459-474.
[143] A.J. Núñez Selles, M. Daglia, L. Rastrelli, The potential role of mangiferin in cancer treatment through its immunomodulatory, anti‐angiogenic, apoptopic, and gene regulatory effects, Biofactors 42(5) (2016) 475-491.
[144] Z. Wei, L. Yan, Y. Chen, C. Bao, J. Deng, J. Deng, Mangiferin inhibits macrophage classical activation via downregulating interferon regulatory factor 5 expression, Mol Med Rep 14(2) (2016) 1091-1098.
[145] Q.J. Zhang, L. Yue, INHIBITORY ACTIVITY OF MANGIFERIN ON HELICOBACTER PYLORI-INDUCED INFLAMMATION IN HUMAN GASTRIC CARCINOMA AGS CELLS, Afr J Tradit Complement Altern Med 14(1) (2017) 263-271.
[146] J. Rodríguez, D. Di Pierro, M. Gioia, S. Monaco, R. Delgado, M. Coletta, S. Marini, Effects of a natural extract from Mangifera indica L, and its active compound, mangiferin, on energy state and lipid peroxidation of red blood cells, Biochimica et Biophysica Acta (BBA) - General Subjects 1760(9) (2006) 1333-1342.
[147] I. Rodeiro, M.T. Donato, I. Martínez, I. Hernández, G. Garrido, J.A. González-Lavaut, R. Menéndez, A. Laguna, J.V. Castell, M.J. Gómez-Lechón, Potential hepatoprotective effects of new Cuban natural products in rat hepatocytes culture, Toxicol. in Vitro 22(5) (2008) 1242-1249.
[148] M. Li, T. Wang, H. Tian, G. Wei, L. Zhao, Y. Shi, Macrophage-derived exosomes accelerate wound healing through their anti-inflammation effects in a diabetic rat model, Artif. Cells Nanomed. Biotechnol. 47(1) (2019) 3793-3803.
[149] J. Zhang, J. Guan, X. Niu, G. Hu, S. Guo, Q. Li, Z. Xie, C. Zhang, Y. Wang, Exosomes released from human induced pluripotent stem cells-derived MSCs facilitate cutaneous wound healing by promoting collagen synthesis and angiogenesis, Journal of translational medicine 13(1) (2015) 1-14.
[150] M. Isakson, C. de Blacam, D. Whelan, A. McArdle, A.J.P. Clover, Mesenchymal Stem Cells and Cutaneous Wound Healing: Current Evidence and

Future Potential, Stem Cells International 2015 (2015) 831095.
[151] K. Ousey, K.F. Cutting, A.A. Rogers, M.G. Rippon, The importance of hydration in wound healing: reinvigorating the clinical perspective, Journal of Wound Care 25(3) (2016) 122-130.
[152] M.B. Dreifke, A.A. Jayasuriya, A.C. Jayasuriya, Current wound healing procedures and potential care, Materials Science and Engineering: C 48 (2015) 651-662.
[153] S. Ding, S. He, K. Ye, X. Shao, Q. Yang, G. Yang, Photopolymerizable, immunomodulatory hydrogels of gelatin methacryloyl and carboxymethyl chitosan as all-in-one strategic dressing for wound healing, Int. J. Biol. Macromol. 253 (2023) 127151.
[154] B. Jiang, A. Shi, Y. Xu, Y. Zhang, Y. Chen, X. Jiang, H. Liu, L. Zhang, SDF-1α and CTGF functionalized Gelatin methacryloyl (GelMA) hydrogels enhance fibroblast activation to promote wound healing, Mater. Today Commun. 34 (2023) 105152.
[155] T. Kushibiki, Y. Mayumi, E. Nakayama, R. Azuma, K. Ojima, A. Horiguchi, M. Ishihara, Photocrosslinked gelatin hydrogel improves wound healing and skin flap survival by the sustained release of basic fibroblast growth factor, Sci. Rep. 11(1) (2021) 23094.
[156] G. Wang, W. Wang, Z. Chen, T. Hu, L. Tu, X. Wang, W. Hu, S. Li, Z. Wang, Photothermal microneedle patch loaded with antimicrobial peptide/MnO2 hybrid nanoparticles for chronic wound healing, Chem. Eng. J. 482 (2024) 148938.
[157] Y. Yi, Z. Yang, C. Zhou, Y. Yang, Y. Wu, Q. Zhang, Quercetin-encapsulated GelMa hydrogel microneedle reduces oxidative stress and facilitates wound healing, Nano TransMed 3 (2024) 100030.
[158] A.K. Gupta, T. Wang, J.A. Rapaport, Systematic review of exosome treatment in hair restoration: Preliminary evidence, safety, and future directions, Journal of Cosmetic Dermatology n/a(n/a)
[159] V. Sarrazy, F. Billet, L. Micallef, B. Coulomb, A. Desmoulière, Mechanisms of pathological scarring: Role of myofibroblasts and current developments, Wound Repair Regen. 19(s1) (2011) s10-s15.
[160] B.H. Pan, Q. Zhang, C.H. Lam, H.Y. Yuen, S. Kuang, X. Zhao, Petite miracles: insight into the nano-management of scarless wound healing, Drug Discov. Today 27(3) (2022) 857-865.
[161] A.V. Shinde, C. Humeres, N.G. Frangogiannis, The role of α-smooth muscle actin in fibroblast-mediated matrix contraction and remodeling, Biochimica et Biophysica Acta (BBA) - Molecular Basis of Disease 1863(1) (2017) 298-309.
[162] C.-C. Tsai, S.-B. Wu, H.-C. Kau, Y.-H. Wei, Essential role of connective tissue growth factor (CTGF) in transforming growth factor-β1 (TGF-β1)-induced myofibroblast transdifferentiation from Graves' orbital fibroblasts, Sci. Rep. 8(1) (2018) 7276.
[163] D.C. Yeo, C. Wiraja, A.S. Paller, C.A. Mirkin, C. Xu, Abnormal scar identification with spherical-nucleic-acid technology, Nat. Biomed. Eng. 2(4) (2018) 227-238.

[164] K.E. Lipson, C. Wong, Y. Teng, S. Spong, CTGF is a central mediator of tissue remodeling and fibrosis and its inhibition can reverse the process of fibrosis, Fibrogenesis & Tissue Repair 5(1) (2012) S24.
[165] A.L. Moore, C.D. Marshall, A. Nauta, H.P. Lorenz, M.T. Longaker, Chapter 5 - Scarless Wound Healing: From Experimental Target to Clinical Reality, in: A. Atala, R. Lanza, A.G. Mikos, R. Nerem (Eds.), Principles of Regenerative Medicine (Third Edition), Academic Press, Boston, 2019, pp. 65-92.
[166] G.G. Gauglitz, Management of keloids and hypertrophic scars: current and emerging options, CLIN. COSMET. INVESTIG. DERMATOL. 6 (2013) 103-114.
[167] B. Berman, A. Maderal, B. Raphael, Keloids and Hypertrophic Scars: Pathophysiology, Classification, and Treatment, Dermatologic Surgery 43 (2017) S3-S18.
[168] K. Chen, D. Henn, M. Januszyk, J.A. Barrera, C. Noishiki, C.A. Bonham, M. Griffin, R. Tevlin, T. Carlomagno, T. Shannon, T. Fehlmann, A.A. Trotsyuk, J. Padmanabhan, D. Sivaraj, D.P. Perrault, A.I. Zamaleeva, C.J. Mays, A.H. Greco, S.H. Kwon, M.C. Leeolou, S.L. Huskins, S.R. Steele, K.S. Fischer, H.C. Kussie, S. Mittal, A.M. Mermin-Bunnell, N.M. Diaz Deleon, C. Lavin, A. Keller, M.T. Longaker, G.C. Gurtner, Disrupting mechanotransduction decreases fibrosis and contracture in split-thickness skin grafting, Sci. Transl. Med. 14(645) (2022) eabj9152.
[169] R.A.F. Clark, To Scar or Not to Scar, N. Engl. J. Med. 385(5) (2021) 469-471.
[170] S. O'Reilly, E. Crofton, J. Brown, J. Strong, J. Ziviani, Use of tape for the management of hypertrophic scar development: A comprehensive review, Scars, Burns & Healing 7 (2021) 20595131211029206.
[171] V.W. Wong, K. Levi, S. Akaishi, G. Schultz, R.H. Dauskardt, Scar Zones: Region-Specific Differences in Skin Tension May Determine Incisional Scar Formation, Plastic and Reconstructive Surgery 129(6) (2012) 1272-1276.
[172] B. Kuehlmann, C.A. Bonham, I. Zucal, L. Prantl, G.C. Gurtner, Mechanotransduction in Wound Healing and Fibrosis, Journal of Clinical Medicine 9(5) (2020) 1423.
[173] K. Chen, S.H. Kwon, D. Henn, B.A. Kuehlmann, R. Tevlin, C.A. Bonham, M. Griffin, A.A. Trotsyuk, M.R. Borrelli, C. Noishiki, J. Padmanabhan, J.A. Barrera, Z.N. Maan, T. Dohi, C.J. Mays, A.H. Greco, D. Sivaraj, J.Q. Lin, T. Fehlmann, A.M. Mermin-Bunnell, S. Mittal, M.S. Hu, A.I. Zamaleeva, A. Keller, J. Rajadas, M.T. Longaker, M. Januszyk, G.C. Gurtner, Disrupting biological sensors of force promotes tissue regeneration in large organisms, Nat. Commun. 12(1) (2021) 5256.
[174] K. Chen, A. Vigliotti, M. Bacca, R.M. McMeeking, V.S. Deshpande, J.W. Holmes, Role of boundary conditions in determining cell alignment in response to stretch, Proceedings of the National Academy of Sciences 115(5) (2018) 986-991.
[175] H. Atcha, A. Jairaman, J.R. Holt, V.S. Meli, R.R. Nagalla, P.K. Veerasubramanian, K.T. Brumm, H.E. Lim, S. Othy, M.D. Cahalan, M.M. Pathak, W.F. Liu, Mechanically activated ion channel Piezo1 modulates macrophage polarization and stiffness sensing, Nat. Commun. 12(1) (2021) 3256.
[176] J. Jiang, F. Wang, W. Huang, J. Sun, Y. Ye, J. Ou, M. Liu, J. Gao, S. Wang, D. Fu, B. Chen, L. Liu, F. Peng, Y. Tu, Mobile mechanical signal generator for

macrophage polarization, Exploration 3(2) (2023) 20220147.
[177] D. Bannerman, S. Pascual-Gil, M. Radisic, An optimal gel patch for the injured heart, Nat. Biomed. Eng. 3(8) (2019) 592-593.
[178] V. Sharma, S.K. Dash, K. Govarthanan, R. Gahtori, N. Negi, M. Barani, R. Tomar, S. Chakraborty, S. Mathapati, D.K. Bishi, Recent advances in cardiac tissue engineering for the management of myocardium infarction, Cells 10(10) (2021) 2538.
[179] T.J. Cahill, R.P. Choudhury, P.R. Riley, Heart regeneration and repair after myocardial infarction: translational opportunities for novel therapeutics, Nat. Rev. Drug Discovery 16(10) (2017) 699-717.
[180] E. Braunwald, Cell-based therapy in cardiac regeneration: an overview, Circulation research 123(2) (2018) 132-137.
[181] S. Lim, T.Y. Park, E.Y. Jeon, K.I. Joo, H.J. Cha, Double-layered adhesive microneedle bandage based on biofunctionalized mussel protein for cardiac tissue regeneration, Biomaterials 278 (2021) 121171.
[182] M.N. Hirt, A. Hansen, T. Eschenhagen, Cardiac tissue engineering: state of the art, Circulation research 114(2) (2014) 354-367.
[183] L. Dong, C. Jin, A.B. Closson, I. Trase, H.C. Richards, Z. Chen, J.X. Zhang, Cardiac energy harvesting and sensing based on piezoelectric and triboelectric designs, Nano Energy 76 (2020) 105076.
[184] X. Cai, T. Lei, D. Sun, L. Lin, A critical analysis of the α, β and γ phases in poly(vinylidene fluoride) using FTIR, RSC Adv. 7(25) (2017) 15382-15389.
[185] L. Lu, W. Ding, J. Liu, B. Yang, Flexible PVDF based piezoelectric nanogenerators, Nano Energy 78 (2020) 105251.
[186] J. Pu, X. Yan, Y. Jiang, C. Chang, L. Lin, Piezoelectric actuation of direct-write electrospun fibers, Sens. Actuators, A 164(1-2) (2010) 131-136.
[187] Y. Duan, Y. Huang, Z. Yin, N. Bu, W. Dong, Non-wrinkled, highly stretchable piezoelectric devices by electrohydrodynamic direct-writing, Nanoscale 6(6) (2014) 3289-3295.
[188] C. Chang, Y.-K. Fuh, L. Lin, A direct-write piezoelectric PVDF nanogenerator, TRANSDUCERS 2009-2009 International Solid-State Sensors, Actuators and Microsystems Conference, IEEE, 2009, pp. 1485-1488.
[189] X. Cai, T. Lei, D. Sun, L. Lin, A critical analysis of the α, β and γ phases in poly (vinylidene fluoride) using FTIR, RSC Adv. 7(25) (2017) 15382-15389.
[190] J. Hescheler, R. Meyer, S. Plant, D. Krautwurst, W. Rosenthal, G. Schultz, Morphological, biochemical, and electrophysiological characterization of a clonal cell (H9c2) line from rat heart, Circulation research 69(6) (1991) 1476-1486.
[191] M.L. Lindsey, R. Bolli, J.M.C. Jr., X.-J. Du, N.G. Frangogiannis, S. Frantz, R.G. Gourdie, J.W. Holmes, S.P. Jones, R.A. Kloner, D.J. Lefer, R. Liao, E. Murphy, P. Ping, K. Przyklenk, F.A. Recchia, L.S. Longacre, C.M. Ripplinger, J.E.V. Eyk, G. Heusch, Guidelines for experimental models of myocardial ischemia and infarction, American Journal of Physiology-Heart and Circulatory Physiology 314(4) (2018) H812-H838.
[192] K.E. Odening, I. Baczko, M. Brunner, Animals in cardiovascular research: important role of rabbit models in cardiac electrophysiology, European Heart Journal

41(21) (2020) 2036-2036.
[193] E. Sung, A. Prakosa, S. Zhou, R.D. Berger, J. Chrispin, S. Nazarian, N.A. Trayanova, Fat infiltration in the infarcted heart as a paradigm for ventricular arrhythmias, Nat. Cardiovasc. Res. 1(10) (2022) 933-945.
[194] H.F. Weisman, D.E. Bush, J.A. Mannisi, B.H. Bulkley, Global cardiac remodeling after acute myocardial infarction: A study in the rat model, J. Am. Coll. Cardiol. 5(6) (1985) 1355-1362.
[195] B.I. Jugdutt, Ventricular Remodeling After Infarction and the Extracellular Collagen Matrix, Circulation 108(11) (2003) 1395-1403.
[196] J. Beugels, D.G.M. Molin, D.R.M.G. Ophelders, T. Rutten, L. Kessels, N. Kloosterboer, A.A.P.d. Grzymala, B.W.W. Kramer, R.R.W.J. van der Hulst, T.G.A.M. Wolfs, Electrical stimulation promotes the angiogenic potential of adipose-derived stem cells, Sci. Rep. 9(1) (2019) 12076.
[197] G.-J. Jeong, J.Y. Oh, Y.-J. Kim, S.H. Bhang, H.-K. Jang, J. Han, J.-K. Yoon, S.-M. Kwon, T.I. Lee, B.-S. Kim, Therapeutic Angiogenesis via Solar Cell-Facilitated Electrical Stimulation, ACS Appl. Mater. Interfaces 9(44) (2017) 38344-38355.